Betreuer

D I P L O M A R B E I T

Modifications of Spectra and Correlations through Yoctosecond Photon Double Pulses from a Quark-Gluon Plasma

ausgeführt am Institut für
Theoretische Physik
der Technischen Universität Wien

bei
Univ.-Prof. DI Dr. Anton Rebhan
unter Anleitung von
Univ.Ass. Dr. Andreas Ipp

durch
Ing. Peter Somkuti

Ort, Datum

Unterschrift

Abstract

We calculate Hanbury Brown - Twiss (HBT) correlation functions as well as direct photon spectra from an anisotropic quark-gluon plasma (QGP) in order to investigate possible indirect signals of photon double pulses on the yoctosecond timescale, which arise at low emission angles. Both quantities show a dependence on the isotropization time of the QGP. We find that HBT correlations exhibit non-trivial features, such as plateaus or a second peak. The ratio of two spectra measured at different emission angles is especially sensitive to early isotropization times.

Zusammenfassung

In Schwerionenkollisionen werden Quark-Gluon Plasmas (QGP) erzeugt, welche aufgrund der raschen longitudinalen Expansion eine Anisotropie im Impulsraum aufweisen. Diese Anisotropie ist die Ursache dafür, dass die differentielle thermische Photonenrate im Plasma eine starke Abhängigkeit einerseits von der Richtung der Emission, als auch von der Stärke der Anisotropie besitzt. Anhand der Emissionsrate des Plasmas, lässt sich nun ein zeitabhängiges Photonensignal berechnen, welches von einem idealen Detektor gemessen wird. Diese Photonenpulse haben eine Länge von einigen Yoctosekunden (10^{-24}s), was in etwa der selben Größenordnung wie der Lebensdauer des QGP entspricht. Platziert man den Detektor zu kleineren Winkel hin, nahe zur Strahlachse der Kollision, weisen die Pulse eine außergewöhnliche Doppelpuls-Struktur auf. Die Form der Pulse ist sehr empfindlich im Bezug auf die Parameter des QGP-Modells, was deren Messung als Methode prädestiniert, um die internen Dynamiken des Plasmas zu erforschen. Zum jetzigen Zeitpunkt gibt es noch keinen Ansatz um Strukturen zeitaufgelöst im Bereich von Yoctosekunden zu messen. Daher werden in dieser Arbeit Methoden untersucht, die ein indirektes Signal für die Existenz solcher Doppelpulse liefern könnten.

Spektren von thermischen Photonen und Hanbury Brown - Twiss (HBT) Korrelationen zeigen eine Abhängigkeit von der Isotropisierungszeit - jener Zeitkonstante, zu der das Plasma wieder annähernd isotrop wird. Dieser Parameter spielt eine große Rolle für die Phänomenologie der Doppelpulse. Bei dem Verhältnis zweier Spektren, gemessen in verschiedene Richtungen (etwa in Vorwärtsrichtung und im rechten Winkel zur Strahlachse), handelt es sich um eine Größe, die sehr empflindlich im Bezug auf sehr frühe Isotropisierungszeiten ist. Analysiert man HBT Korrelationen für verschiedene Photon-Vektor-Paar Geometrien, findet man nicht-triviale Modifikationen der üblichen Gauß'schen Form, deren Ursache die Unterdrückung der Photonenrate durch die Anisotropie ist.

Contents

Acknowledgments

Handing in this thesis concludes a long journey that was studying physics at the Vienna University of Technology. At this point I want to express my thanks to Anton Rebhan and the Institute for Theoretical Physics for providing me both with the opportunity to write this thesis as well as the marvelous environment in which I, as an undergraduate student, was allowed to take part in meetings and conferences. I am especially grateful to my co-supervisor Andreas Ipp, who, without exception, always took the time to help me and discuss matters, trivial or intricate. Additional thanks go to Andreas Schmitt for providing hints on the design of the introduction. I of course want to mention the fellow students who shared the office with me and were so kind as to help me with the one or the other little problem: Erwin Kronberger, Franz Heindl, Thomas Garschall, Thomas Mörtlbauer (who provided the neat title page), Frederic Brünner and Oskar Till. Outside of the university, I need to thank both Stefan Wagner and Christian Schmid for the nights of inline-skating and the many visits to the movies, which kept me from going insane through these years. Thanks to the crew at Südwind and Harald Schweigert at Siemens, who both offered me much flexibility regarding my working hours to keep up with the varying schedule at the university.

Finally, I need to thank my parents Sándor and Ilona Somkuti, without whom all this would not have been possible in the first place.

Peter Somkuti
Vienna,
December 2011

—The world which we perceive is a tiny fraction of the world which we can perceive, which is a tiny fraction of the perceivable world, you see.

– Terence Kemp McKenna

1 Introduction

1.1. Asymptotic freedom and the quark-gluon plasma

The standard model of particle physics is currently the leading theory to describe nature on a subatomic scale. It unifies the electroweak interaction together with the strong nuclear force in the framework of a quantum gauge field theory, a theory whose Lagrangian is invariant under continuous local transformations. The theory of strong interactions, quantum chromodynamics (QCD), belongs to the class of non-Abelian gauge theories, also called Yang-Mills theories in honor of their inventors Chen Ning Yang and Robert L. Mills [1]. Non-Abelian gauge theories exhibit a feature that was revealed by David Gross, David Politzer and Frank Wilczek [2–4], who were awarded the Nobel prize in physics in 2004 for their discovery. This property is called *asymptotic freedom* and refers to the fact that the coupling or the interaction strength of such a theory becomes weak at large energy scales.

Interactions within a quantum field theory may be altered by the presence of loop diagrams. Such is the case in quantum electrodynamics (QED), where the vacuum polarization diagram changes the effective interaction, as depicted in Fig. 1.1.

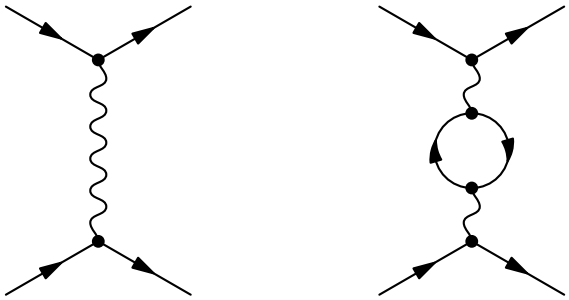

Figure 1.1: Electron-electron interaction via photon exchange in QED. The time direction points to the right. Lines with arrows represent the fermionic electrons, the wiggly line is the photon.

The diagram in Fig. 1.1a shows the known tree-level electron-electron interaction mediated by the gauge boson of QED, the photon γ. By insertion of a vacuum polarization diagram (Fig. 1.1b), the interaction becomes a function of the energy scale Q. Scaling behavior of quantum field theories has been investigated by Murray Gell-Mann and Francis Low [5], and the appropriate function that describes the change of the coupling $g = \sqrt{4\pi\alpha}$ with respect to a certain renormalization scale μ is

the *renormalization group equation*

$$\beta(g) = \mu \frac{\partial g}{\partial \mu} = \frac{\partial g}{\partial \log(\mu)}. \tag{1.1}$$

The modern name *β-function* was introduced by Curtis Callan and Kurt Symanzik [6, 7]. The inserted fermion loop in Fig. 1.1b modifies the photon propagator by a factor. This modification can be interpreted as a rescaling of the bare electron-photon vertex and hence be absorbed into the QED coupling constant

$$\alpha^{\text{eff}}(Q^2) = \frac{\alpha(\mu^2)}{1 - \frac{\alpha(\mu^2)}{3\pi} \log\left(\frac{Q^2}{\mu^2}\right)}. \tag{1.2}$$

This expression contains the bare coupling α, which can by fixed by obtaining experimental values at some scale μ. The scaling behavior of the interaction strength is known as *running coupling*. In quantum electrodynamics, the beta function to one-loop order is positive, which means the interaction strength increases with the energy scale.

One can explain this theoretical result using more phenomenological terms. Vacuum is not considered as purely empty space in quantum electrodynamics anymore, electrically charged virtual particles are formed and annihilated at all times. In the presence of a test charge, these virtual particle-antiparticle pairs arrange accordingly. A cloud of virtual charges will screen the original test particle, decreasing the strength of its electrical field to an outside observer. Moving closer to the test charge, therefore probing higher energy scales, diminishes the screening effect and the effective interaction increases.

The same scheme can be applied to quantum chromodynamics. Here, one considers the interaction of two fermionic quarks, mediated by the QCD gauge boson, the gluon. Opposed to QED, which is an Abelian theory, the gauge bosons of quantum chromodynamics feature self-interactions. Additionally to the fermion loop, like in Fig. 1.1b, one has to consider pure gluonic loops as well as a ghost loop.

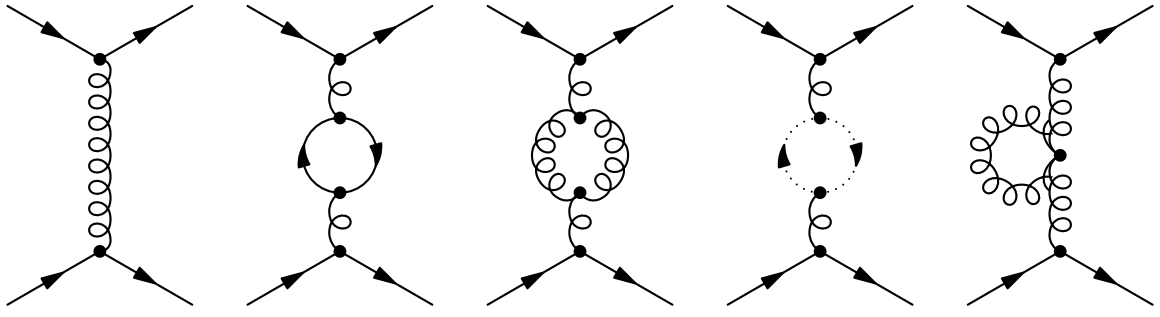

Figure 1.2: Interaction of two fermionic quarks by gluon exchange to one-loop order. The quarks are represented in the diagrams by the lines with arrows. The tree-level interaction is shown in a) with the curly line representing the gluon. In QCD, several loops can be inserted to modify the tree-level interaction: a) a quark loop, b) a pure gluonic loop, c) a ghost-loop (dotted lines) and d) a gluon self-energy insertion via the four-gluon vertex.

The additional contributions from the gluon loops (Fig. 1.2c and Fig. 1.2e) and the fact that gluons interact with themselves have a significant influence on the scaling behavior of QCD.

$$\alpha_s^{\text{eff}}(Q^2) = \frac{\alpha_s(\mu^2)}{1 + \frac{(33-2n_f)\,\alpha_s(\mu^2)}{12\pi} \log\left(\frac{Q^2}{\mu^2}\right)} \tag{1.3}$$

Equation (1.3) shows the energy scale dependence of the strong coupling α_s at one-loop order, with n_f being the number of quark flavors. One can immediately spot the difference to the QED effective coupling in Eq. (1.2): the factor to the logarithmic term has a different sign as long as the number of quark flavors is equal to or smaller than 16. Six flavors of quarks have been discovered as of now, which makes this pre-factor overall positive. So instead of an increasing coupling at large energy scales, as was the case in QED, the effective interaction strength decreases. The beta function of QCD is negative, and this phenomenon is called *asymptotic freedom*. Quarks are strongly coupled at lower energies and behave like free particles at sufficiently high energies. Returning to the picture of a test charge that is screened by virtual particles, we see the opposite effect. The term electric charge is replaced by the QCD pendant, the color charge. Moving away from a charged test particle, which is equivalent to probing lower energy scales, actually increases the color charge seen from an observer. While virtual quark-antiquark pairs do screen the color charge of the test particle, the quarks are surrounded by virtual gluon-antigluon pairs, which themselves carry color charge.

A part of the low energy regime of QCD matter is well known to us through nuclear physics. Quarks form hadrons, compound particles held together by the strong interaction, such as the neutron and the proton. Quarks have been observed indirectly by deep inelastic scattering experiments at high energies (e.g. in Ref. [8]), but single, isolated quarks are yet to be found. Trying to separate quarks from hadrons only leads to the formation of new hardons. This is known as *confinement*.

The still mysterious phenomenon of confinement stands just opposite of asymptotic freedom. We can be certain of the confining attribute of QCD thanks to numerous experiments, and the theoretical description of the running coupling constant matches up with the data as well [9]. These results suggest that quarks behave as free particles at sufficiently large energies. In such a high energy limit, the confinement is lifted and we speak of the *deconfined* phase. Much like in an ordinary electric plasma, quarks and gluons are able to move as free carriers of electric and color charge - which justifies the term *quark-gluon plasma* (QGP) to denote the deconfined phase of QCD matter. In practical terms, the deconfined phase is accessible via perturbation theory, as a small coupling justifies taking into account only diagrams at leading order in α_s.

Having established these two limits, one can assume that there has to be a region of transition, separating the two phases. Perturbation theory only works reliably at low couplings or, in the case of QCD, at asymptotically high energies. The suggested phase transition has to occur at an intermediate scale, which is not accessible through either perturbation theory or effective models.

With the rapid advancement of computing power, lattice gauge theory, as the only reliable non-perturbative method, has shed light on the subject and identified a crossover transition between confined and deconfined phases at $T \approx 160\,\text{MeV}$ [10, 11]. Lattice computations are performed at zero or very low baryonic chemical potential μ_B. Other analytical methods, such as effective models, allowed to map out different parts of the QCD phase diagram [12], as shown in Fig. 1.3.

Close to the origin of the proposed QCD phase diagram, we see the vacuum. QCD is a theory with a mass gap, which means that one needs a finite amount of energy to excite the lowest energy state or lightest particle. Below the red line, we are in the confined part of the phase diagram - quarks only exist in bound states as baryons and mesons. In the high-density region of the diagram at small temperatures, we have several phases, which all belong to the class of *color superconductors*. The

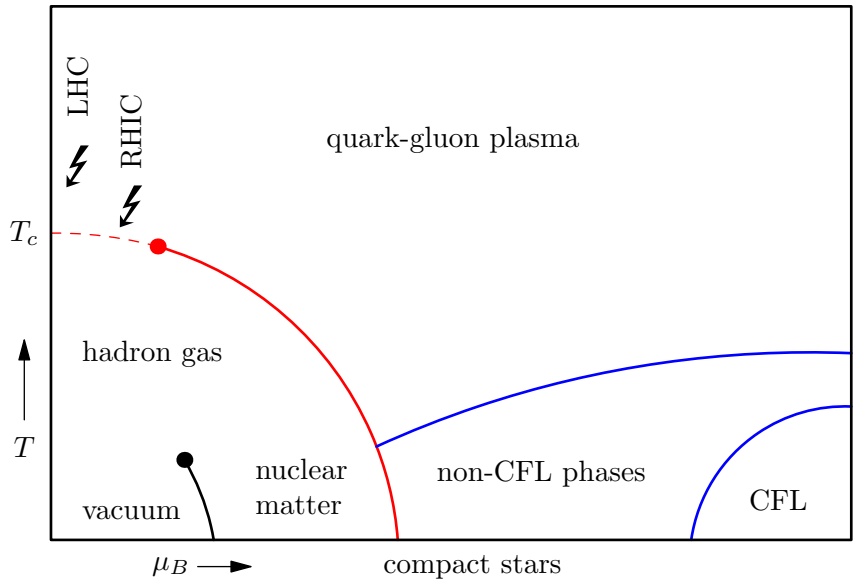

Figure 1.3: The proposed QCD phase diagram. At asymptotically high baryon densities μ_B, QCD behaves as a weakly coupled theory similar to the high-temperature scenario. Hence, the color-flavor locked (CFL) phase at such high μ_B is a well established phase theoretically. As intermediate regions in the diagram can not be accessed by perturbative methods, this phase diagram is mainly of illustrative nature. The lightning symbols indicates the state of matter which can be created in heavy-ion collisions.

so-called *color-flavor locked* (CFL) quark matter phase features a Cooper pairing mechanism and is the theoretically well established favored phase of QCD at asymptotically high densities. Next to the CFL phase, different superconducting phases have been proposed at intermediate densities [13]. This intermediate region at low temperature may be recreated in compact stars [14], which are among the most dense objects found in nature so far. The phase diagram presented in Fig. 1.3 is not known to much detail, especially at densities above the nuclear saturation density. In that regard, the CFL and non-CFL phases depicted in the diagram should be only considered as a sketch - the red line separating hadronic (nuclear) matter and quark matter (non-CFL phase) might not extend to $T = 0$, but rather a critical point [15].

The dashed red line at $T = T_c$ indicates the crossover transition between the confined hadron gas phase and the deconfined plasma phase. Next to this line are two lightning symbols. Each of them indicate the points in the phase diagram that are accessible by the heavy-ion collision experiments at LHC and RHIC.

1.2. The quark-gluon plasma in heavy-ion collisions

So far, the only natural occurrence of the would be the early universe, some $10^{-6} - 10^{-5}$ seconds after the big bang [16]. To study the deconfined phase, we hence need to rely on particle accelerators. In heavy-ion collisions, heavy nuclei, such as lead or gold, are being accelerated to near light speed. The ions acquire high center of mass energies at the order of a few hundred GeV per nucleon. Upon impact, the energy is released and the resulting QCD matter is supposedly found in the indicated points in the deconfined portion of the phase diagram (lightning symbols in Fig. 1.3). The quark-gluon plasma then undergoes a cooling process and passes through a crossover to enter the confined phase, where it *hadronizes*, as the quarks start forming hadrons below the *chemical freezeout* temperature $T < T_c$.

Two facilities are able to produce a quark-gluon plasma at the moment: the Relativistic Heavy Ion Collider (RHIC) in the Brookhaven National Laboratory and the Large Hadron Collider (LHC) at the European Organization for Nuclear Research (CERN). The former facility has played an important role by providing experimental evidence on the existence of the QGP. In the near future, the Compressed Baryonic Matter experiment (CBM) at the Facility for Antiproton and Ion Research (FAIR) in the GSI[1] Darmstadt will also be able to perform similar experiments.

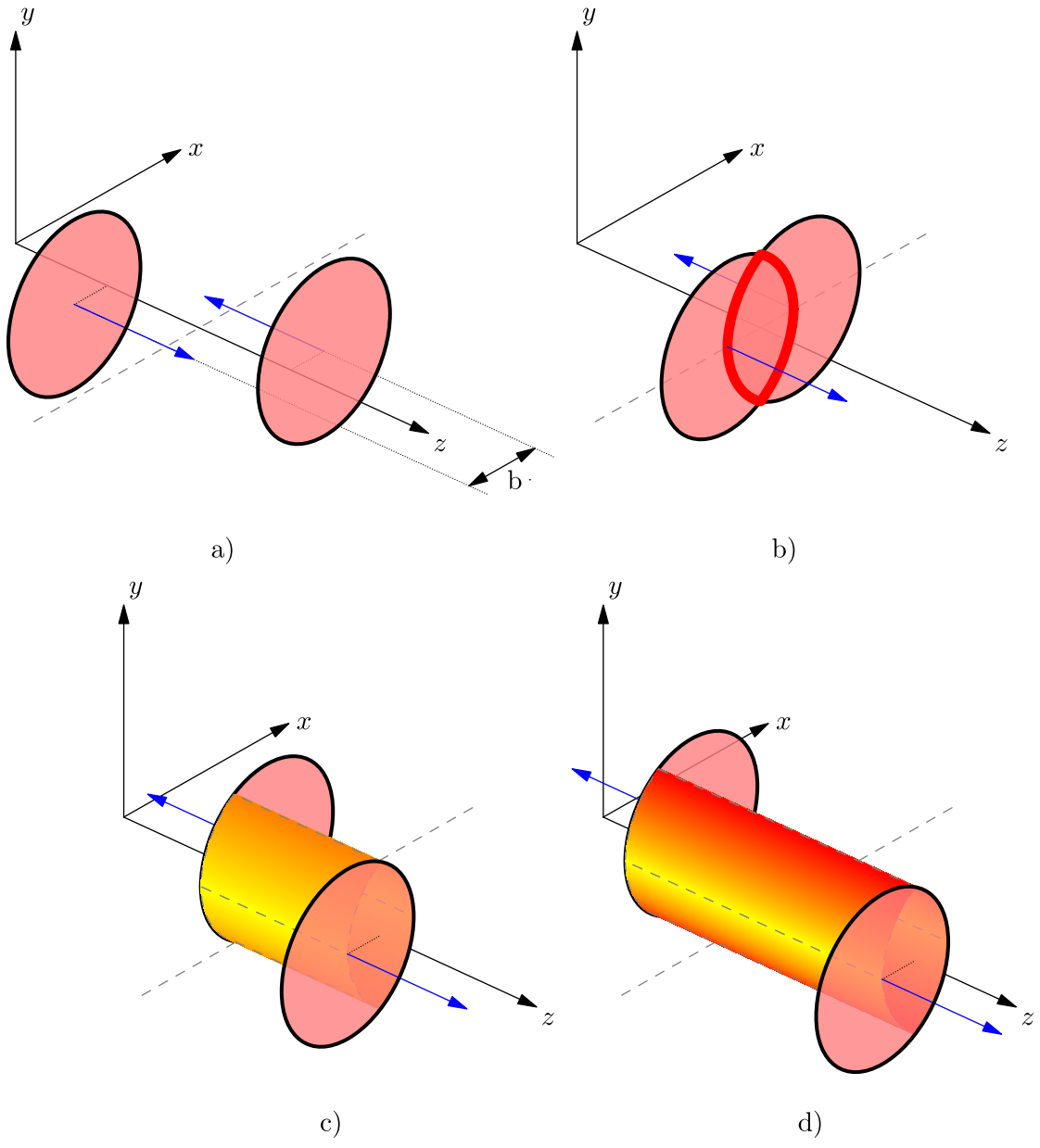

Figure 1.4: An illustration of the QGP creation at heavy-ion colliders. The red circles represent the Lorentz contracted nuclei, the direction of their velocities is indicated by the blue arrows. The interaction region is formed within the overlap of the nuclei (b). The quark-gluon plasma then expands between the receding nuclei (c) and subsequently cools down (d).

[1] Gesellschaft für Schwerionenforschung

A schematic illustration of the situation in heavy-ion colliders is shown in Fig. 1.4. In a laboratory rest frame, the accelerated nuclei appear as so-called Lorentz-contracted *pancakes*, moving at each other at near-light speed along the beam axis (Fig. 1.4a). The coordinate system is arranged so the z-coordinate points along this axis. Both nuclei are displaced by a certain amount in a transverse direction, in this case along the x-axis. The separation between the center of the nuclei is the *impact parameter* b. The plane spanned by the separation vector and the beam axis defines the *reaction plane*. When the two nuclei hit each other, an almond shaped region is formed (Fig.1.4b). The nucleons outside this interaction region are not affected by the violent collision at first and continue traveling along the beam axis. Inside the interaction region, bounded by the two receding nuclei, the quark-gluon plasma is formed (Fig. 1.4c) and cools down as the nuclei travel even further apart (Fig.1.4d).

Strong experimental evidence for the existence of the quark-gluon plasma was found by observing the phenomena of *J/ψ-suppression* [17–19], *jet-quenching* [20, 21] or *elliptic flow* [22].

J/ψ-suppression. The J/ψ particle is a meson consisting of a charm quark c and a charm antiquark $\bar{c}$. A mechanism similar to Debye screening is present in a quark-gluon plasma. Due to this screening of color charge, the $c\bar{c}$ pair will not be able to keep its bound state, if the binding radius of the meson exceeds the Debye length which depends on the temperature of the medium. Thus, the production of J/ψ particles should be suppressed by such a screening effect. The color screening is only possible if color charge carriers can move freely, which is the reason why the *anomalous J/ψ-suppression* was considered a signal for the deconfined phase and was found in heavy-ion experiments [23]. Although other explanations for the suppression were found that do no require the presence of a QGP, such as nuclear absorption models [24], the J/ψ-suppression should be mentioned here as one of the first proposed signals for the deconfined phase of QCD.

Jet-quenching. High energetic partons scatter within the QGP, their momentum vectors pointing back-to-back after the scattering event. As these partons leave the QGP, they produce hadron showers that can be measured. If the scattering takes place near an edge of the QGP, one of the partons has to travel through the entire plasma. On its way through the QGP, the parton loses energy and the produced hadrons are lesser in numbers, compared to the parton that escaped the QGP quickly.

Elliptic flow. The asymmetry of the interaction region (red almond-shaped contour in Fig. 1.4b) in non-central collisions gives rise to a density gradient in the *transverse plane* in which the interaction region lies. This directly translates to a momentum anisotropy due to the resulting pressure gradient. What is usually referred to as elliptic flow is the second Fourier coefficient v_2 of the particle distribution, which is a function of the azimuthal angle around the beam axis. Elliptic flow is an indication of re-scattering events in the plasma and is linked to collective phenomena. The good agreement of hydrodynamical calculations of v_2 with measured elliptic flow patterns provide strong evidence in favor of the quark-gluon plasma [25].

Other evidence pointing to the quark-gluon plasma is the measurement of *direct photons* that are exclusively emitted by the plasma. The QGP produces photons throughout its lifetime, even the decaying hadrons after the plasma freezeout emit photons. Unfortunately, the ratio of direct photons to all other photons emitted during a heavy-ion collision is about 1% at 2 GeV [26]. This makes the measurement rather difficult, since the secondary photons have to be filtered out. While other means of investigating the QGP have been particularly successful, such as the measurement of pions created at the freezeout surface of the plasma [27], photons are unique in the sense that they

(a) are produced throughout the whole collision,

(b) leave the plasma after creation without any further interaction,

(c) and therefore carry information about the whole evolution of the plasma.

The direct photon emission of the plasma is modified by proposed initial momentum-space anisotropies, which will be explained in detail in the next chapter. The momentum-space anisotropies considered here are not to be confused with the concept of elliptic flow, where two different pressure gradients along transverse directions arise due to the asymmetrical almond shape of non-central collisions. These initial momentum-space anisotropies will suppress the photon emission at some time after the creation of the QGP. Such suppressions as well as the overall geometry of the plasma and the photon detector placement give rise to an interesting double-peak feature in the time-dependent detector signal. An important detail is that these suppressions are only visible if the detector is placed at a low polar angle towards the beam direction. Since the quark-gluon plasma itself has only a lifetime of $\approx 13\,\mathrm{fm}/c$ ($\approx 40\,\mathrm{ys} = 40 \cdot 10^{-24}\,\mathrm{s}$), such photon signals would be the shortest pulses known to date.

This particular feature of the time-dependent direct photon signal was first proposed by Andreas Ipp et al. [28].

1.3. Goal of this thesis

The main goal of this thesis is to establish whether there is a current or future possibility of detecting a signal of photon double pulses with lengths in the order of yoctoseconds. Detecting such pulses in a time-resolved manner is not possible with ordinary electronic measuring devices and tools from attosecond physics are currently not applicable at these timescales.

A more convincing assumption is that said mechanisms, which are responsible for these double pulses also have an effect on time integrated quantities like spectra or intensity correlations as well. The advantage would be that direct photon spectra have already been measured and will be measured in the near future, for example at the LHC and at FAIR. Studies on direct photon spectra considering momentum-space anisotropies have been published recently, but they focus mainly on situations where the detector would be placed transverse to the beam axis - which is coincidentally the detector position at which the double peak feature does not appear at all.

Another possible signal may arise in the so-called Hanbury Brown - Twiss (HBT) correlations. These correlations provide a quantity that is sensitive to the full time-evolution of the quark-gluon plasma without the necessity for a time-resolving detector. It can be shown analytically that a photon source with two separated maxima in the time direction produce oscillations in the HBT correlation function, which can be related to the evolution of the anisotropies.

Both direct photon spectra as well as HBT correlations for direct photons have the necessary capability to shed light on the dynamics of the quark-gluon plasma. Their predictive ability is unfortunately thwarted by the immense practical challenge to measure these photons in the presence of an enormous amount of background photons.

Structure of the thesis

In Chapter 2, the models we use to describe the physics in the QGP are presented. The notion of initial momentum-space anisotropies is explained as well as the models that describe their evolution in time. Chapter 3 focuses on the derivation of the expressions needed to calculate the photon production rate in an anisotropic quark-gluon plasma. Integrating this differential rate allows to compute a photon

signal, which is done in Chapter 4. The phenomenology and mechanisms, which give rise to double pulses are established and pulses for different model parameters are calculated. Considering the same mechanisms, Chapter 5 explores how time-integrated single particle spectra are affected. In the same manner, Chapter 6 investigates the sensitivity of Hanbury Brown - Twiss correlations for photons with respect to these QGP model parameters.

Conventions

The calculations in this thesis are written in natural units throughout, where $c = \hbar = k_B = 1$. Quantities, such as times, photon rates or spectra, however, are given in different units which are labeled explicitly in the corresponding plots. We use following convention for the space-time metric $g_{\mu\nu} = g^{\mu\nu}$:

$$g_{\mu\nu} = \begin{pmatrix} 1 & 0 & 0 & 0 \\ 0 & -1 & 0 & 0 \\ 0 & 0 & -1 & 0 \\ 0 & 0 & 0 & -1 \end{pmatrix}. \tag{1.4}$$

A round man cannot be expected to fit in a square hole right away. He must have time to modify his shape.

– Mark Twain, Following the Equator

2

Momentum-space anisotropy in the QGP

2.1. Overview

This chapter will introduce the idea of momentum-space anisotropies in the quark-gluon plasma. These anisotropies are the basis for various phenomena in the QGP, studied in e.g. Refs. [29–34]. One particular phenomenon related to momentum-space anisotropies are the so-called *plasma instabilities*, which are a major subject of investigation at the Institute for Theoretical Physics [35–39].

Plasma instabilities in the context of an anisotropic QGP are a more general case of Weibel instabilities in an electromagnetic plasma [40]. Weibel instabilities are the driving force behind the rapid isotropization of QED plasmas, and their counterpart in quantum chromodynamics was investigated at first in Ref. [41]. This mechanism may be the cause for a short thermalization time of the plasma [42], although its particular value is still subject to scientific discussion. In Reference [43], thermalization times up to $2\,\mathrm{fm}/c$ are considered as compatible values.

The emphasis in this thesis will be put exclusively on the production of thermal photons. After a short introduction on the Bjorken model for the QGP, the ansatz for the anisotropic momentum distribution function will be explained. Concluding this chapter, the models used for the time evolution of the momentum-space anisotropy will be presented.

2.2. The Bjorken picture

We will use a model for the quark-gluon plasma pioneered by J.D. Bjorken [44], which assumes a so-called *central rapidity plateau*. This central region of the plasma shall not be a function of the space-time rapidity y, suggesting that Lorentz-boosts within this region will not change the physics in the QGP. In a more illustrative way, this is equivalent to stating that all volume elements with the same temperature of the plasma lie on an equal proper-time hyperbola in a Minkowski diagram (Fig. 2.1). The assumption is backed by experimental observations, such as recent measurements at ALICE [45], where hadron production rates show rapidity invariance near the center.

The quark-gluon plasma, which is constrained by the two proper equal time hyperbolas at $\tau = \tau_0$ and $\tau = \tau_f$, is assumed to be entirely free of hadrons. As of now, the formation time of the plasma τ_0 is still subject of investigation. Measuring the *elliptic flow* of direct photons was suggested as a way of constraining the formation time [46], but measurements do not seem to confirm photon flow [47, 48]. For an LHC scenario, Ref. [49] matched the rapidity density dN/dy to the initial temperature $T_0 = 845\,\mathrm{MeV}$ [50], giving an initial formation time of $\tau_0 = 0.088\,\mathrm{fm}/c$. The freezeout time τ_f is determined by the proper-time at which the temperature of the plasma reaches the critical

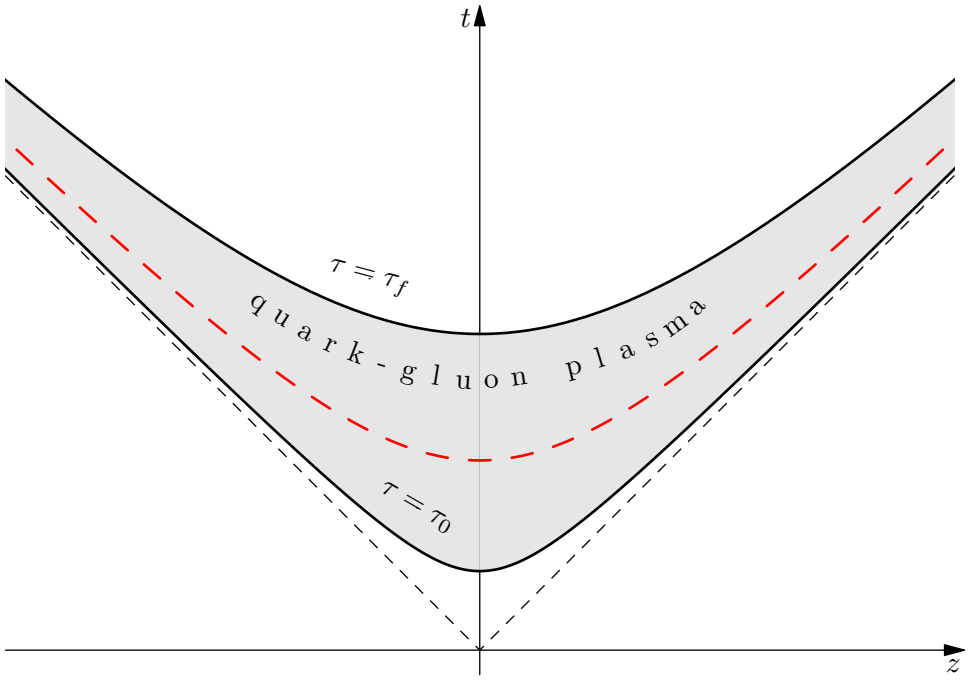

Figure 2.1: A Minkowski diagram to illustrate the Bjorken model (similar to Fig. 3 in Ref. [44]). t represents the time in the laboratory frame and z is the spatial coordinate axis along the beam. The expansion of the plasma is bounded by a light cone (straight black and dashed lines). The QGP phase (gray area) appears after a proper time τ_0 and ends with the freezeout time τ_f. The red, dashed line in between $\tau_0 < \tau < \tau_f$ symbolizes an equal proper time hyperbola within the QGP phase. The temperature of the QGP on this hyperbola is constant according to the assumption of rapidity invariance.

value $T(\tau) = T_c$. Using the 1D Bjorken expansion, the temperature evolution is given by

$$T(\tau) = T_0 \left(\frac{\tau_0}{\tau}\right)^{\frac{1}{3}}, \tag{2.1}$$

which leads to a freezeout time $\tau_f \approx 13\,\mathrm{fm}/c$ for $T_c = 160\,\mathrm{MeV}$.

Additionally, the expansion of the QGP will only occur in the longitudinal direction along the beam. This is still a good approximation for early times [51].

2.3. The Romatschke-Strickland ansatz

The major contributor to the phenomenology of the double peak effect is the possibility of momentum anisotropies in the quark-gluon plasma. Figure 2.2 illustrates this in a rather simple fashion[1].

The momentum distribution of the partons evolves from an initially prolate form into an oblate form at later times. Somewhere in between, the momentum distribution has to reach a spherical, isotropic form. This time is denoted by τ_0 and for our calculations, represents the formation time of the quark-gluon plasma.

After a time $\tau > \tau_0$ (Fig. 2.2a), the two Lorentz contracted nuclei (indicated by the thick, black

[1]These momentum anisotropies describe the anisotropy between longitudinal and transverse directions, and should not be confused with pressure gradients within the transverse plane, which are responsible for the elliptic flow.

lines) have moved away from each other, and the plasma between them is expanding primarily in that direction. High momentum partons, which have a high momentum component in the direction of the expanding plasma, will leave the central region of the plasma very quickly (Fig. 2.2b). The only partons remaining in the central area will have momentum components primarily in the perpendicular or transverse direction $\langle p_L^2 \rangle < 2\langle p_T^2 \rangle$. Since we employ the Bjorken model for our computations, we will restrict ourselves only to this central region.

For greater times $\tau \gg \tau_0$, the flat nuclei have receded even further and the plasma expands in the same manner. The plasma will eventually reach an isotropic state again.

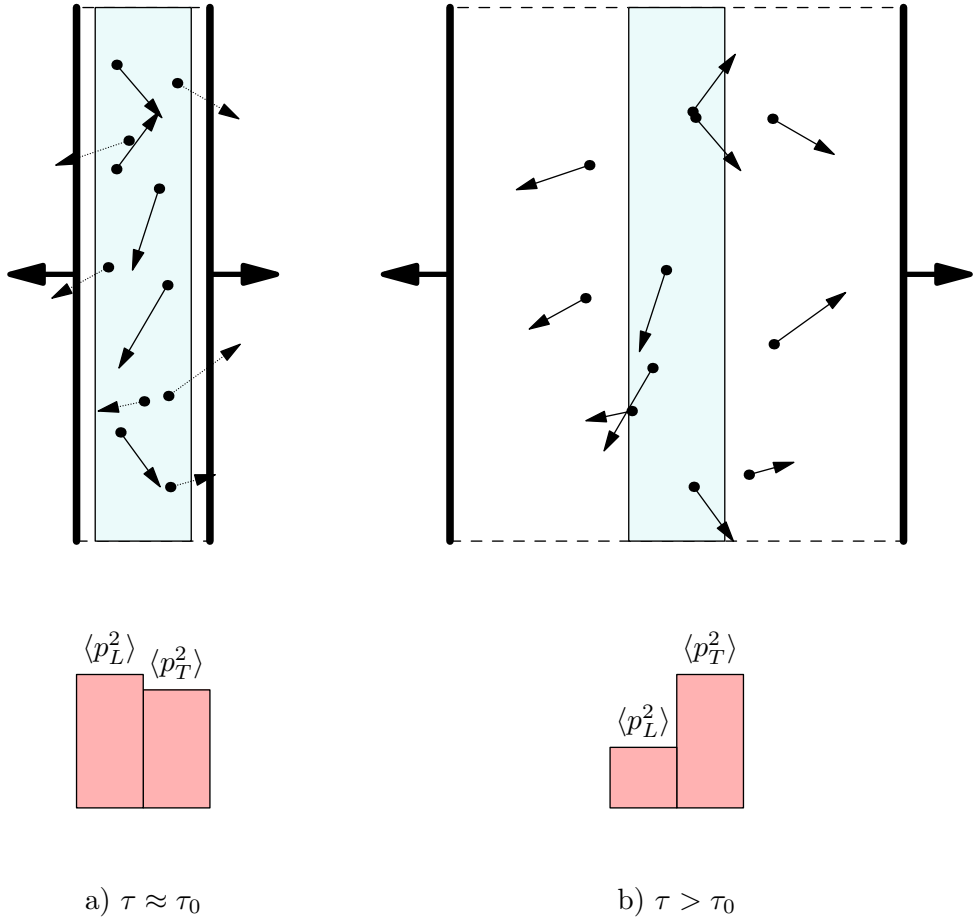

a) $\tau \approx \tau_0$ b) $\tau > \tau_0$

Figure 2.2: This sketch illustrates the buildup of momentum anisotropy in the quark-gluon plasma. Each picture depicts some partons (dots) and their momenta (arrows) at a certain time τ. a) is a snapshot of a time τ very shortly after τ_0. Most of the partons are within the central rapidity plateau (light blue, shaded area). At a later time, we see in b) how the partons with primarily longitudinal momenta have already traveled away from the central region. The partons left behind have mostly high momenta in the transverse direction. The bars at the bottom represent the average of the momentum components within the central area. Note that this figure depicts a two dimensional scenario with two degrees of freedom, hence $\langle p_L^2 \rangle = \langle p_T^2 \rangle$ for the isotropic case.

To summarize the above, one needs to modify the quark and gluon distribution functions in a way that momentum anisotropies can be incorporated. P. Romatschke and M. Strickland proposed a

distribution function, which is now known as the RS-ansatz [52]:

$$f(\mathbf{p}) = f_{\text{iso}}(\sqrt{\mathbf{p}^2 + \xi(\mathbf{n}\cdot\hat{\mathbf{p}})^2}). \tag{2.2}$$

The anisotropy parameter

$$\xi = \frac{\langle p_T^2\rangle}{2\langle p_L^2\rangle} - 1, \tag{2.3}$$

is defined in the range $-1 < \xi < \infty$ and rescales an isotropic distribution function f_{iso}. $\xi > 0$ contracts the distribution function, while $\xi < 0$ stretches it (see Fig. 2.3). If $\xi = 0$, the isotropic scenario is recovered. For our purposes, the anisotropy will only quench the distribution function along the longitudinal direction z ($\mathbf{n} = \hat{\mathbf{p}}_z$):

$$f_{q,g}(\mathbf{p}) = \left[e^{\sqrt{p_x^2+p_y^2+(1+\xi)p_z^2}/T} \pm 1\right]^{-1}. \tag{2.4}$$

The upper sign corresponds to the fermionic quark distribution function, whereas the lower sign corresponds to the bosonic gluon one. Throughout this thesis, the above form (2.4) of the distribution

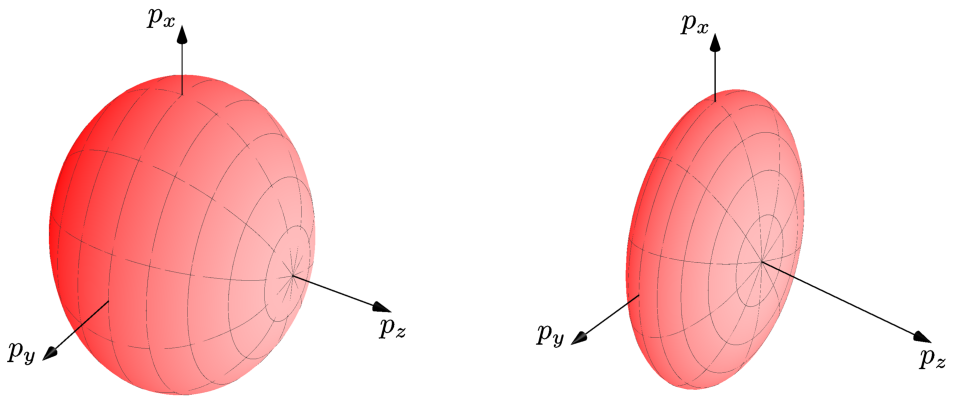

a) $\xi = 0$ b) $\xi = 5$

Figure 2.3: The shape of an anisotropic distribution function from Eq. (2.4) at different anisotropy parameters ξ. These plots depict equal-value surfaces of the anisotropic distributions. The axes label the components of the momentum vector $\mathbf{p}$, where $\hat{p}_z$ is the direction along the beam axis (see Fig. 1.4).

functions is implied, without the anisotropy parameter ξ explicitly written.

2.4. Model for the time evolution

This section shortly recaps the interpolating model for the temperature and the anisotropy parameter [51, 53].

The two asymptotic limits, as described in Ref. [51], are the hydrodynamical expansion [44] and the so-called free streaming limit [54], both in 1+1 dimensions. In the first case, it is assumed that the partons in the plasma undergo an ideal hydrodynamic evolution. This is only valid, if the momentum distribution is isotropic ($\xi = 0$). For the correct hydrodynamical description of an anisotropic QGP,

see Reference [55]. Free-streaming expansion, on the other hand, neglects all parton interaction and is applicable to anisotropic momentum distributions.

In the ideal hydrodynamic case, we have the following expressions for the anisotropy parameter and the temperature. Note that the hard momentum scale p_{hard} is strictly only equal to the temperature in the isotropic case. Since the momentum distribution is assumed to be isotropic at the formation time τ_0 of the plasma, there is a well defined initial temperature T_0:

$$\xi_H(\tau) = 0, \tag{2.5a}$$

$$p_{\mathrm{hard}}(\tau) = T_H(\tau) = T_0 \left(\frac{\tau_0}{\tau}\right)^{\frac{1}{3}}. \tag{2.5b}$$

A significant parameter in the evolution of the anisotropic quark-gluon plasma is the *isotropization time* τ_{iso}, which corresponds to an approximate time, at which the plasma becomes isotropic again. For a pure hydrodynamical evolution with an isotropic momentum distribution, $\tau_{\mathrm{iso}} = \tau_0$.

If one considers the free-streaming expansion, the plasma never reaches momentum-space isotropy, and thus $\tau_{\mathrm{iso}} \to \infty$:

$$\xi_{\mathrm{FS}} = \frac{\tau^2}{\tau_0^2} - 1, \tag{2.6a}$$

$$p_{\mathrm{hard}}(\tau) = T_0. \tag{2.6b}$$

These two extreme cases of ideal hydrodynamical evolution and free-streaming expansion can now be extended to a more general case of momentum-space broadening [56] due to interactions:

$$\xi(\tau) = \left(\frac{\tau}{\tau_0}\right)^{\delta} - 1, \tag{2.7a}$$

$$p_{\mathrm{hard}}(\tau) = T_0 \left(\frac{\tau_0}{\tau}\right)^{(1-\delta/2)/3}. \tag{2.7b}$$

The newly introduced parameter δ can be varied between the hydrodynamical case ($\delta \to 0,\ \xi \to 0$) and the non-interacting free-streaming variant ($\delta \to 2$). Different values for δ correspond to various expansion mechanisms (Table 2.1).

	δ
ideal hydrodynamics	0
plasma instabilities	$1/6 < \delta < 1/2$
collisional broadening	2/3
non-interacting free-streaming	2

Table 2.1: Plasma expansion mechanisms and their corresponding values for the parameter δ [51].

Because of uncertainties on which expansion mechanism enters in the plasma evolution at which time, Ref. [51] chose an approach via a smeared step function. This step function governs the change of δ from e.g. 2 or 2/3 to $\delta = 0$ at approximately the isotropization time τ_{iso} and thus delivers a smooth transition

from the collisional broadening or the free-streaming scenario to the hydrodynamical evolution:

$$\lambda(\tau, \tau_{\rm iso}, \gamma) \equiv \frac{1}{2}\left(\tanh\left[\frac{\gamma(\tau - \tau_{\rm iso})}{\tau_{\rm iso}}\right] + 1\right). \tag{2.8}$$

The inverse of the coefficient γ defines the smoothness of this transition.

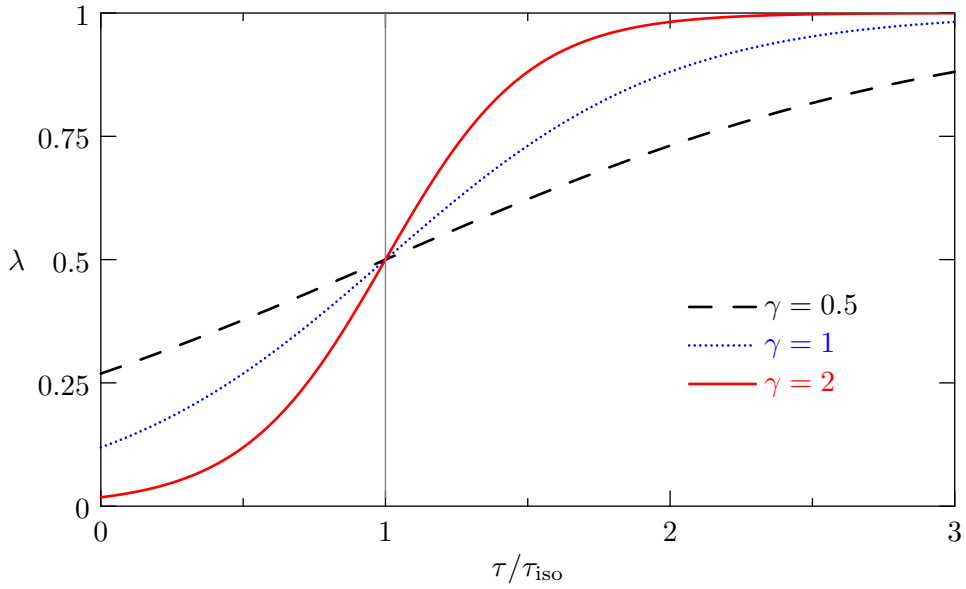

Figure 2.4: The smeared step function $\lambda(\tau, \tau_{\rm iso}, \gamma)$ from Eq. (2.8) for different transition widths γ. This step function enters the model for the time-evolution in Eq. (2.10) and controls the transition of the different plasma phases in Table 2.1.

ξ and $p_{\rm hard}$ now read:

$$\xi(\tau) = \left(\frac{\tau}{\tau_0}\right)^{\delta[1-\lambda(\tau,\tau_{\rm iso},\gamma)]} - 1, \tag{2.9a}$$

$$p_{\rm hard}(\tau) = T_0\, \bar{\mathcal{U}}^{1/3}(\tau). \tag{2.9b}$$

The hard momentum scale, which we will effectively use as our time-dependent temperature, is defined via a helper function $\bar{\mathcal{U}}$. We use the interpolating model that enforces fixed final entropy (multiplicity):

$$\bar{\mathcal{U}}(\tau) \equiv \frac{\mathcal{U}(\tau)}{\mathcal{U}(\tau_{\rm iso}^+)}, \tag{2.10a}$$

$$\mathcal{U}(\tau) \equiv \left\{\mathcal{R}\left([\frac{\tau_{\rm iso}}{\tau}]^\delta - 1\right)\right\}^{\frac{3\lambda(\tau)}{4}} \left(\frac{\tau_{\rm iso}}{\tau_0}\right)^{\frac{1-\delta[1-\lambda(\tau)]}{2}}, \tag{2.10b}$$

$$\mathcal{U}(\tau_{\rm iso}^+) \equiv \lim_{\tau\to\tau_{\rm iso}^+} \mathcal{U}(\tau) = \left\{\mathcal{R}\left([\frac{\tau_{\rm iso}}{\tau}]^\delta - 1\right)\right\}^{\frac{3}{4}} \left(\frac{\tau_{\rm iso}}{\tau_0}\right), \tag{2.10c}$$

$$\mathcal{R}(\xi) \equiv \frac{1}{2}\left(\frac{1}{1+\xi} + \frac{\arctan(\sqrt{\xi})}{\sqrt{\xi}}\right). \tag{2.10d}$$

Fixed final multiplicity is in contrast to fixed initial conditions. By setting the initial conditions to

a fixed value, the entropy generation $\Delta S/S_0$ will increase with respect to τ/τ_{iso} (Fig. 6 in Ref. [51]). If one requires the entropy generation to be within a certain bound, e.g. less than 10% or 20%, the isotropization time τ_{iso} will have upper bounds as well. These upper bounds would restrict the isotropization time for the free-streaming model to values, which are well below the limit of what is still regarded as possible, not yet ruled out values for τ_{iso}.

The isotropization time will have a large impact on the final photon signal, which is why we aim to max out reasonable values for τ_{iso}. Using the model with enforced fixed final multiplicity ensures that the hard scale p_{hard} will be independent of the isotropization times for large τ/τ_0 (Fig. 2.5).

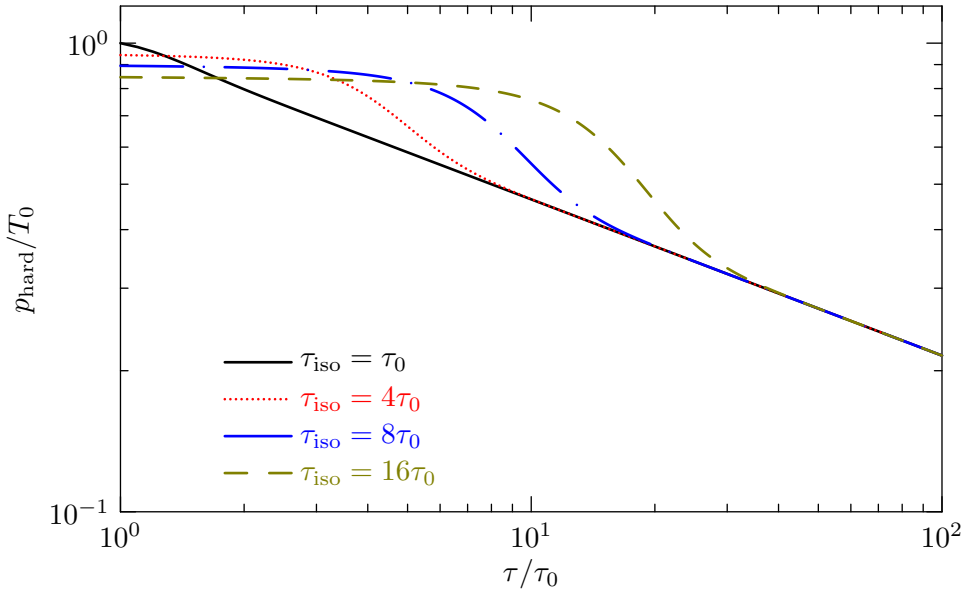

Figure 2.5: Evolution of the momentum hard scale p_{hard} with enforced final fixed entropy. Notice how different isotropization times τ_{iso} lead to a slightly different initial value of p_{hard} at $\tau = \tau_0$. $\gamma = 10$, $\delta = 2$.

As one can see in Fig. 2.6, the anisotropy parameter ξ reaches a maximum at $\tau \approx \tau_{\text{iso}}$. This is apparently in contradiction to the definition given earlier, which said that τ_{iso} gives an approximate time at which ξ becomes small again ($\xi \to 0$). Figure 2.6 uses a very small value for γ, which is equivalent to a very smooth and long transition of the different phases in the QGP evolution.

Changing the parameter to a larger value creates a sharper transition, as seen in Fig. 2.7. The isotropization time then really becomes a proper time, at which ξ returns to a small value, compared to the maximum.

The models for both the quark-gluon plasma and the evolution of the anisotropy and temperature presented in this chapter allow to compute several quantities during the lifespan of the QGP. To obtain a photon signal, one needs to know the differential photon production rate in the plasma. The expressions needed for the calculation of this differential rate will be derived in the next chapter.

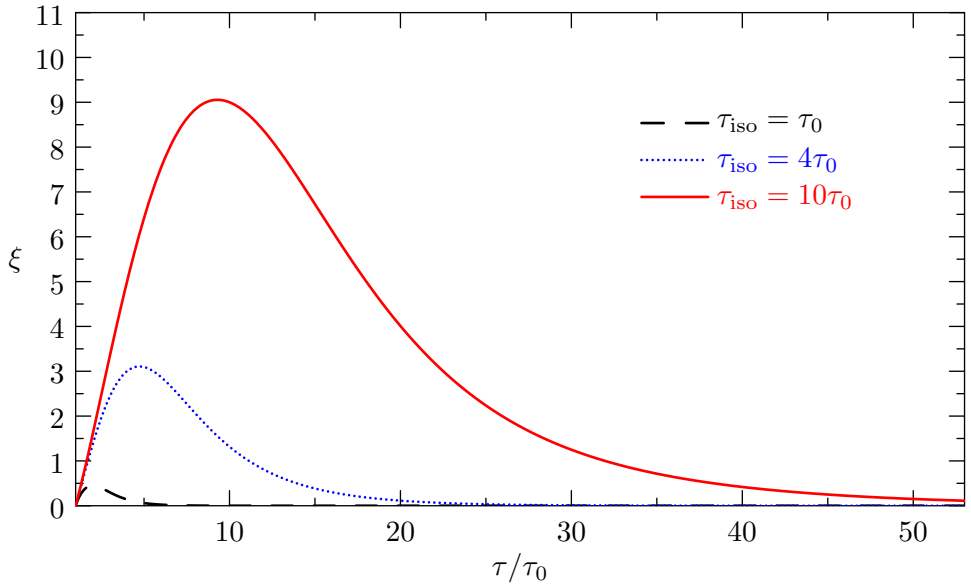

Figure 2.6: Time evolution of the anisotropy parameter for a small transition parameter $\gamma = 0.5$ and a free-streaming scenario ($\delta = 2$).

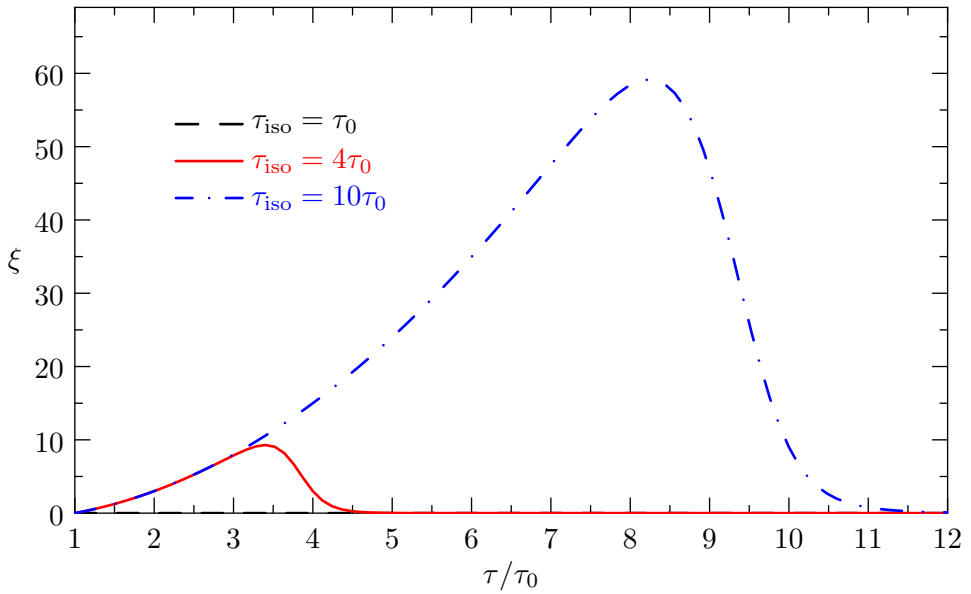

Figure 2.7: The same time evolution as in Fig. 2.6, but with a larger transition parameter. The anisotropy at $\tau_{\text{iso}} = \tau_0$ is not visible anymore, as it is quite close to 0. At sharper transitions, the anisotropy parameter is closer to 0 at τ_{iso}. $\gamma = 25$, $\delta = 2$.

Light thinks it travels faster than anything but it is wrong. No matter how fast light travels, it finds the darkness has always got there first, and is waiting for it.

– Terry Pratchett, Reaper Man

3
Photon production

3.1. Overview

In this section, we calculate the photon production rate EdR/d^3p in the quark-gluon plasma, taking into account momentum anisotropies. As we have established in the introduction, we can apply the method of perturbation theory and include only processes to leading order in the strong coupling α_s.

The first analytic result of photon production rates from a quark-gluon plasma was derived by J. Kapusta, P. Lichard and D. Seibert [57]. This result was calculated using the hard thermal loop resummation method by E. Braaten and R.D. Pisarski [58] to deal with the divergences (see Section 3.3 for details). It has then been further extended by S. Turbide and C. Gale [50] to account for the space-time evolution of the plasma.

The following computations of the hard (Section 3.2) and soft parts (Section 3.3) for an anisotropic QGP are similar to reference [57] - with the difference that non-isotropic distribution functions from Ref. [52] are used. Divergences that occur in both the hard and soft contributions will be discussed in Section 3.4 on the numerical integration.

Z.-T. Liang and X.-N. Wang [59] proposed a mechanism for non-central heavy ion collisions that could lead to quarks in a QGP with an initial polarization. As shown in Ref. [60], this initial polarization can transfer to photon polarization. The detection of direct photons is an experimental challenge as it is, without having to pay much attention to polarization states. The possibility of polarized quarks is therefore omitted in this thesis.

The calculations in this chapter are based on the works by B. Schenke, M. Strickland [61] and A. Ipp [60, 62]. As in Ref. [61], we will not take into account bremsstrahlung.

3.2. Hard contribution

There are two processes that fall into the category of so-called *hard contributions*[1] to the lowest order in α_s which each yield a photon:

- Compton scattering of quarks and antiquarks ($qg \to q\gamma$, $\bar{q}g \to \bar{q}\gamma$)
- quark-antiquark annihilation ($\bar{q}q \to g\gamma$).

[1] Note that these *hard contributions* should not be mixed up with *hard photons*, which is usually the term used for high-momentum photons ($p > 6$ GeV).

Photon rates from the mentioned processes exhibit divergences for low exchanged momenta. The corresponding scattering amplitudes can only be trusted at high or *hard* momentum transfer regions. At low momentum transfer regions, the scattering amplitudes show a similar divergence in the region of high momentum transfer, thus being only reliable for low or *soft* transferred momenta.

An overview of the Feynman-graphs corresponding to the processes of the hard contribution is shown in Fig. 3.1. In the S-matrix formalism, we then to evaluate these diagrams to obtain the scattering

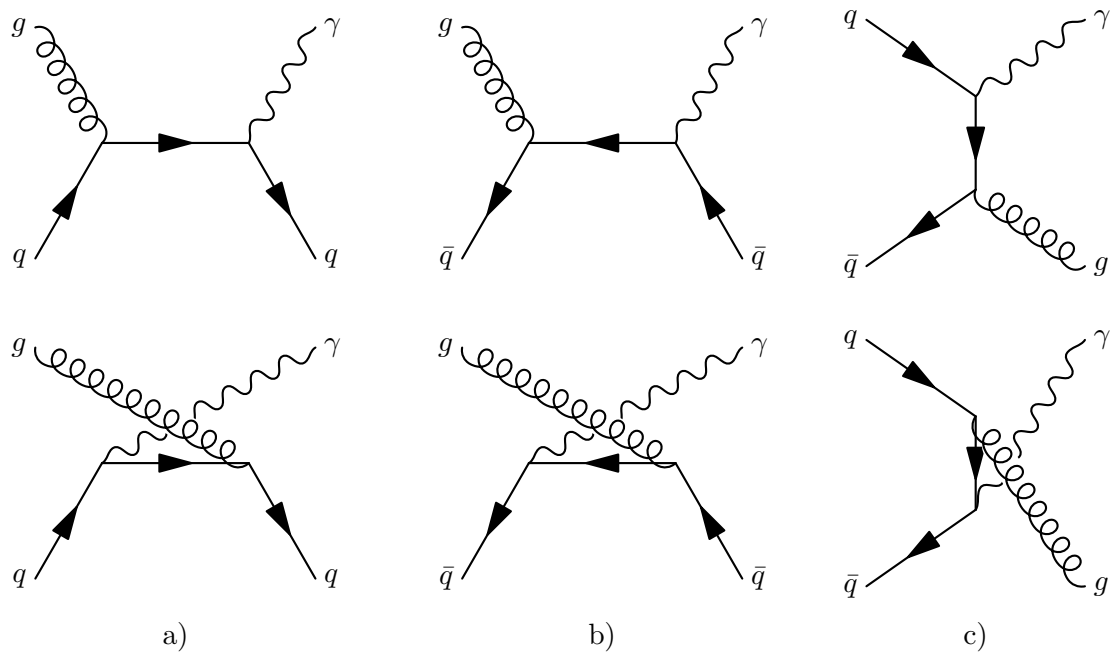

Figure 3.1: The graphs corresponding to the three leading order processes for the hard contribution: a) $qg \to q\gamma$, b) $\bar{q}g \to \bar{q}\gamma$ and c) $\bar{q}q \to g\gamma$. We use the common symbols for (anti)quarks (straight lines), gluons (curly lines) and photons (wiggly lines). The time coordinate points to the right.

amplitudes, which we use to compute the photon production rate. As pointed out by e.g. Boyanovsky and de Vega [63], the S-matrix formalism involves an elementary flaw. This flaw is the use of asymptotic in- and outgoing states, which the scattering matrix connects. While it is obvious to assume that particles are well described by asymptotic states in scattering experiments, the matter is not so trivial in the case of a QGP. Due to the fast hadronization of the plasma, we have to think about *finite lifetime effects* and the role of quarks and gluons as *transient* particles. Reference [63] came to the conclusion that photon production rates calculated via the scattering matrix differ from their result obtained using the real-time (RT) formalism by a factor of 2-4 in the range 200 MeV $< p <$ 2.5 GeV. At higher energies, the photon rate from the S-matrix approach drops off, while the result using the RT-formalism shows a flatter plateau. This should be kept in mind when calculating spectra and drawing conclusions. We will stick to the S-matrix approach to calculate scattering amplitudes, as we want to compute the photon rate as a function of the anisotropy parameter ξ, following the work of Schenke and Strickland [61].

3.2.1. Quark Compton scattering

The Compton scattering contributions for quarks are shown in Fig. 3.1a and Fig. 3.1b, or detailed in Fig. 3.2. Feynman rules used for this calculation are listed in Appendix A. The scattering amplitude

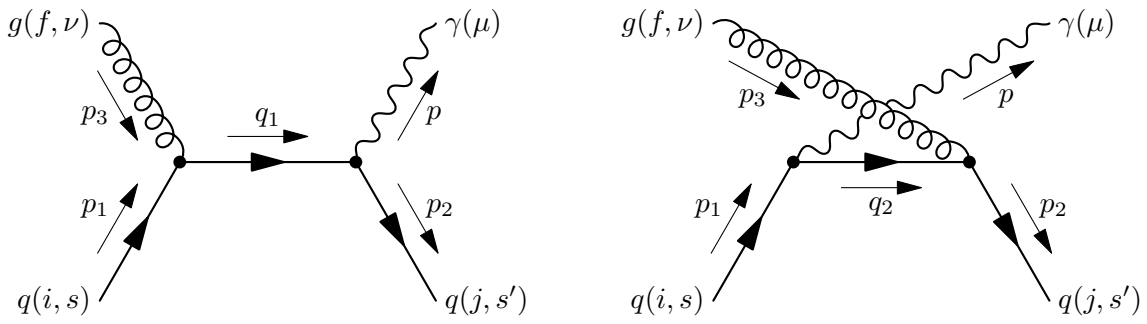

s-channel (t,u)-channel

Figure 3.2: The detailed Compton-scattering diagram ($qg \to q\gamma$, Fig. 3.1a). Gluons have a color (f) and a Lorentz index (ν), (anti)quarks feature spin (s', s) and color indices (j, i), photons have a Lorentz index (μ).

for the sum of the two channels (plus sign due to the exchange of the bosonic gluon and the photon) can be written as

$$\begin{aligned} i\mathcal{M}_{qg\to q\gamma} = {} & \bar{u}^{s'}_{\alpha}(p_2)c^{\dagger}_{j}(-ieQ\,\gamma^{\mu}_{\alpha\beta})\varepsilon^{*}_{\mu}(p)\frac{i(\not{q}_1+m)_{\beta\gamma}}{q_1^2-m^2}\varepsilon_{\nu}(p_3)a_f(-ig_sT^f\gamma^{\nu}_{\gamma\delta})u^{s}_{\delta}(p_1)c_i \\ & + \bar{u}^{s'}_{\alpha}(p_2)c^{\dagger}_{j}(-ig_sT^f\gamma^{\nu}_{\alpha\beta})\varepsilon_{\nu}(p_3)a_f\frac{i(\not{q}_2+m)_{\beta\gamma}}{q_2^2-m^2}\varepsilon^{*}_{\mu}(p)(-ieQ\,\gamma^{\mu}_{\gamma\delta})u^{s}_{\delta}(p_1)c_i. \end{aligned} \tag{3.1}$$

u and $\bar{u}$ are quark and antiquark spinors respectively. The ε are polarization tensors for either photons or gluons. g_s is the strong coupling parameter, related to the coupling constant α_s via $g_s = \sqrt{4\pi\alpha_s}$. In accordance with Ref. [61], $\alpha_s = 0.32$ was used. a ($a^{\dagger}$) and c ($c^{\dagger}$) are color annihilation (creation) operators, the former act in the adjoint color space, while the latter acts in the fundamental color space. The gauge group matrices are denoted by T. The Greek subscripts ($\alpha, \beta, \gamma, \delta$) at the spinor u, the Dirac matrices γ^{μ} (with Lorentz index μ) and the fermionic propagators (q_1, q_2) represent spinor indices.

To build the modulus of the scattering amplitude, we need to write down the conjugate $(i\mathcal{M}_{qg\to q\gamma})^{\dagger}$ first. By multiplying Eq. (3.1) with its modulus (see Appendix B), we obtain the squared modulus:

$$\begin{aligned} |\mathcal{M}_{qg\to q\gamma}|^2 = {} & (i\mathcal{M}_{qg\to q\gamma})^{\dagger}(i\mathcal{M}_{qg\to q\gamma}) \\ = {} & e^2Q^2g_s^2\left(c^{\dagger}_{i}T^fc_jc^{\dagger}_{j}T^fc_i\varepsilon_{\mu'}(p)\varepsilon^{*}_{\nu'}(p_3)a^{\dagger}_{f}\varepsilon^{*}_{\mu}(p)\varepsilon_{\nu}(p_3)a_f\right) \\ & \times\left\{\bar{u}^{s}_{\delta'}(p_1)\gamma^{\mu'}_{\delta'\gamma'}\frac{(\not{q}_2+m)_{\gamma'\beta'}}{q_2^2-m^2}\gamma^{\nu'}_{\beta'\alpha'}u^{s'}_{\alpha'}(p_2)\bar{u}^{s'}_{\alpha}(p_2)\gamma^{\mu}_{\alpha\beta}\frac{(\not{q}_1+m)_{\beta\gamma}}{q_1^2-m^2}\gamma^{\nu}_{\gamma\delta}u^{s}_{\delta}(p_1)\right. \\ & + \bar{u}^{s}_{\delta'}(p_1)\gamma^{\mu'}_{\delta'\gamma'}\frac{(\not{q}_2+m)_{\gamma'\beta'}}{q_2^2-m^2}\gamma^{\nu'}_{\beta'\alpha'}u^{s'}_{\alpha'}(p_2)\bar{u}^{s'}_{\alpha}(p_2)\gamma^{\nu}_{\alpha\beta}\frac{(\not{q}_2+m)_{\beta\gamma}}{q_2^2-m^2}\gamma^{\mu}_{\gamma\delta}u^{s}_{\delta}(p_1) \\ & + \bar{u}^{s}_{\delta'}(p_1)\gamma^{\nu'}_{\delta'\gamma'}\frac{(\not{q}_1+m)_{\gamma'\beta'}}{q_1^2-m^2}\gamma^{\mu'}_{\beta'\alpha'}u^{s'}_{\alpha'}(p_2)\bar{u}^{s'}_{\alpha}(p_2)\gamma^{\mu}_{\alpha\beta}\frac{(\not{q}_1+m)_{\beta\gamma}}{q_1^2-m^2}\gamma^{\nu}_{\gamma\delta}u^{s}_{\delta}(p_1) \\ & \left. + \bar{u}^{s}_{\delta'}(p_1)\gamma^{\nu'}_{\delta'\gamma'}\frac{(\not{q}_1+m)_{\gamma'\beta'}}{q_1^2-m^2}\gamma^{\mu'}_{\beta'\alpha'}u^{s'}_{\alpha'}(p_2)\bar{u}^{s'}_{\alpha}(p_2)\gamma^{\nu}_{\alpha\beta}\frac{(\not{q}_2+m)_{\beta\gamma}}{q_2^2-m^2}\gamma^{\mu}_{\gamma\delta}u^{s}_{\delta}(p_1)\right\}. \end{aligned} \tag{3.2}$$

The two channels (Fig. 3.2) for the $qg \to q\gamma$ process feature two inbound particles, a quark and a

gluon, and two outgoing particles, another quark and a photon. In order to get the right pre-factor to every process we want to calculate, we need to know the number of all possible states of the outgoing particles. To correctly account for these degeneracies, one has to sum $|\mathcal{M}|^2$ over all outgoing (final) states.

To include our lack of knowledge about the polarization state of the incoming quarks, we also need to multiply by the average of each of these states. First, we can calculate the sum of spins s, s'. The completeness relation for free (positive energy) Dirac spinors is particularly useful for this task:

$$\sum_s u^s_\delta(p_1)\bar{u}^s_{\delta'}(p_1) = (\not{p}_1 + m)_{\delta\delta'}. \tag{3.3}$$

The sum is performed the same way for the outgoing spinors s'. To account for the spin degeneracy of the incoming quark with spin s, we need to keep in mind a factor of $\frac{1}{2}$.

Similar considerations have to be given for the polarizations of the incoming gluon and the outgoing photon. In this case, we need to make use of the Ward-Takahashi identity.

A longer and more precise derivation of the identity can be found in e.g. Refs. [64, 65], we will only show how the identity can be used to replace the polarization sums.

The Ward-Takahashi identity states that a scattering amplitude with an incoming or outgoing photon or gluon vanishes, if a polarization vector ε_μ is replaced by a momentum vector p_μ:

$$\mathcal{M} = \varepsilon_\mu \mathcal{M}^\mu \to p_\mu \mathcal{M}^\mu = 0. \tag{3.4}$$

We start off by writing Eq. (3.1) in a slightly more minimalist form and omit spinor indices for the time being ($q_1 = p + p_2$ and $q_2 = p_1 - p$):

$$\begin{aligned} i\mathcal{M} = &-\overbrace{e g_s Q c_j^\dagger T^f c_j}^{C} \varepsilon^*_\mu(p)\varepsilon_\nu(p_3) \\ &\times \bar{u}^{s'}(p_2)\left\{\gamma^\mu \frac{i}{\not{p} + \not{p}_2 - m}\gamma^\nu + \gamma^\nu \frac{i}{\not{p}_1 - \not{p} - m}\gamma^\mu\right\} u^s(p_1). \end{aligned} \tag{3.5}$$

The photon polarization vector $\varepsilon^*_\mu(p)$ is replaced by p_μ:

$$i\mathcal{M} = -C\ \varepsilon_\nu(p_3)\bar{u}^{s'}(p_2)\left\{i\frac{\not{p}}{\not{p} + \not{p}_2 - m}\gamma^\nu + i\gamma^\nu \frac{\not{p}}{\not{p}_1 - \not{p} - m}\right\} u^s(p_1). \tag{3.6}$$

Each of the numerators can now be expanded by adding and subtracting $\not{p}_2 - m$ and $\not{p}_1 - m$ respectively:

$$\begin{aligned} i\mathcal{M} = -C\ \varepsilon_\nu(p_3)\bar{u}^{s'}(p_2)\Bigg\{&i\frac{(\not{p} + \not{p}_2 - m) - (\not{p}_2 - m)}{\not{p} + \not{p}_2 - m}\gamma^\nu \\ &+ i\gamma^\nu \frac{-(\not{p}_1 - \not{p} - m) + (\not{p}_1 - m)}{\not{p}_1 - \not{p} - m}\Bigg\} u^s(p_1). \end{aligned} \tag{3.7}$$

The fractions yield a gamma matrix each with a different sign, canceling each other:

$$i\mathcal{M} = -C\ \varepsilon_\nu(p_3)\bar{u}^{s'}(p_2)\left\{\cancel{i\gamma^\nu} - i\frac{\not{p}_2 - m}{\not{p} + \not{p}_2 - m}\gamma^\nu - \cancel{i\gamma^\nu} + i\gamma^\nu \frac{\not{p}_1 - m}{\not{p}_1 - \not{p} - m}\right\} u^s(p_1). \tag{3.8}$$

The remaining fractions are equal to zero, as we can apply the free Dirac equation to each numerator:

$$\begin{aligned} \bar{u}^{s'}(p_2)(\not{p}_2 - m) = 0, \\ (\not{p}_1 - m)u^s(p_1) = 0, \end{aligned} \tag{3.9}$$

and thus we have shown that (3.4) holds for our quark Compton scattering diagram. To show how the polarization sums can be replaced, we choose our photon or gluon momentum p to point into the z-direction:

$$p = \begin{pmatrix} |\mathbf{p}| \\ 0 \\ 0 \\ |\mathbf{p}| \end{pmatrix}. \tag{3.10}$$

The Ward-Takahashi identity (3.4) then tells us that

$$\mathcal{M}^{(0)} = \mathcal{M}^{(3)}. \tag{3.11}$$

Choosing our transverse polarization vectors in a similar fashion, $\varepsilon_1 = (0, 1, 0, 0)$ and $\varepsilon_2 = (0, 0, 1, 0)$, we can write a sum of polarization vectors

$$\sum_{\text{pol.}} \varepsilon^*_\mu(p_3)\varepsilon_\nu(p_3)\mathcal{M}^\mu\mathcal{M}^{*,\nu} = |M^{(1)}|^2 + |M^{(2)}|^2. \tag{3.12}$$

Adding (3.11) gives us our replacement rule:

$$\begin{aligned} \sum_{\text{pol.}} \varepsilon^*_\mu\varepsilon_\nu\mathcal{M}^\mu\mathcal{M}^{*,\nu} &= |M^{(1)}|^2 + |M^{(2)}|^2 + |M^{(3)}|^2 - |M^{(0)}|^2 \\ &= -g_{\mu\nu}\mathcal{M}^\mu\mathcal{M}^{*,\nu}. \end{aligned} \tag{3.13}$$

This replacement is valid as long as the polarization vectors are to be found in a scalar product with a scattering matrix element. The gluon polarization sum can therefore be replaced by the metric tensor:

$$\sum_{\text{pol.}} \varepsilon^*_{\nu'}(p_3)\varepsilon_\nu(p_3) \to -g_{\nu\nu'}. \tag{3.14}$$

By assuming the gluons to be transversely polarized, we can omit the emission of ghosts in this polarization sum.

The same can be applied to the polarization sum for the photons:

$$\sum_{\text{pol.}} \varepsilon^*_{\mu'}(p)\varepsilon_\mu(p) \to -g_{\mu\mu'}. \tag{3.15}$$

Fortunately, the two minus signs cancel and the metric contracts the μ' and ν' indices:

$$\begin{aligned}\frac{1}{4}|\mathcal{M}_{qg\to q\gamma}|^2 = \frac{1}{4}e^2Q^2g_s^2\left(c_i^\dagger T^f c_j c_j^\dagger T^f c_i a_f^\dagger a_f\right)\\ \times\Bigg\{(\not{p}_1+m)_{\delta\delta'}\,\gamma^\mu_{\delta'\gamma'}\frac{(\not{q}_2+m)_{\gamma'\beta'}}{q_2^2-m^2}\gamma^\nu_{\beta'\alpha'}(\not{p}_2+m)_{\alpha'\alpha}\,\gamma^\mu_{\alpha\beta}\frac{(\not{q}_1+m)_{\beta\gamma}}{q_1^2-m^2}\gamma^\nu_{\gamma\delta} &\quad (3.16a)\\ +\,(\not{p}_1+m)_{\delta\delta'}\,\gamma^\mu_{\delta'\gamma'}\frac{(\not{q}_2+m)_{\gamma'\beta'}}{q_2^2-m^2}\gamma^\nu_{\beta'\alpha'}(\not{p}_2+m)_{\alpha'\alpha}\,\gamma^\nu_{\alpha\beta}\frac{(\not{q}_2+m)_{\beta\gamma}}{q_2^2-m^2}\gamma^\mu_{\gamma\delta} &\quad (3.16b)\\ +\,(\not{p}_1+m)_{\delta\delta'}\,\gamma^\nu_{\delta'\gamma'}\frac{(\not{q}_1+m)_{\gamma'\beta'}}{q_1^2-m^2}\gamma^\mu_{\beta'\alpha'}(\not{p}_2+m)_{\alpha'\alpha}\,\gamma^\mu_{\alpha\beta}\frac{(\not{q}_1+m)_{\beta\gamma}}{q_1^2-m^2}\gamma^\nu_{\gamma\delta} &\quad (3.16c)\\ +\,(\not{p}_1+m)_{\delta\delta'}\,\gamma^\nu_{\delta'\gamma'}\frac{(\not{q}_1+m)_{\gamma'\beta'}}{q_1^2-m^2}\gamma^\mu_{\beta'\alpha'}(\not{p}_2+m)_{\alpha'\alpha}\,\gamma^\nu_{\alpha\beta}\frac{(\not{q}_2+m)_{\beta\gamma}}{q_2^2-m^2}\gamma^\mu_{\gamma\delta}\Bigg\}. &\quad (3.16d)\end{aligned}$$

Remember, the pre-factor $\frac{1}{4}$ is the result of the spin average of the incoming quark times the polarization average of the incoming gluon.

The first bracket including the tensors in the two color spaces still remain to be calculated. Color creation and annihilation operators $c_{i,j}^\dagger$ and $c_{i,j}$ pick out the (i,j) and (j,i)-th element of the gauge group matrices T^f. Another summation over these two color spaces has to be performed, where the average is now taken over the three (fundamental) colors of the incoming quark and the eight (adjoint) colors of the incoming gluon.

$$\sum_{f=1}^{8}\sum_{i,j=1}^{3} c_i^\dagger T^f c_j c_j^\dagger T^f c_i a_f^\dagger a_f = \sum_{f=1}^{8}\sum_{i,j=1}^{3} T_{ij}^f T_{ji}^f a_f^\dagger a_f = 4 \tag{3.17}$$

Instead of performing the explicit sum using the Gell-Mann matrices, one could alternatively use the so called Fiertz identity for $SU(N)$:

$$T_{ij}^f T_{kl}^f = \frac{1}{2}\left(\delta_{il}\delta_{jk} - \frac{1}{N}\delta_{ij}\delta_{kl}\right), \tag{3.18}$$

or in our special case ($N=3$):

$$T_{ij}^f T_{ji}^f = \frac{1}{2}\left(3\cdot 3 - \frac{1}{3}\cdot 3\right) = 4. \tag{3.19}$$

With the aforementioned average, the pre-factor now reads

$$\begin{aligned}\frac{1}{2\cdot 2\cdot 3\cdot 8}|\mathcal{M}_{qg\to q\gamma}|^2 = \frac{1}{24}e^2Q^2g_s^2\\ \times\{(3.16a)+(3.16b)+(3.16c)+(3.16d)\}.\end{aligned} \tag{3.20}$$

At this point, we make a simplification. We drop the quark masses m, as we are in a regime where the quark momenta in the plasma can be expected to be much larger than their current masses. In this ultra relativistic limit, expression (3.20) can be further simplified by decomposing the slashed momenta via $\not{p} = \gamma^\rho p_\rho$. These momenta p_ρ are no longer objects in spinor space, and can therefore be

pulled out:

$$\begin{aligned}\frac{1}{4}|\mathcal{M}_{qg\to q\gamma}|^2 = \frac{1}{24}e^2Q^2g_s^2 \\ \times\Bigg\{&\frac{p_{1,\lambda}q_{1,\rho}p_{2,\sigma}q_{1,\tau}}{q_2^2q_1^2}\left[\gamma^\lambda_{\delta\delta'}\gamma^\mu_{\delta'\gamma'}\gamma^\rho_{\gamma'\beta'}\gamma^\nu_{\beta'\alpha'}\gamma^\sigma_{\alpha'\alpha}\gamma^\mu_{\alpha\beta}\gamma^\tau_{\beta\gamma}\gamma^\nu_{\gamma\delta}\right] &(3.21a)\\ &+\frac{p_{1,\lambda}q_{2,\rho}p_{2,\sigma}q_{2,\tau}}{q_2^4}\left[\gamma^\lambda_{\delta\delta'}\gamma^\mu_{\delta'\gamma'}\gamma^\rho_{\gamma'\beta'}\gamma^\nu_{\beta'\alpha'}\gamma^\sigma_{\alpha'\alpha}\gamma^\nu_{\alpha\beta}\gamma^\tau_{\beta\gamma}\gamma^\mu_{\gamma\delta}\right] &(3.21b)\\ &+\frac{p_{1,\lambda}q_{1,\rho}p_{2,\sigma}q_{1,\tau}}{q_1^4}\left[\gamma^\lambda_{\delta\delta'}\gamma^\nu_{\delta'\gamma'}\gamma^\rho_{\gamma'\beta'}\gamma^\mu_{\beta'\alpha'}\gamma^\sigma_{\alpha'\alpha}\gamma^\mu_{\alpha\beta}\gamma^\tau_{\beta\gamma}\gamma^\nu_{\gamma\delta}\right] &(3.21c)\\ &+\frac{p_{1,\lambda}q_{1,\rho}p_{2,\sigma}q_{2,\tau}}{q_1^2q_2^2}\left[\gamma^\lambda_{\delta\delta'}\gamma^\nu_{\delta'\gamma'}\gamma^\rho_{\gamma'\beta'}\gamma^\mu_{\beta'\alpha'}\gamma^\sigma_{\alpha'\alpha}\gamma^\nu_{\alpha\beta}\gamma^\tau_{\beta\gamma}\gamma^\mu_{\gamma\delta}\right]\Bigg\}. &(3.21d)\end{aligned}$$

These four lines are hence traces over spinor space. To calculate these traces, one can again make use of properties of the Dirac matrices:

$$\begin{aligned}\mathrm{Tr}[\gamma^\mu\gamma^\nu] &= 4g^{\mu\nu},\\ \mathrm{Tr}[\gamma^\mu\gamma^\nu\gamma^\rho\gamma^\sigma] &= 4(g^{\mu\nu}g^{\rho\sigma} - g^{\mu\rho}g^{\nu\sigma} + g^{\mu\sigma}g^{\nu\rho}).\end{aligned} \tag{3.22}$$

The trace of an odd number of Dirac matrices vanishes, and higher even-numbered traces can be evaluated via recursive formulae, special techniques (e.g. [66]) or using a computer algebra system [67].

It is quite evident that these computations are a tedious task. The trace over 8 gamma matrices already consists of 105 terms, when fully expanded. Luckily, this task can be efficiently outsourced to computer algebra systems. Performing these calculations yield the following expression:

$$\frac{1}{96}|\mathcal{M}_{qg\to q\gamma}|^2 = \frac{1}{24}e^2Q^2g_s^2\left\{\frac{32\;p\cdot p_1\;p\cdot p_2}{q_1^4} + \frac{32\;p\cdot p_1\;p\cdot p_2}{q_2^4}\right\}. \tag{3.23}$$

Eq. (3.23) can now be further simplified by using the momentum conservation condition at each vertex in Fig. 3.2:

$$\begin{aligned}q_1 = p + p_2 &\to q_1^2 = 2p\cdot p_2,\\ q_2 = p_1 - p &\to q_2^2 = -2p\cdot p_1,\end{aligned} \tag{3.24}$$

where the massless limit of the relation $p_i^2 = m^2 = 0$ was used.

$$\frac{1}{96}|\mathcal{M}_{qg\to q\gamma}|^2 = \frac{1}{3}e^2Q^2g_s^2\left\{\frac{p\cdot p_1}{p\cdot p_2} + \frac{p\cdot p_2}{p\cdot p_1}\right\}. \tag{3.25}$$

3.2.2. Antiquark Compton scattering

The calculation of the antiquark Compton scattering contribution is very similar to the Compton scattering one. One has to replace the quark spinors u and $\bar{u}$ in Eq. (3.1) by antiquark spinors $\bar{v}$ and v respectively, as well as replace the fermionic propagators, since the momentum flow now points into the opposite direction (see Feynman rules in Appendix A).

Instead of using the spinor sum for quark spinors (3.3), we have to apply the antiquark pendant

$$\sum_s v^s_\delta(p_1)\bar{v}^s_{\delta'}(p_1) = (\not{p}_1 - m)_{\delta\delta'}. \tag{3.26}$$

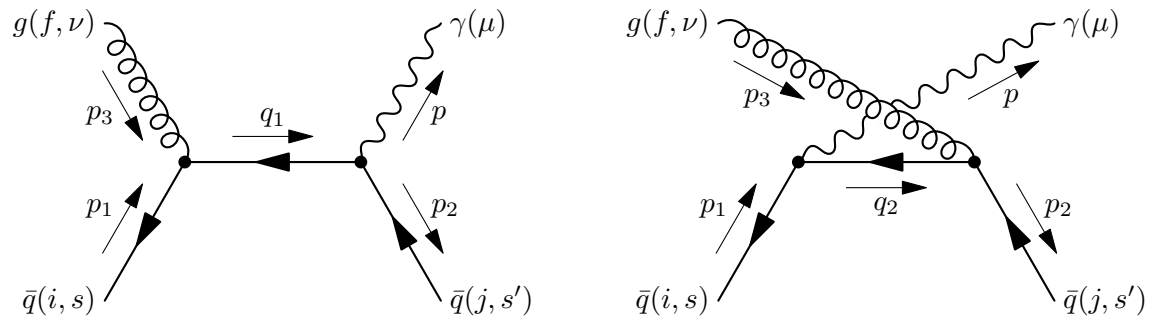

s-channel (t,u)-channel

Figure 3.3: The detailed Compton-scattering diagram ($\bar{q}g \to \bar{q}\gamma$, Fig. 3.1b) for antiquarks, using the same notation as in Fig. 3.2.

Performing the calculation gives us the same result as the quark Compton scattering process.

3.2.3. Quark-antiquark annihilation

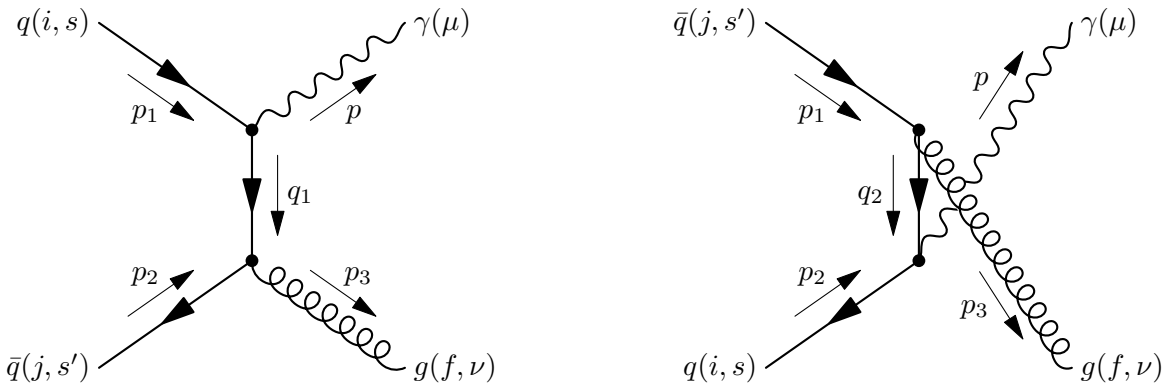

u-channel t-channel

Figure 3.4: Detailed quark-antiquark annihilation process.

A closer look at the detailed Feynman graphs in both Fig. 3.4 and Fig. 3.2 reveals important similarities. By exchanging $p_3 \to -p_3$ and $p_2 \to -p_2$ in the s-channel diagram in Fig. 3.4, and turning the antiquark spinor $\bar{q}$ into a quark spinor q, one arrives at the quark Compton scattering diagram. To account for the exchanged antiquark spinor, one has to write an additional overall minus sign. While incorporating the degeneracies for the different incoming and outgoing particle states, the result can be written down by performing the aforementioned exchanges on Eq. (3.25):

$$\frac{1}{36}|\mathcal{M}_{q\bar{q}\to g\gamma}|^2 = \frac{8}{9}e^2Q^2g_s^2\left\{\frac{p\cdot p_1}{p\cdot p_2}+\frac{p\cdot p_2}{p\cdot p_1}\right\}. \tag{3.27}$$

The averaging factor of $\frac{1}{36}$ is composed of the two incoming colors (3) and incoming spins (2) for the quark and antiquark each ($2\cdot 3\cdot 2\cdot 3 = 36$), the factor of $\frac{8}{9}$ is attained by taking the factor of $\frac{1}{3}$ from the Compton result and dividing by the quark colors (which we lose as outgoing states) and multiplying by the gluon colors (which we gain): $\frac{1}{3}\cdot\frac{1}{3}\cdot 8 = \frac{8}{9}$.

Aside from the pre-factor, the result for the annihilation diagram is the same as for the Compton scattering diagrams. Note that this is a special case in the ultra relativistic limit and does not hold for finite quark masses.

3.3. Soft contribution

One can already see from the expressions (3.25) and (3.27), the hard contributions feature a logarithmic divergence. It is therefore necessary to calculate the remaining low-energy processes that were omitted in the hard part. The photon production rate for unpolarized photons to leading order in α and all orders in α_s can be calculated via [68]

$$E\frac{dR_{\text{soft}}}{d^3q} = -\frac{1}{(2\pi)^3} g_{\mu\nu}\ \text{Im}\ \Pi_{\text{R}}^{\mu\nu}(q). \tag{3.28}$$

Π_{R} is the retarded photon polarization tensor, which in first loop order is represented by the Feynman diagram in Fig. 3.5. By simple power-counting of the loop integral, one can see that this graph

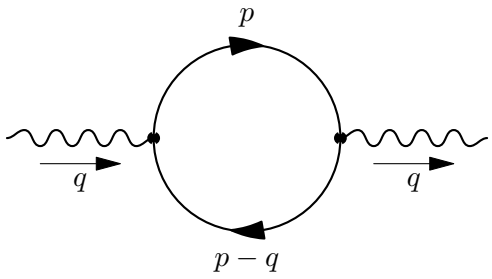

Figure 3.5: Photon polarization diagram with bare internal propagators.

exhibits an ultraviolet divergence. Nevertheless, we need to calculate the photon rate (3.28), and hence the imaginary part of the polarization tensor. This imaginary part of Π_R is logarithmically infrared divergent - like our hard contribution.

To combat this divergence, one can make use of the *hard thermal loop* (HTL) resummation technique by E. Braaten and R.D. Pisarski [58]. M.E. Carrington, H. Defu and M.H. Thoma extended this technique to the real-time formalism [69], developed by L.V. Keldysh [70]. The hard thermal loop approximation refers to the fact that the soft external photon momenta $q \sim gT$ are much smaller than the internal momenta $p \sim T$.

The motivation to use a non-equilibrium formalism in order to compute the soft photon rates is essentially the lack of knowledge about the evolution of the QGP itself. It is not yet clear, whether the plasma reaches thermal equilibrium at all in its short lifetime.

Thorough details on the real time formalism (RTF) can be found in e.g. [71]. For an essential understanding of the calculations done in Refs. [28, 60, 61], the following points should be sufficient:

- the vertices in Fig. 3.5 are now distinguished between incoming (1) and outgoing photon (2),
- propagators are distinguished in a similar manner, as they connect different vertices with different start- and endpoints.

The logarithmic infrared divergence in Fig. 3.5 is eliminated if we replace a bare internal propagator by an effective or dressed one. This way, the previously massless fermionic propagators acquire a

thermal mass, which shields off the divergence. According to the RTF rules, we need to replace both the upper and the lower internal propagator, one at a time. Each blob in Fig. 3.6 represents an HTL

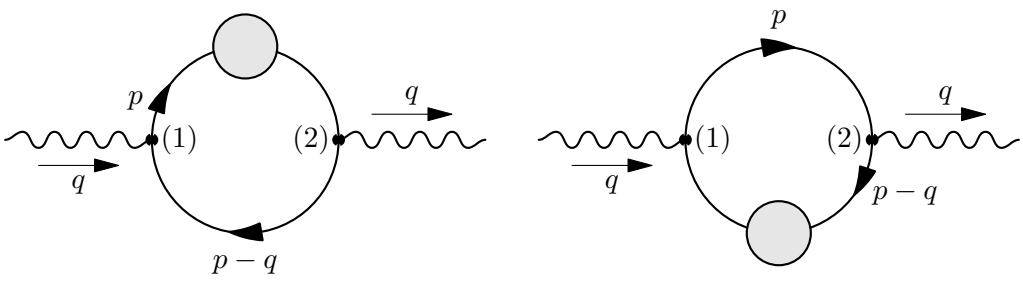

Figure 3.6: Photon polarization diagram with HTL resummed fermion propagators. The grey blob represent the dressing of a fermion propagator with quark self energies according to Fig. 3.7.

resummed propagator with quark self-energy insertions (Fig. 3.7). In the anisotropic case, we need to require that $p \gg q$ holds for each component of the momenta [72]. The photon production rate is

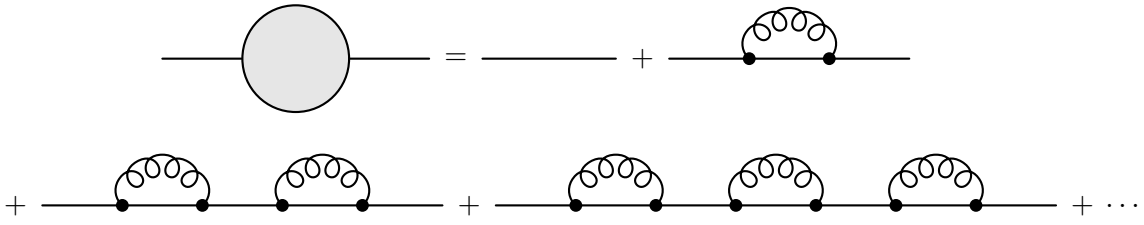

Figure 3.7: Quark self-energy insertions.

written as the trace of the (12)-component of the photon polarization tensor [73]:

$$E\frac{dR_{\text{soft}}}{d^3q} = \frac{i}{2(2\pi)^3} g_{\mu\nu}\Pi^{\mu\nu}_{(12)}(q). \tag{3.29}$$

The Feynman graphs (Fig. 3.6) have to be evaluated using the special rules for the real-time formalism. We need to differentiate between vertex (1) and vertex (2), as well as propagators S_{12} and S_{21}, where the order of the numbers indicates the direction of the momentum arrow.

$$\begin{aligned} -i\Pi^{\mu\nu}_{(12)}(q) = -e^2Q^2N_c \int \frac{d^4p}{(2\pi)^4} \mathrm{Tr}\,[&\gamma^\mu i S^\star_{12}(p)\gamma^\nu i S_{21}(p-q) \\ &+\gamma^\mu i S_{12}(p)\gamma^\nu i S^\star_{21}(p-q)] \end{aligned} \tag{3.30}$$

The star on a propagator ($S^\star$) indicates that this is a dressed propagator - dressed with gluon self-energy insertions (Fig. 3.7). To compute the polarization tensor, expressions for the (12) and (21) components of the dressed fermionic propagators $S^\star$ have to be found.

Using a similar notation as Refs. [69, 74], the fermionic bare propagator is

$$\begin{aligned} S(k) = (\not{k} + m)\Bigg\{ &\begin{pmatrix} (k^2 - m^2 + i\varepsilon)^{-1} & 0 \\ 0 & -(k^2 - m^2 - i\varepsilon)^{-1} \end{pmatrix} \\ &+ 2\pi i\, \delta(k^2 - m^2) \begin{pmatrix} f_F(\mathbf{k}) & f_F(\mathbf{k}) - \theta(-k^{(0)}) \\ f_F(\mathbf{k}) - \theta(k^{(0)}) & f_F(\mathbf{k}) \end{pmatrix} \Bigg\}. \end{aligned} \tag{3.31}$$

The fermionic distribution function f_F can be either an equilibrium or non-equilibrium distribution, as well as isotropic or anisotropic.

The 2x2 structure of the propagators need to be taken into account when writing down the Dyson-Schwinger equation

$$S^\star = S + S\Sigma S^\star, \tag{3.32}$$

with Σ being the fermion self energy. We have for the (ab)-components

$$S^\star_{ab} = S_{ab} + \sum_{i,j=1}^{2} S_{ai}\Sigma_{ij}S^\star_{jb}. \tag{3.33}$$

Writing down (3.33) for $a = b = 1$, $a = b = 2$ and taking the sum of the two resulting equations, we get

$$S^\star_{11} + S^\star_{22} = S_{11} + S_{22} + \sum_{i,j=1}^{2} S_{1i}\Sigma_{ij}S^\star_{j1} + \sum_{i,j=1}^{2} S_{2i}\Sigma_{ij}S^\star_{j2}. \tag{3.34}$$

Including the two expanded sums, the right hand side now consists of 10 terms. As there are only three independent linear combinations of the components [75]

$$\begin{aligned} S_R &= S_{11} - S_{12}, \\ S_A &= S_{11} - S_{21}, \\ S_F &= S_{11} + S_{22}. \end{aligned} \tag{3.35}$$

(3.34) can be rewritten using the shorthand notation in (3.35). Additionally, one can explicitly show that

$$S_{11} - S_{12} - S_{21} + S_{22} = 0. \tag{3.36}$$

First, we write down the components

$$\begin{aligned} &[S_{11}(k) + S_{22}(k) - S_{12}(k) - S_{21}(k)](\not{k} + m)^{-1} = \\ &\quad = \frac{1}{k^2 - m^2 + i\varepsilon} + \cancel{2\pi i\delta(k^2 - m^2)f_F(\mathbf{k})} \\ &\quad - \frac{1}{k^2 - m^2 - i\varepsilon} + \cancel{2\pi i\delta(k^2 - m^2)f_F(\mathbf{k})} \\ &\quad - 2\pi i\delta(k^2 - m^2)[\cancel{f_F(\mathbf{k})} - \theta(-k^{(0)})] \\ &\quad - 2\pi i\delta(k^2 - m^2)[\cancel{f_F(\mathbf{k})} - \theta(k^{(0)})] \\ &\quad = \frac{1}{k^2 - m^2 + i\varepsilon} - \frac{1}{k^2 - m^2 - i\varepsilon} + 2\pi i\delta(k^2 - m^2)\underbrace{[\theta(k^{(0)}) + \theta(-k^{(0)})]}_{=1}. \end{aligned} \tag{3.37}$$

Next, we make use of the Sokhatsky–Weierstrass theorem, which allows us to rewrite the two fractions according to the sign of the infinitesimal shift in the complex plane by ε:

$$\begin{aligned} \frac{1}{k^2 - m^2 + i\varepsilon} &= \mathcal{P}\frac{1}{k^2 - m^2} - i\pi\delta(k^2 - m^2), \\ \frac{1}{k^2 - m^2 - i\varepsilon} &= \mathcal{P}\frac{1}{k^2 - m^2} + i\pi\delta(k^2 - m^2), \end{aligned} \tag{3.38}$$

and thus (3.36) is shown. Because of relation (3.36), the three independent linear combinations (3.35)

can also be written as two different sums of propagator components each:

$$\begin{aligned} S_R &= S_{11} - S_{12} = S_{21} - S_{22}, \\ S_A &= S_{11} - S_{21} = S_{12} - S_{22}, \\ S_F &= S_{11} + S_{22} = S_{12} + S_{21}. \end{aligned} \tag{3.39}$$

Similar relations hold for the components of the self-energy Σ:

$$\begin{aligned} \Sigma_{11} + \Sigma_{12} + \Sigma_{21} + \Sigma_{22} &= 0, \\ \Sigma_R = \Sigma_{11} + \Sigma_{12} &= -\Sigma_{21} - \Sigma_{22}, \\ \Sigma_A = \Sigma_{11} + \Sigma_{21} &= -\Sigma_{12} - \Sigma_{22}, \\ \Sigma_F = \Sigma_{11} + \Sigma_{22} &= -\Sigma_{12} - \Sigma_{21}. \end{aligned} \tag{3.40}$$

The subscripts of the three independent linear combinations in (3.39) reflect the property of that propagator. If one explicitly calculates e.g. S_R, one gets

$$\begin{aligned} S_R(k) = S_{11}(k) - S_{12}(k) &= (\not{k} + m)[-\mathrm{sgn}(k^{(0)}) i\pi\delta(k^2 - m^2)] \\ &= \frac{\not{k} + m}{k^2 - m^2 + i\varepsilon \mathrm{sgn}(k^{(0)})}, \end{aligned} \tag{3.41}$$

which is the well known retarded fermion propagator, with the contour bypassing the poles at $k^2 = m^2$ in the upper half of the complex plane, depicted in Fig. 3.8. S_A is the advanced propagator, while S_F is the symmetric one, employing the Feynman prescription.

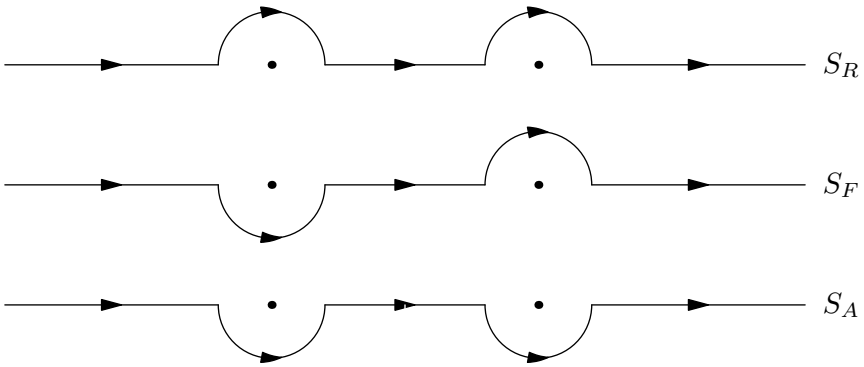

Figure 3.8: Integration contours for the retarded (S_R), symmetric (S_F) and advanced (S_A) propagators. The dots represent the poles on the real axis at $k = \pm m$.

The relations (3.39) and (3.40) can be used to find expressions for the (ab)-components of both S and Σ:

$$\begin{aligned} S_{11} &= \frac{1}{2}(S_F + S_A + S_R), \\ S_{12} &= \frac{1}{2}(S_F + S_A - S_R), \\ S_{21} &= \frac{1}{2}(S_F - S_A + S_R), \\ S_{22} &= \frac{1}{2}(S_F - S_A - S_R), \end{aligned} \tag{3.42}$$

$$\begin{aligned}\Sigma_{11} &= \frac{1}{2}(+\Sigma_F + \Sigma_A + \Sigma_R),\\ \Sigma_{12} &= \frac{1}{2}(-\Sigma_F - \Sigma_A - \Sigma_R),\\ \Sigma_{21} &= \frac{1}{2}(-\Sigma_F + \Sigma_A - \Sigma_R),\\ \Sigma_{22} &= \frac{1}{2}(+\Sigma_F - \Sigma_A - \Sigma_R).\end{aligned} \tag{3.43}$$

Note that the relations (3.42) also hold for the dressed propagator $S^\star$. Inserting the expressions (3.42) and (3.43) into Eq. (3.34) yields the following, more legible result:

$$S_F^\star = S_F + S_R\Sigma_R S_F^\star + S_F\Sigma_A S_A^\star + S_R\Sigma_R S_A^\star. \tag{3.44}$$

The general ansatz to solve this equation is [69]

$$\begin{aligned}S_F^\star(k) = [1 - 2f_F(\mathbf{k})]\mathrm{sgn}(k^{(0)})[S_R^\star(k) - S_A^\star(k)]\\ + S_R^\star(k)\left\{\Sigma_F(k) - [1 - 2f_F(\mathbf{k})]\mathrm{sgn}(k^{(0)})[\Sigma_R(k) - \Sigma_A(k)]\right\} S_A^\star(k).\end{aligned} \tag{3.45}$$

As shown in [76], the Kubo-Martin-Schwinger formula,

$$\Sigma_{12} = -\Sigma_{21}, \tag{3.46}$$

also holds for non-equilibrium systems. Σ_F is therefore exactly zero and the difference $\Sigma_R - \Sigma_A$ is equal to $2\Sigma_{12}$. The ansatz (3.45) therefore reduces to

$$\begin{aligned}S_F^\star(k) = [1 - 2f_F(\mathbf{k})]\mathrm{sgn}(k^{(0)})[S_R^\star(k) - S_A^\star(k)]\\ - S_R^\star(k)\left\{[1 - 2f_F(\mathbf{k})]\mathrm{sgn}(k^{(0)})[2\Sigma_{12}(k)]\right\} S_A^\star(k).\end{aligned} \tag{3.47}$$

Since the relations in Eq. (3.42) also hold for dressed propagators, we write for $S_{12}^\star$

$$S_{12}^\star = \frac{1}{2}(S_F^\star + S_A^\star - S_R^\star), \tag{3.48}$$

and insert the result for $S_F^\star$ from Eq. (3.47):

$$\begin{aligned}S_{12}^\star(k) = \frac{1}{2}\left\{[S_R^\star(k) - S_A^\star(k)]\mathrm{sgn}(k^{(0)}) -\right.\\ \left.\mathrm{sgn}(k^{(0)})S_R^\star(k)\, 2\,\Sigma_{12}(k)\, S_A^\star(k) + S_A^\star(k) - S_R(k)^\star\right\}.\end{aligned} \tag{3.49}$$

The Dyson-Schwinger equation (3.32) can be rewritten if we multiply by $S^{-1}(\ldots)[S^\star]^{-1}$ as

$$S^{-1} = [S^\star]^{-1} + \Sigma, \tag{3.50}$$

so that

$$\begin{aligned}S_A^{-1} &= [S_A^\star]^{-1} + \Sigma_A,\\ S_R^{-1} &= [S_R^\star]^{-1} + \Sigma_R,\\ S_A^{-1} - S_R^{-1} &= [S_A^\star]^{-1} - [S_R^\star]^{-1} + \underbrace{\Sigma_A - \Sigma_R}_{=-2\Sigma_{12}}.\end{aligned} \tag{3.51}$$

The difference of the inverse propagators $S_A^{-1} - S_R^{-1}$ is zero, giving us an expression for $2\Sigma_{12}$:

$$2\Sigma_{12} = [S_A^\star]^{-1} - [S_R^\star]^{-1}, \tag{3.52}$$

which can be inserted into Eq. (3.49). The inverse dressed propagators yield terms that exactly cancel out the first term in Eq. (3.49), giving us the result for $S_{12}^\star$:

$$S_{12}^\star = \frac{1}{2}(S_A^\star - S_R^\star). \tag{3.53}$$

Performing a similar calculation for $S_{21}^\star$ yields

$$S_{21}^\star = \frac{1}{2}(S_R^\star - S_A^\star) = -S_{12}^\star. \tag{3.54}$$

We now have expressions for both the (12) and (21) components of the dressed propagator $S^\star$ and can compute the trace of the photon polarization tensor (3.30). To simplify the expression, we shift the momentum p in the second term $p \to p + q$:

$$\begin{aligned} -ig_{\mu\nu}\Pi_{(12)}^{\mu\nu}(q) = -e^2Q^2N_c g_{\mu\nu} \int \frac{d^4p}{(2\pi)^4} \mathrm{Tr}\,[&\gamma^\mu i S_{12}^\star(p)\gamma^\nu i S_{21}(p-q) \\ &+\gamma^\mu i S_{12}(p+q)\gamma^\nu i S_{21}^\star(p)]\,. \end{aligned} \tag{3.55}$$

It should be noted here that the propagators still have a Dirac structure with suppressed spinor indices. Consequently, the correct order of the gamma matrices and the propagators should always be ensured. In the regime of the quark-gluon plasma, we can use massless propagators, eliminating the mass terms in Eq. (3.31). The (12) and (21) components explicitly read:

$$S_{12/21}(k) = \not{k}\, 2\pi i\delta(k^2)[f_F(\mathbf{k}) - \Theta(\mp k^{(0)})]. \tag{3.56}$$

Now we can apply the aforementioned hard thermal loop approximation, since we encounter sums (differences) of hard (q) and soft (p) momenta:

$$\begin{aligned} p \pm q &\approx \pm q + O(gT), \\ (p \pm q)^2 = p^2 + q^2 \pm 2p\cdot q &\approx \pm 2p\cdot q + O(g^2T^2). \end{aligned} \tag{3.57}$$

This gives us following expression for the (12) and (21) components:

$$\begin{aligned} S_{12/21}(p \pm q) &= (\not{p} \pm \not{q})2\pi i\delta([p\pm q]^2)[f_F(\mathbf{q}) - \Theta(\mp[p^{(0)} \pm q^{(0)}]) \\ &= \pm\not{q}\pi i \frac{1}{q^{(0)}}\delta(p^{(0)} - \mathbf{p}\cdot\hat{\mathbf{q}})[f_F(\mathbf{q}) - \Theta(-q^{(0)})] \\ &= \pm\frac{\not{q}\pi i}{q^{(0)}}\, f_F(\mathbf{q})\delta(p^{(0)} - \mathbf{p}\cdot\hat{\mathbf{q}}). \end{aligned} \tag{3.58}$$

The theta function in the upper equation is zero, since $q^{(0)}$ is the zeroth component of the photon momentum, and as such always positive: $q^{(0)} = |\mathbf{q}|$. This form of the propagator also clearly shows us the spinor structure with the slashed photon momentum q. As we want to make use of Dirac trace theorems again, it is helpful to decompose the propagators as follows:

$$\begin{aligned} S_{12/21} &= \gamma^\alpha (S_{12/21})_\alpha, \\ S_{12/21}^\star &= \gamma^\alpha (S_{12/21}^\star)_\alpha. \end{aligned} \tag{3.59}$$

Inserting the explicit form of the bare propagators into Eq. (3.55) and writing out $d^4p = d^3p\, dp^{(0)}$ as well as $\not{q} = \gamma^\alpha q_\alpha$ leaves us with

$$\begin{aligned} -ig_{\mu\nu}\Pi^{\mu\nu}_{(12)}(q) &= \\ = e^2Q^2N_c g_{\mu\nu}\int \frac{d^3p\, dp^{(0)}}{(2\pi)^4}\mathrm{Tr}\Big[&\gamma^\mu\gamma^\alpha\gamma^\nu q_\alpha \frac{\pi\, i}{q^{(0)}} f_F(\mathbf{q})\,\delta(p^{(0)}-\mathbf{p}\cdot\hat{\mathbf{q}})S^\star_{21}(p) \\ &-\gamma^\mu S^\star_{12}(p)\gamma^\nu\gamma^\alpha q_\alpha \frac{\pi\, i}{q^{(0)}} f_F(\mathbf{q})\,\delta(p^{(0)}-\mathbf{p}\cdot\hat{\mathbf{q}})\Big]. \end{aligned} \tag{3.60}$$

Making use of Eq. (3.54) allows us to compactify the sum ($S^\star_{12} = -S^\star_{21}$) and we can perform the $p^{(0)}$ integration, keeping in mind that we need to impose the condition $p^{(0)} = \mathbf{p}\cdot\hat{\mathbf{q}}$ in the succeeding steps of the calculation:

$$\begin{aligned} -ig_{\mu\nu}\Pi^{\mu\nu}_{(12)}(q) &= \\ &- e^2Q^2N_c g_{\mu\nu}\int \frac{d^3p}{(2\pi)^3\cdot 2}\mathrm{Tr}\left[\gamma^\mu\gamma^\alpha\gamma^\nu\gamma^\beta + \gamma^\mu\gamma^\beta\gamma^\nu\gamma^\alpha\right] \\ &\times q_\alpha[S^\star_{12}(q)]_\beta \frac{i}{q^{(0)}} f_F(\mathbf{q})\Big|_{p^{(0)}=\mathbf{p}\cdot\hat{\mathbf{q}}}. \end{aligned} \tag{3.61}$$

The dressed propagator can now be decomposed via Eq. (3.53) ($-S^\star_{12} = \frac{1}{2}[S^\star_R - S^\star_A]$) and the two Dirac traces compute to $-8g^{\alpha\beta}$ when contracted with the metric tensor $g_{\mu\nu}$:

$$-ig_{\mu\nu}\Pi^{\mu\nu}_{(12)}(q) = -e^2Q^2N_c\frac{1}{q^{(0)}}f_F(\mathbf{q})\int\frac{d^3p}{(2\pi)^3}4g^{\alpha\beta}q_\alpha\left\{i[S^\star_R(p)]_\beta - i[S^\star_A(p)]_\beta\right\}\Big|_{p^{(0)}=\mathbf{p}\cdot\hat{\mathbf{q}}}. \tag{3.62}$$

The HTL resummed retarded and advanced propagators are given by

$$S^\star_{R,A}(k) = \frac{1}{\not{k} - \Sigma_{R,A}}, \tag{3.63}$$

with the retarded and advanced electron self-energies [72, 76]

$$\Sigma_{R,A}(k) = \frac{g^2C_F}{4}\int\frac{d^3p}{(2\pi)^3}\frac{f(\mathbf{p})}{|\mathbf{p}|}\frac{p\cdot\gamma}{p\cdot k \pm i\varepsilon}, \tag{3.64}$$

where C_F is the Casimir factor for N_c colors

$$C_F \equiv \frac{N_c^2-1}{2N_c}. \tag{3.65}$$

Using both Eq. (3.63) and Eq. (3.64), one can see that the retarded and advanced dressed propagators are related by complex conjugation:

$$iS^\star_R - iS^\star_A = iS^\star_R - [iS^\star_R]^* = -2\mathrm{Im}S^\star_R. \tag{3.66}$$

This allows to rewrite Eq. (3.62) and leaving us with a nice, compact result [60]:

$$-ig_{\mu\nu}\Pi^{\mu\nu}_{(12)} = e^2Q^2N_c\frac{8f_F(\mathbf{q})}{|\mathbf{q}|}\int\frac{d^3p}{(2\pi)^3}\mathrm{Im}[q\cdot S^\star_R(p)]\Big|_{p^{(0)}=\mathbf{p}\cdot\hat{\mathbf{q}}}. \tag{3.67}$$

3.4. Numerical integration

The total photon production rate EdR/d^3p is obtained by computing the phase space integral of the scattering amplitudes and performing the integration in Eq. (3.67). To calculate the production rates for the hard processes, we start with the Compton portion:

$$E\frac{dR_{\rm com}}{d^3p} = \frac{\mathcal{N}_{\rm com}}{2(2\pi)^3}\int \frac{d^3p_1\, f_q(\mathbf{p}_1)}{2E_1(2\pi)^3}\frac{d^3p_2\,[1-f_q(\mathbf{p}_2)]}{2E_2(2\pi)^3}\frac{d^3p_3\, f_g(\mathbf{p_3})}{2E_3(2\pi)^3} \times (2\pi)^4\delta^{(4)}(p_1+p_3-p_2-p)|\mathcal{M}_{\rm com}|^2. \tag{3.68}$$

The degeneracy factor $\mathcal{N}_{\rm com}$ contains the degrees of freedom of the incoming (anti)quarks and gluons, some of which we already noted in Section 3.2.1. First, we pull the pre-factor $\frac{1}{96}$ from (3.25) to the right side and take the quark charges Q out of $|\mathcal{M}_{\rm com}|^2$. What remains to be considered is the antiquark contribution (Section 3.2.3), which amounts to a factor of 2 due to the result being the same as in the quark Compton case. We consider only up and down quarks with quark charges $-\frac{1}{3}$ and $\frac{2}{3}$ respectively. This results in a factor of $\frac{5}{9}$:

$$\mathcal{N}_{\rm com} = 2\cdot\frac{5}{9} = \frac{10}{9}. \tag{3.69}$$

The result is consistent with both [62] and [61] if one considers $e^2\, g_s^2 = 16\pi^2\alpha\alpha_s$ and the way how the degeneracy factors are split up between $|\mathcal{M}_{\rm com}|^2$ and $\mathcal{N}_{\rm com}$. We introduce a new variable $q = p_1 - p$, the four dimensional delta function is then

$$\delta^{(4)}(q+p_3-p_2) = \delta^{(3)}(\mathbf{p_3}+\mathbf{q}-\mathbf{p_2})\delta(p_3^{(0)}+q^{(0)}-p_2^{(0)}). \tag{3.70}$$

The three dimensional part of the delta function is used to integrate the momentum $\mathbf{p_3}$ in a trivial fashion:

$$E\frac{dR_{\rm com}}{d^3p} = \frac{\mathcal{N}_{\rm com}}{2(2\pi)^3}\int d^3q\, d^3p_2\, \frac{f_q(\mathbf{p}+\mathbf{q})}{2E_1(2\pi)^3}\frac{[1-f_q(\mathbf{p}_2)]}{2E_2(2\pi)^3}\frac{f_g(\mathbf{q}-\mathbf{p}_2)}{2E_3(2\pi)^3} \times (2\pi)^4\delta(p_3^{(0)}+q^{(0)}-p_2^{(0)})|\mathcal{M}_{\rm com}|^2. \tag{3.71}$$

In the next step, we rename $p_2 \to k$, and rewrite (3.71) in terms of our new variables (using $p\cdot p_1 = -\frac{q^2}{2}$):

$$E\frac{dR_{\rm com}}{d^3p} = -\frac{5\alpha\alpha_s}{36\pi^6}\int d^3q\, d^3k\, \frac{f_q(\mathbf{p}+\mathbf{q})}{|\mathbf{p}+\mathbf{q}|}\frac{[1-f_q(\mathbf{k})]}{|\mathbf{k}|}\frac{f_g(\mathbf{q}-\mathbf{k})}{|\mathbf{q}-\mathbf{k}|} \times \delta(p_3^{(0)}+q^{(0)}-p_2^{(0)})\left\{\frac{q^2}{2p\cdot k}+\frac{2p\cdot k}{q^2}\right\}. \tag{3.72}$$

In order to evaluate the remaining delta function, it is convenient to switch to spherical coordinates:

$$\zeta = |\zeta|\begin{pmatrix}\cos\phi_\zeta\sin\theta_\zeta\\ \sin\phi_\zeta\sin\theta_\zeta\\ \cos\theta_\zeta\end{pmatrix}, \tag{3.73}$$

with ζ being k, p or q. Further, we set $q^{(0)} \to \omega$ to be consistent with [61, 62]:

$$\delta(p_3^{(0)}+q^{(0)}-p_2^{(0)}) = \delta(|\mathbf{k}-\mathbf{q}|+\omega-|\mathbf{k}|). \tag{3.74}$$

Using the parametrization we chose in (3.73), the first term in the delta function computes to

$$|\mathbf{k}-\mathbf{q}| = \left(|\mathbf{k}|^2+|\mathbf{q}|^2-2|\mathbf{k}||\mathbf{q}|[\cos\theta_k\cos\theta_q+\cos(\phi_k-\phi_q)\sin\theta_k\sin\theta_q]\right)^{\frac{1}{2}}. \tag{3.75}$$

Following [61], we want to use this delta function to integrate the azimuthal angle ϕ_k. Isolating ϕ_k requires us to square the equation $|\mathbf{k}-\mathbf{q}| = |\mathbf{k}|-\omega$ in the delta function from Eq. (3.74):

$$(|\mathbf{k}-\mathbf{q}|)^2 = |\mathbf{k}|^2+\omega^2-2|\mathbf{k}|\omega. \tag{3.76}$$

This allows for an easy extraction of the cosine term, when inserting Eq. (3.75) into Eq. (3.76):

$$\cos(\phi_k-\phi_q) = \frac{2|\mathbf{k}|(\omega+|\mathbf{q}|\cos\theta_k\cos\theta_q)-\omega^2-|\mathbf{q}|^2}{2|\mathbf{k}||\mathbf{q}|\sin\theta_k\sin\theta_q} \equiv \kappa. \tag{3.77}$$

The equation has two solutions for ϕ_k:

$$\phi_k = \phi_q \pm \arccos\kappa. \tag{3.78}$$

If we extract ϕ_k using the delta function, we need to sum over the two roots $\phi_{k,i}$

$$\delta(g(\phi_k)) = \sum_i \frac{\delta(\phi_k-\phi_{k,i})}{|g'(\phi_{k,i})|} \tag{3.79}$$

with

$$g(\phi_k) = |\mathbf{k}-\mathbf{q}|+\omega-|\mathbf{k}|. \tag{3.80}$$

Since $|\mathbf{k}-\mathbf{q}|$ is a square root, we will use a mixed notation in this case. The derivative of $g(\phi_k)$ at both roots is

$$|g(\phi_{k,i})| = \left|\frac{1}{2}\frac{1}{|\mathbf{k}-\mathbf{q}|}2|\mathbf{k}||\mathbf{q}|\sin\theta_k\sin\theta_q\sin(\arccos\kappa)\right|. \tag{3.81}$$

Rewriting this with $\sin(\arccos\kappa) = \sqrt{1-\kappa^2}$ leads to

$$\delta(|\mathbf{k}-\mathbf{q}|+\omega-|\mathbf{k}|) \to 2|\mathbf{k}-\mathbf{q}|\sum_i \chi^{-\frac{1}{2}}\Theta(\chi)\delta(\phi_k-\phi_{k,i}), \tag{3.82}$$

with

$$\chi \equiv 4|\mathbf{k}|^2|\mathbf{q}|^2\sin^2\theta_k\sin^2\theta_q - [2|\mathbf{k}|(\omega+|\mathbf{q}|\cos\theta_k\cos\theta_q)-\omega^2-|\mathbf{q}|^2]^2. \tag{3.83}$$

Putting it all together and expanding the integral measures into spherical coordinates $d^3\zeta = \zeta^2\sin\theta_\zeta d\zeta d\theta_\zeta d\phi_\zeta$ for $\zeta = \mathbf{q},\mathbf{k}$ gives us (the ϕ_k integration has been performed using the delta function above):

$$\begin{aligned} E\frac{dR_{\text{com}}}{d^3p} = &-\frac{5\alpha\alpha_s}{18\pi^6}\sum_i\int_{q^*}^{\infty}\mathbf{q}^2 d|\mathbf{q}|\int_0^{\pi}\sin\theta_q d\theta_q\int_0^{2\pi}d\phi_q\int_0^{\infty}|\mathbf{k}|d|\mathbf{k}|\int_0^{\pi}\sin\theta_k d\theta_k \\ &\times\frac{f_q(\mathbf{p}+\mathbf{q})}{|\mathbf{p}+\mathbf{q}|}[1-f_q(\mathbf{k})]f_g(\mathbf{q}-\mathbf{k})\chi^{-\frac{1}{2}}\Theta(\chi)\left\{\frac{q^2}{2p\cdot k}+\frac{2p\cdot k}{q^2}\right\}\Bigg|_{\phi_k=\phi_{k,i}}. \end{aligned} \tag{3.84}$$

One can clearly see that we will encounter a logarithmic divergence for $q^*\to 0$, due to the term in the scattering matrix. As can be shown by analytically extracting the leading divergence for the isotropic case [62], the infrared cut-off q^* can be chosen to be around the same scale as the ultraviolet cut-off for the soft part. This turns q^* essentially into a hard-soft separation scale. When chosen right, small changes to this separation scale should not alter the computed photon rate noticeably. For the

computation, q^* has been set to

$$q^* \equiv \sqrt{g}\, T = T(4\pi\alpha)^{\frac{1}{4}}. \tag{3.85}$$

The calculation of the annihilation part is very similar, but one has to pay attention to the little differences. First of all, the phase space integration takes a different form, as well as the momentum conservation.

$$\begin{aligned} E\frac{dR_{\rm ann}}{d^3p} = \frac{\mathcal{N}_{\rm ann}}{2(2\pi)^3}\int \frac{d^3p_1\, f_q(\mathbf{p}_1)}{2E_1(2\pi)^3}\frac{d^3p_2\, f_q(\mathbf{p}_2)}{2E_2(2\pi)^3}\frac{d^3p_3\,[1+f_g(\mathbf{p_3})]}{2E_3(2\pi)^3} \\ \times (2\pi)^4\delta^{(4)}(p_1+p_2-p_3-p)|\mathcal{M}_{\rm ann}|^2. \end{aligned} \tag{3.86}$$

The degeneracy factor for the annihilation part $\mathcal{N}_{\rm ann}$ only contains the sum over the squared quark charges:

$$\mathcal{N}_{\rm ann} = \frac{5}{9}. \tag{3.87}$$

We again set $q = p_1 - p$ and use the three dimensional part of the delta function to perform the integration over $\mathbf{p}_3$. The remaining delta function will be treated as above ($\omega = q^{(0)}$) to integrate ϕ_k:

$$\begin{aligned} \cos(\phi_k-\phi_q) = \frac{\omega^2-|\mathbf{q}|^2+2|\mathbf{k}|(\omega-|\mathbf{q}|\cos\theta_q\cos\theta_k}{2|\mathbf{q}||\mathbf{k}|\sin\theta_q\sin\theta_k} \equiv \eta, \\ \phi_{k,i} = \phi_q \pm \arccos\eta, \\ \delta(\omega+\mathbf{k}-|\mathbf{k}+\mathbf{q}|) \to 2|\mathbf{k}+\mathbf{q}|\sum_i \psi^{-\frac{1}{2}}\Theta(\psi)\delta(\phi_k-\phi_{k,i}), \end{aligned} \tag{3.88}$$

with the helper function

$$\psi \equiv 4|\mathbf{k}|^2|\mathbf{q}|^2\sin^2\theta_q\sin^2\theta_k - [\omega^2-|\mathbf{q}|^2-2|\mathbf{k}|(\omega-|\mathbf{q}|\cos\theta_q\cos\theta_k)]^2. \tag{3.89}$$

The squared matrix element is invariant under changes $p_1 \leftrightarrow p_2$, so we only need to calculate one of the two terms in (3.27) and note another factor 2, resulting in the same numerical pre-factor as for the Compton scattering part:

$$\begin{aligned} E\frac{dR_{\rm ann}}{d^3p} = \frac{5\alpha\alpha_s}{18\pi^6}\sum_i\int_{q^*}^\infty \mathbf{q}^2 d|\mathbf{q}|\int_0^\pi \sin\theta_q d\theta_q\int_0^{2\pi} d\phi_q\int_0^\infty |\mathbf{k}|d|\mathbf{k}|\int_0^\pi \sin\theta_k d\theta_k \\ \times \frac{f_q(\mathbf{p}+\mathbf{q})}{|\mathbf{p}+\mathbf{q}|} f_q(\mathbf{k})[1+f_g(\mathbf{q}-\mathbf{k})]\psi^{-\frac{1}{2}}\Theta(\psi)\left\{\frac{2p\cdot k}{q^2}\right\}\Big|_{\phi_k=\phi_{k,i}}. \end{aligned} \tag{3.90}$$

The total hard contribution is the sum of both the Compton scattering part and the annihilation part:

$$E\frac{dR_{\rm hard}}{d^3p} = E\frac{dR_{\rm com}}{d^3p} + E\frac{dR_{\rm ann}}{d^3p}. \tag{3.91}$$

The soft part (3.67) (notice that the photon momentum was called q earlier, so we switch $p \leftrightarrow q$ to be consistent with the nomenclature of the hard contribution):

$$E\frac{dR_{\rm soft}}{d^3p} = -\frac{e^2Q^2N_c}{2(2\pi)^3}\frac{8f_F(\mathbf{p})}{|\mathbf{p}|}\int\frac{d^3q}{(2\pi)^3}{\rm Im}[p\cdot S_R^\star(q)]. \tag{3.92}$$

Using (3.63), the scalar product $q \cdot S_R^\star(p)$ can be expanded:

$$E\frac{dR_{\text{soft}}}{d^3p} = -\frac{5}{12\pi^5}\alpha\frac{f_F(\mathbf{p})}{|\mathbf{p}|} \times \int d^3q\, \text{Im}\left\{\frac{q^{(0)}[p^{(0)} - \Sigma_R^{(0)}(q)] - \mathbf{q}\cdot[\mathbf{p} - \mathbf{\Sigma}_R(q)]}{[p^{(0)} - \Sigma_R^{(0)}(q)]^2 - [\mathbf{p} - \mathbf{\Sigma}_R(q)]^2}\right\}\Big|_{p^{(0)}=\mathbf{p}\cdot\hat{\mathbf{q}}}. \tag{3.93}$$

Explicit formulae from [76] are then used for Σ_0, $\Sigma_{x,y}$ and Σ_z. The integration measure can again be rewritten in spherical coordinates

$$\int d^3q = \int_0^{q^*} |\mathbf{q}|^2 d|\mathbf{q}| \sin\theta_q d\theta_q d\phi_q, \tag{3.94}$$

with the ultraviolet cut-off q^*. The fermionic distribution function is then replaced by the anisotropic distribution (2.4) from Ref. [52].

To compute the total photon production rate

$$E\frac{dR_{\text{total}}}{d^3p} = E\frac{dR_{\text{hard}}}{d^3p} + E\frac{dR_{\text{soft}}}{d^3p}, \tag{3.95}$$

a Monte Carlo integration routine, written by A. Ipp [60, 62], was used. This routine integrates each remaining coordinate separately for each of the contributions. Each of the integrations is performed a certain number of times and then averaged to increase statistics. The photon rates are computed for photon energies $p > 1\,\text{GeV}$, as we have not included all processes that would contribute to the photon production at lower energies.

To illustrate the important result of [61], a plot of the photon rates at different anisotropy parameters is shown in Fig. 3.9. Notice that the photon rates are suppressed near $\theta_p \approx \pi/2$ at $\xi > 0$. If we fold the computed photon rates from Fig. 3.9 with the time-evolution model from (2.9), we get a time-dependent photon rate depicted in Fig. 3.11. One immediately notices a number of unphysical kinks in the time-dependent photon rates. These are a result of how the numerical data is being processed and used for further computations.

First, the Monte Carlo routine calculates the photon rates for various ξ, θ_p and E/p_{hard}. Due to the nature of Monte Carlo integration, one needs a large amount of data to get stable and reliable results - meaning that the calculation of a dataset for different ξ, θ_p and E/p_{hard} should be repeated as often as possible to gather enough statistics. Additionally, one would also need to perform the calculation for as many different parameters as possible. As the calculations take some time (approximately 10 seconds per datapoint on a conventional desktop computer), one has to find a compromise regarding the amount of statistics versus the density of the parameter space in ξ, θ_p and E/p_{hard}. Ultimately, the following set was chosen:

- E/p_{hard}: 1 to 15 with spacing of 1,
- θ_p from 0 to $\pi/2$ with a spacing of $2\pi/15$,
- ξ: 0, 1, 10, 30, 100, 200.

The datasets are read into a *Mathematica* notebook and the photon rates are calculated by averaging over all datasets. To allow for a seamless usage of the numerical data within the computer algebra system, the data is being interpolated linearly between the actual sampling points of the parameter space. Despite the rather crude spacing of ξ, the interpolation works well in preserving the behavior

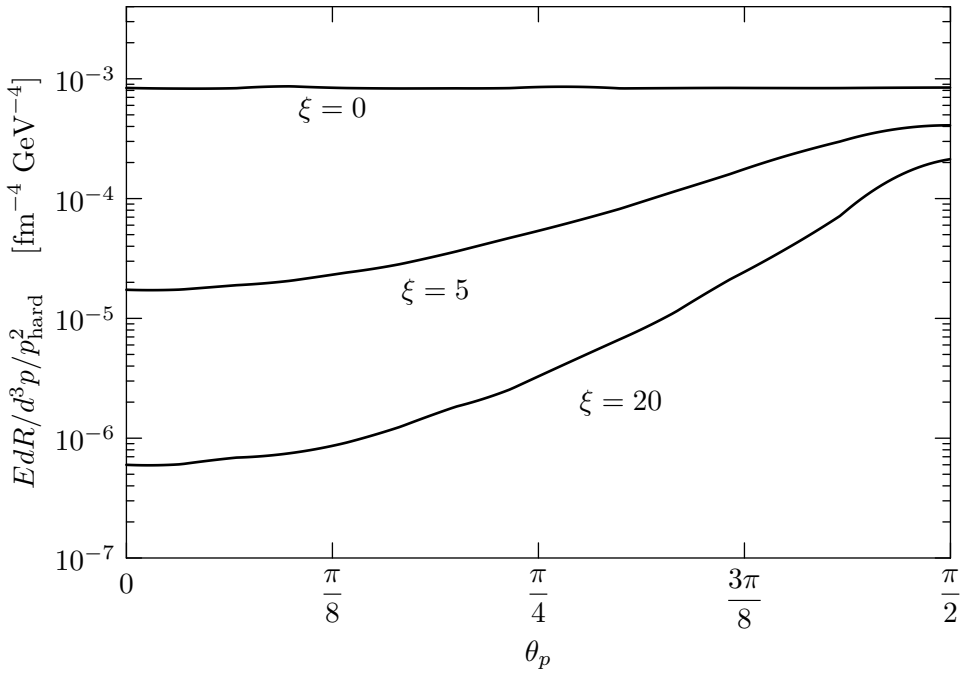

Figure 3.9: Photon rates as a function of emission angle θ_p, similar to Fig. 2 in [61]. The polar angle θ_p is measured from the beam axis, so $\theta_p = \pi/2$ points to the transverse direction, whereas $\theta_p = 0$ is parallel to the beam. ($E/p_{\rm hard} = 5$).

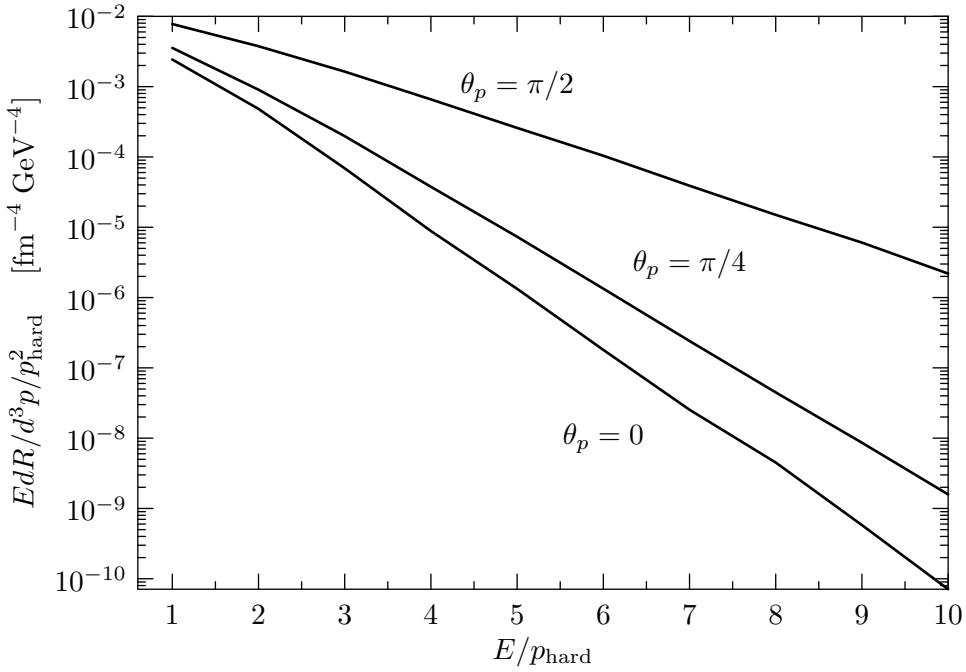

Figure 3.10: This figure shows the photon rates as a function of $E/p_{\rm hard}$ at different photon emission angles. $\xi = 10$ for all curves.

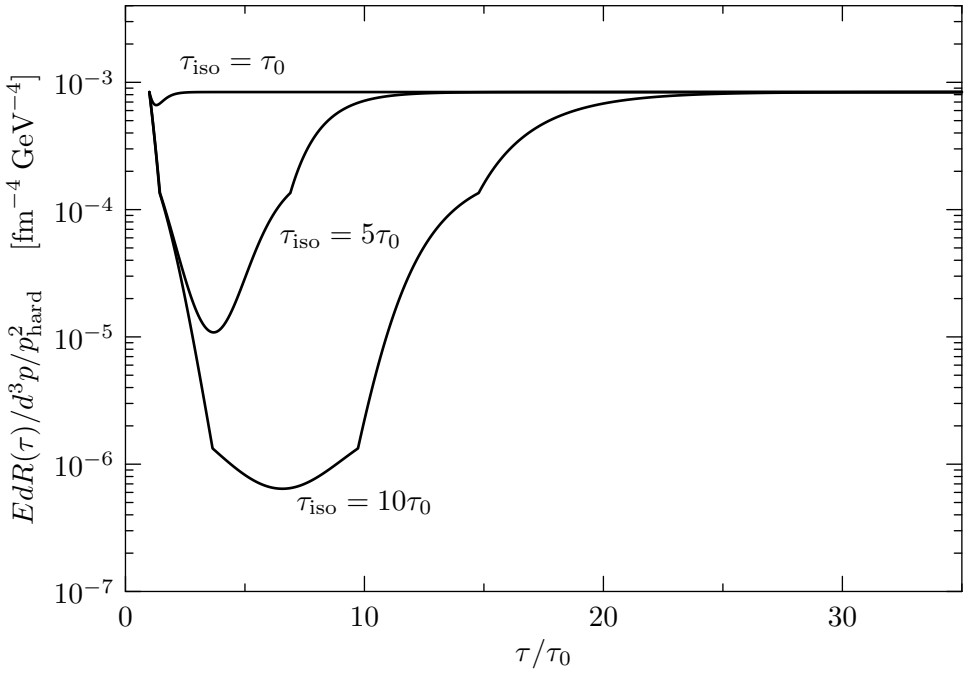

Figure 3.11: Photon rates in forward direction ($\theta_p = 0$) with time-dependent anisotropy parameter ξ and different isotropization times $\tau_{\rm iso}$, but constant temperature (no plasma cooling). $E/p_{\rm hard} = 5$,$\gamma = 2$, $\delta = 2$.

of the function (Fig. 3.12). Since the parameter space is three dimensional, a linear interpolation between the points was chosen as the most straightforward implementation. While the interpolation seems to be working as expected for different values of ξ, the matter is slightly more complicated for the time-evolution in Fig. 3.11. The proper time τ enters the ξ-model in a power law (2.9) and thus produces these kinks at the times, in which ξ equals one of the sampling points. Even for a more densely spaced dataset in ξ, the dips would not vanish due to the power law describing the time evolution of the anisotropy.

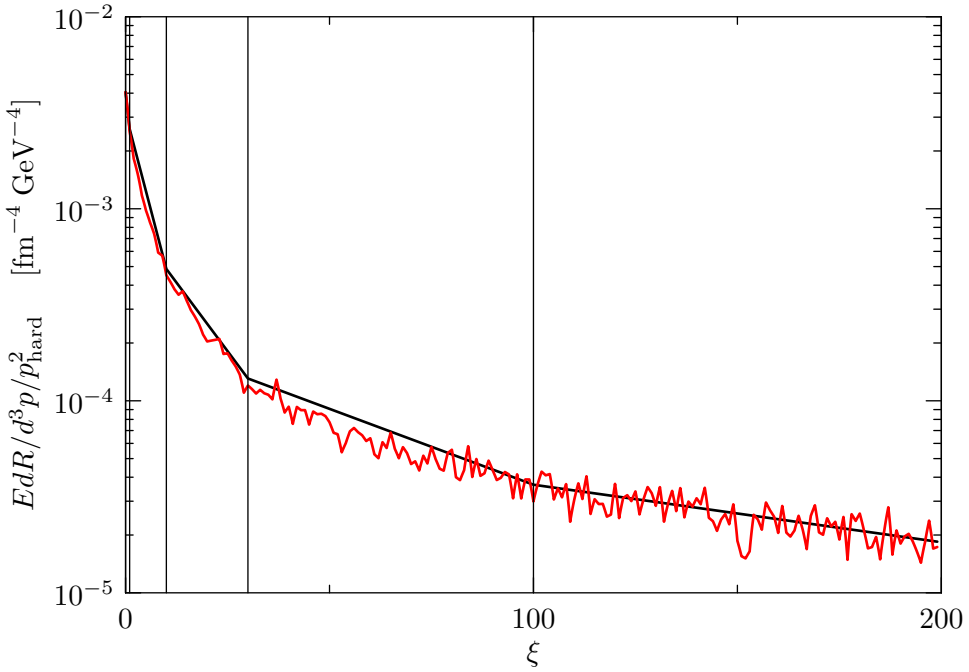

Figure 3.12: This figure shows the photon rate as a function of ξ for a fixed E/p_{hard}. The black line represents the interpolated curve with sampling points for ξ as mentioned earlier in the text. The vertical lines indicate those sampling points. The waggly, red line is the same function, only sampled at a higher rate ($\xi = 1, 2, 3 \ldots 200$) and with only one dataset. This also shows how a larger number of datasets is needed for good statistics, especially in the higher region of ξ. $\theta_p = 0$, $E/p_{\mathrm{hard}} = 1$.

Bosco: It's a bargain, trust me, trust me.
Sam: I never trust a man that says trust me twice.
– Sam & Max Save The World

4
Double pulses

4.1. Overview

With the results from Chapter 3, we are able to compute the photon emission rate EdR/d^3p in a quark-gluon plasma with momentum-space anisotropies. In the end, we are keen on calculating a direct photon signal that could be registered by photon detectors in heavy-ion experiments.

Such a photon signal is accomplished by integrating the photon rate (3.95) over the space-time evolution of the quark-gluon plasma. As we have sketched previously (Fig. 2.2), we assume that the QGP expands parallel to the beam direction - the transverse expansion will be omitted for the time being.

By folding the model-dependent photon rates over the entire evolution of the plasma until its freezeout and taking care of the special geometry of this problem, we obtain a photon signal at a detector placed far away from the plasma. By the interplay of the geometry, several parameters such as the collision centrality, as well as the anisotropy-dependent photon rate, two successive photon peaks with durations on the order of yoctoseconds, are possible.

The notation has been kept similar to [28, 77].

4.2. Photon emission model

4.2.1. Transformation of the photon rate

The number of photons N emitted from a certain four-volume element tV of the plasma is given by

$$N = R\,tV, \tag{4.1}$$

with (constant) R being the phase-space integrated differential photon rate dR. Since the photon rate will be a function of time at least, one has to rewrite the product as a space-time integral

$$N = \int_{tV} R(x)\; d^4x = \int\int_{tV} f(p,x)\delta(p^2)\; d^4x\; d^4p, \tag{4.2}$$

with

$$f(p,x)\delta(p^2) \equiv \frac{dR}{d^4p}. \tag{4.3}$$

The delta function represents the on-shell condition for the photons: $p^2 = [p^{(0)}]^2 - \mathbf{p}^2 \equiv \omega^2 - \mathbf{p}^2 = 0 \rightarrow \omega^2 = \mathbf{p}^2$. As mentioned before, we want to make use of the Lorentz-boost invariance of the central rapidity region of the plasma, hence we need to consider the transformation behavior. The

photon number N, the squared photon momentum p^2, as well as the infinitesimal four-volumes d^4x and d^4p are Lorentz scalars. Therefore, the photon rate R and the differential photon rate f have to be Lorentz scalars as well.

Each element of the plasma is related via Lorentz-boosts along the beam axis z - and the Bjorken model tells us that the physics at each of these points along such a boost is the same, as long as the boosts remain within the central rapidity plateau. We use the simplification to lengthen this plateau section of the plasma to an infinite extent, so that the boost-invariance holds for all points within the QGP.

The explicit expressions for the invariance of f under Lorentz-boosts is

$$f(p,x) = \bar{f}(\bar{p},\bar{x}) = \bar{f}(\Lambda p, \Lambda x). \tag{4.4}$$

Variables with a bar represent quantities in the local plasma rest frame, opposed to variables in the laboratory frame without the bar. Λ is the Lorentz matrix for boosts in the positive z-direction

$$\Lambda = \begin{pmatrix} \gamma & 0 & 0 & -\beta\gamma \\ 0 & 1 & 0 & 0 \\ 0 & 0 & 1 & 0 \\ -\beta\gamma & 0 & 0 & \gamma \end{pmatrix}, \tag{4.5}$$

β is the velocity of a certain infinitesimal volume element in the plasma

$$\beta(t,z) = \frac{z}{t}, \tag{4.6}$$

with z being the position of said volume element and $\gamma = \sqrt{1-\beta^2}^{-1}$. This choice for β is an implementation of rapidity invariance: all elements of the plasma travel away from the same origin ($z = 0$). To calculate the number of photons N arriving at a detector D at a certain laboratory time t_d, one needs to integrate the differential rate $f(p,x)$ along an adequate line in the Minkowski diagram. This integration ensures that we get all the contributions from the expanding QGP, as photons emitted earlier from the far away region of the plasma will arrive at the same time t_d as some photons emitted later in the regions closer to the detector. Such a space-like curve can be parametrized as

$$\mathbf{z}(t) = x_p\hat{\mathbf{p}}_1 + y_p\hat{\mathbf{p}}_2 + \hat{\mathbf{p}}(t - t_d + d) \tag{4.7}$$

and represents all photons that arrive at the laboratory time $t = t_d$ at the detector D placed at $z = d$ away from the origin. $\hat{\mathbf{p}}$ is the unit vector of the light wave vector $p = (\omega, \mathbf{p})$. Both $\hat{\mathbf{p}}_1$ and $\hat{\mathbf{p}}_2$ are perpendicular to $\mathbf{p}$ and will allow us shifts in the transverse directions with the spatial parameters x_p and y_p.

To account for all these photons, we integrate f in the laboratory frame over all times $t_1 < t < t_2$ along the curve $\mathbf{z}(t)$ to get the differential photon rate at the detector:

$$f_d(p,t_d) = \int_{t_1}^{t_2} dt f(p,\mathbf{z}(t)). \tag{4.8}$$

The differential rate at the detector is integrated over all photon momenta according to Eq. (4.3) via

the on-shell condition:

$$\begin{aligned} R_d(t_d) &= \int f_d(p, t_d)\, \delta(p^2) d^4p \\ &= \int f_d(\omega, \mathbf{p}, t_d)\, \delta(\omega^2 - \mathbf{p}^2)\, d\omega d^3p. \end{aligned} \tag{4.9}$$

At this stage, the detector D spans up the solid angle of an entire sphere 4π, enclosing the entire plasma. Only later we will pick a certain detector position. The delta function in Eq. (4.9) has two roots at $\omega = \pm|\mathbf{p}|$. Since ω in our case is strictly positive, the negative energy solution is dropped, leaving us with

$$\delta(\omega^2 - \mathbf{p}^2) = \frac{1}{2|\mathbf{p}|}\delta(\omega - |\mathbf{p}|) \tag{4.10}$$

and

$$\begin{aligned} R_d(t_d) &= \int f_d(\omega, \mathbf{p}, t_d)\, \frac{1}{2|\mathbf{p}|}\delta(\omega - |\mathbf{p}|)\, d\omega d^3p \\ &= \int f_d(|\mathbf{p}|, \mathbf{p}, t_d)\, \frac{1}{2|\mathbf{p}|} d^3p. \end{aligned} \tag{4.11}$$

To evaluate Eq. (4.11), one has to make an idealistic assumption on the behavior of the photon detector. We now consider the detector to have a finite area A_d and is placed into the direction of $\hat{\mathbf{p}}$. Additionally, we assume that it only registers photons which arrive with a wave vector pointing parallel to $\hat{\mathbf{p}}$ - alternatively, one could say that the detector is sufficiently far enough from the collision center and the vector $\hat{\mathbf{p}}$ is fixed at a certain polar angle. This allows us to split up the integration and neglect the angular dependence of the differential rate f_d:

$$\begin{aligned} R_d(t_d) &\approx \int_{A_d} d\Omega \int f_d(p, t_d) \frac{1}{2|\mathbf{p}|}\mathbf{p}^2\, d|\mathbf{p}| = \frac{A_d}{4\pi d^2} \int \frac{\omega}{2} f_d(\omega, t_d)\, d\omega \\ &= \int R_d(\omega, t_d)\, d\omega. \end{aligned} \tag{4.12}$$

The differential rate f_d as well as the rate R_d are still implicitly a function of the transverse shifts x_p and y_p. For the total number of photons registered between t_a and t_b, the only step left is to integrate these transverse shifts over the interaction region A_N:

$$N(t_a, t_b) = \frac{A_d}{8\pi d^2} \int_{A_N} dx_p\, dy_p \int_{t_a}^{t_b} dt_d \int d\omega\, \omega\, W(\omega)\, f_d(\omega, t_d), \tag{4.13}$$

where $W(\omega)$ is an arbitrary detector window function, which in the simplest case is $W(\omega) = \delta(\omega - \omega_d)$ to pick out a single frequency. This would be analogous to an ideal detector that is capable of resolving any specific photon frequency ω_d.

We have defined the differential rate in Eq. (4.8), which features $f(p, \mathbf{z}(t))$ as observed in the laboratory frame of the detector. As we calculate the photon rate in the rest frame of a volume element in the plasma, the aforementioned transformations have to be applied to relate the two frames of reference to each other:

$$\bar{f}(\bar{\omega}, \bar{t}, \bar{z}) = f(\omega, t, z). \tag{4.14}$$

Explicitly, the transformation of both position vector and wave vector read:

$$\begin{aligned} \bar{r} = \Lambda(\beta)x = \Lambda(\beta)\begin{pmatrix} t \\ x \\ y \\ z \end{pmatrix} = \begin{pmatrix} t/\gamma \\ x \\ y \\ 0 \end{pmatrix}, \\ \bar{p} = \Lambda(\beta)p = \Lambda(\beta)\begin{pmatrix} \omega \\ p_x \\ p_y \\ p_z \end{pmatrix} = \begin{pmatrix} \gamma\omega - \beta\gamma p_z \\ k_x \\ k_y \\ \gamma k_z - \beta\gamma\omega \end{pmatrix}. \end{aligned} \tag{4.15}$$

and finally

$$f(\omega, t, z) = \bar{f}(\gamma(\omega - \beta p_z), t/\gamma, 0). \tag{4.16}$$

The x and y coordinates, which should not be confused with the shifts x_p and y_p, are not affected by the transformation. Since we are interested in the time-dependent photon rate, we can omit the t_d-integration in the last step and, using the delta-like detector window function, get

$$\frac{dN}{dt_d\, d\omega_d} = \frac{A_d}{8\pi d^2}\int_{A_N} dx_p\, dy_p \int_{t_a}^{t_b} dt\, \omega_d\, \bar{f}(\gamma(\omega_d - \beta p_z), t/\gamma). \tag{4.17}$$

To connect the result in Eq. (4.17) to our previously computed photon rates, we can use Eq. (4.11):

$$\begin{aligned} R_d(t_d) \equiv \int \frac{dR(t_d)}{d^3p} d^3p = \frac{A_d}{4\pi d^2}\int f_d(p, t_d)\frac{1}{2|\mathbf{p}|}\mathbf{p}^2\, d|\mathbf{p}| \\ \rightarrow f_d(\omega, t_d) = \bar{f}(\gamma(\omega - \beta p_z, t/\gamma)) = 2\omega\frac{dR(t_d)}{d^3p}, \end{aligned} \tag{4.18}$$

where $dR(t_d)/d^3p$ is simply the detector rate dR/d^3p integrated along a curve such as Eq. (4.7).

All of the formulae and equations in this section have been written with as few parameters as possible in order to give a clean derivation of Eq. (4.17). However, the transformed photon rate $\bar{f}$ is a function of the photon frequency $\bar{\omega}$ and the proper time t/γ. Since both depend explicitly on β, they are also functions of the curves $\mathbf{z}(t)$, which again are implicitly functions of the detector time t_d. Additionally, through the relation in Eq. (4.18), the transformed photon rate incorporates all the dependencies that have been worked out in Chapter 3, e.g. the anisotropy parameter, the plasma temperature as well as all the remaining parameters from the Martinez-Strickland model [51, 53].

4.2.2. Relativistic Doppler shift

Equation (4.15) shows the transformational behavior of a photon wave vector p. The frequency (or energy) ω of this photon transforms as

$$\bar{\omega} = \gamma(\omega - \beta p_z), \tag{4.19}$$

which is known as the relativistic Doppler shift. Photons emitted from volume elements of the plasma at different positions z will therefore be subject to Doppler shifts with different strengths. With

$$p_z = \omega\cos\theta, \tag{4.20}$$

the Doppler factor reads

$$\frac{1-\beta\cos\theta}{\sqrt{1-\beta^2}}. \tag{4.21}$$

The Doppler factor is equal to 1 at

$$\beta_0 = \frac{2\cos\theta}{\cos^2\theta+1}, \tag{4.22}$$

and

$$\beta_0 = 0. \tag{4.23}$$

If we place the detector D at some finite positive z, volume elements with $0 < \beta < \beta_0$ emit photons with frequency $\bar{\omega}$ that are registered as blue-shifted photons with $\omega > \bar{\omega}$. Photons that are emitted from portions of the plasma with $\beta < 0$ and $\beta > \beta_0$, on the other hand, will arrive red-shifted ($\omega < \bar{\omega}$). This is a very important detail, as it plays a crucial role in the phenomenology of the double pulse generation.

If we translate this conclusion into the framework of the Bjorken picture (Fig. 2.1), we see that the Minkowski diagram is split up in three different parts (Fig. 4.1). The actual strength of the shift will

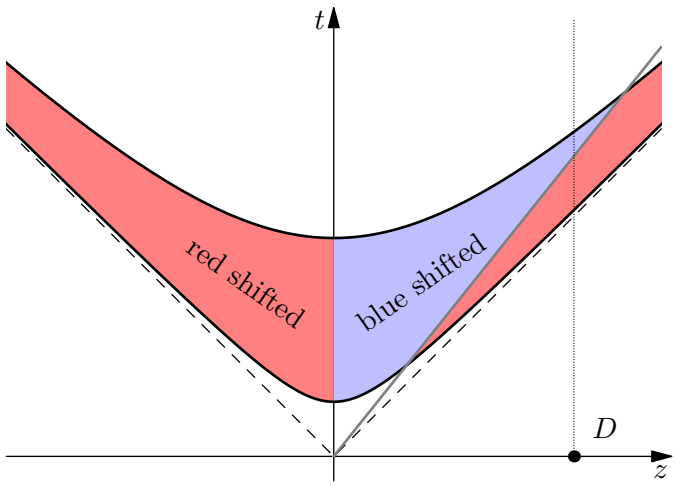

Figure 4.1: Regions with blue- and red-shifted photons in the Minkowski diagram of the Bjorken picture at $\theta_p = \pi/4$. Although the shading is constant in this illustration, the strength of the Doppler effect increases with growing z. For smaller angles, the gray line separating the blue- and red shifted parts tilts more towards the light cone according to $t = z(1+\cos^2\theta_p)/(2\cos\theta_p)$.

finally depend on the z-component of the space-like curve $\mathbf{z}(t)$. Photons emitted at $\theta_p = \pi/2$ have $p_z = 0$ and experience redshift in the entire Minkowski diagram. Bringing back to mind the energy dependence of the photon rates (Fig. 3.10), one can immediately see that the differently shifted areas correspond to different emission rates. Blue shifted photons were emitted at lower energy and are therefore higher in numbers.

The position of the detector is encoded in the Lorentz transformations and the choice of the sign of β and has to agree with the parametrization of the curve in Eq. (4.7).

4.2.3. Interaction region and temperature dependence

The calculation of the photon rate requires the integration over the interaction region, which we call A_N. This interaction region is defined as the transverse spatial extent of the quark-gluon plasma. Heavy-ion collisions are additionally parametrized by the impact parameter b, which is the distance between the centers of the nuclei. This centrality parameter hence defines the total volume of the QGP and will have an important effect on the photon emission as well.

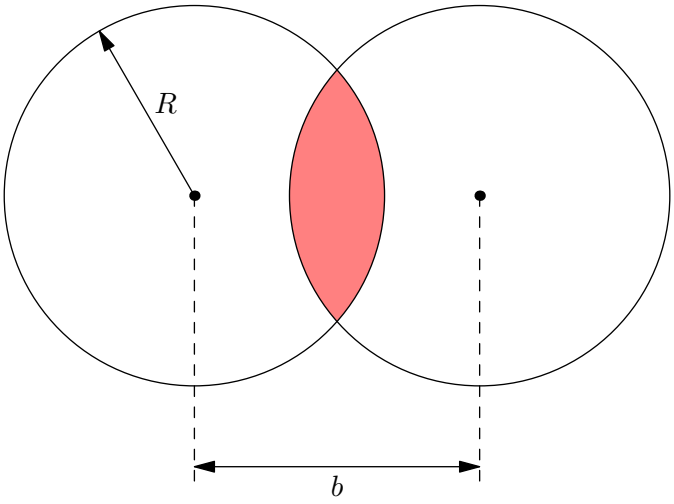

Figure 4.2: The red shaded interaction region, within which the QGP is created in the transverse plane. The radius of the nuclei is denoted by R and the impact parameter, which is the distance between the two centers of the nuclei, is denoted by b.

Figure 4.2 shows a sketch of the interaction region. It depicts the heavy ion collision from a view parallel to the beam. The two nuclei with radius R overlap according to the impact parameter b, creating the quark-gluon plasma in the red shaded intersection A_N.

One possible way of tackling the integration over A_N in Eq. (4.17) is to assume that the photon rate is independent from its location in the interaction region - equivalently formulated, the temperature of the plasma is taken as constant in the transverse plane. This reduces the integration over A_N to a simple scaling factor. Although computation time is reduced in this approximation, the rather sharp jump in temperature at the borders of the interaction region produces unphysical artifacts in the photon signals.

We can use a temperature profile based on the local nucleon density for each of the two nuclei [49, 78]:

$$T(x,y) = T_0 \left[2 \left(1 - \frac{x^2+y^2}{R^2} \right) \right]^{\frac{1}{4}}, \tag{4.24}$$

with some initial temperature T_0. The above temperature profile is based on a spherical density according to the Glauber model [79] and can be extended to the case of non-vanishing impact parameters:

$$\begin{aligned} T(x,y) = T_0 \left[4 \left(1 - \frac{(x-b/2)^2+y^2}{R^2} \right) \left(1 - \frac{(x+b/2)^2+y^2}{R^2} \right) \right]^{\frac{1}{8}} \\ \times \Theta[R^2-(x-b/2)^2-y^2)] \cdot \Theta[R^2-(x+b/2)^2+y^2)]. \end{aligned} \tag{4.25}$$

The theta functions make sure that the temperature is exactly zero, if x and y are outside the overlap region. Figure 4.3 illustrates the temperature profile for a non-central collision.

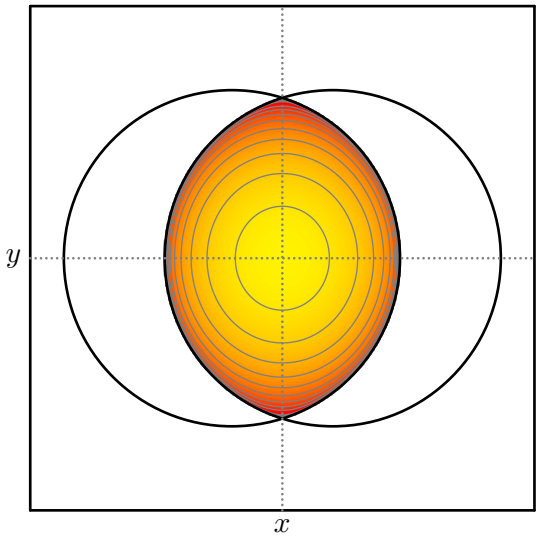

Figure 4.3: Schematic density plot of the temperature profile (4.25) with a non-vanishing impact parameter b (see Fig. 4.2). The yellow area in the center has the highest temperatures. The temperature drops off towards the border of the interaction region, represented by the orange and red shading.

One little detail needs to be kept in mind about the non-central temperature profile. It is evident in Eq. (4.25) that for $b \neq 0$, the initial temperature T_0 cannot be recovered at the center of the interaction region ($x = 0, y = 0$). This lower initial temperature of the plasma will eventually lead to a faster freezeout.

The vectors $\hat{\mathbf{p}}$ and $\hat{\mathbf{p}}_1$ are chosen to lie in the so-called reaction plane, $\hat{\mathbf{p}}_2$ is oriented orthogonal:

$$\hat{\mathbf{p}} = \begin{pmatrix} \sin\theta_p \\ 0 \\ \cos\theta_p \end{pmatrix}, \quad \hat{\mathbf{p}}_1 = \begin{pmatrix} \cos\theta_p \\ 0 \\ -\sin\theta_p \end{pmatrix}, \quad \hat{\mathbf{p}}_2 = \begin{pmatrix} 0 \\ 1 \\ 0 \end{pmatrix}, \tag{4.26}$$

illustrated in Fig. 4.4.

The above choice for the photon wave vector also determines the curve $\mathbf{z}(t)$:

$$\mathbf{z}(t, t_d, x_p, y_p) = \begin{pmatrix} x(t, t_d, x_p, y_p) \\ y(t, t_d, x_p, y_p) \\ z(t, t_d, x_p, y_p) \end{pmatrix} = \begin{pmatrix} x_p \cos\theta_p + (t - t_d + d)\sin\theta_p \\ y_p \\ -x_p \sin\theta_p + (t - t_d + d)\cos\theta_p \end{pmatrix}. \tag{4.27}$$

In accordance with [28], the photon rate dN will be calculated per unit solid angle $d\Omega_d$ ($A_d = \Omega_d \cdot d^2$):

$$\frac{dN}{dt_d\, d\omega_d\, d\Omega_d} = \frac{1}{8\pi} \int_{A_N} dx_p\, dy_p \int_{t_a}^{t_b} dt\, \omega_d\, \bar{f}(\gamma(\omega_d - \beta p_z), t/\gamma). \tag{4.28}$$

There are two possible ways to implement the integration boundaries for the interaction region depicted in Fig. 4.2. One is to write y_p as a function of x_p. We choose the other way and write the x_p in terms

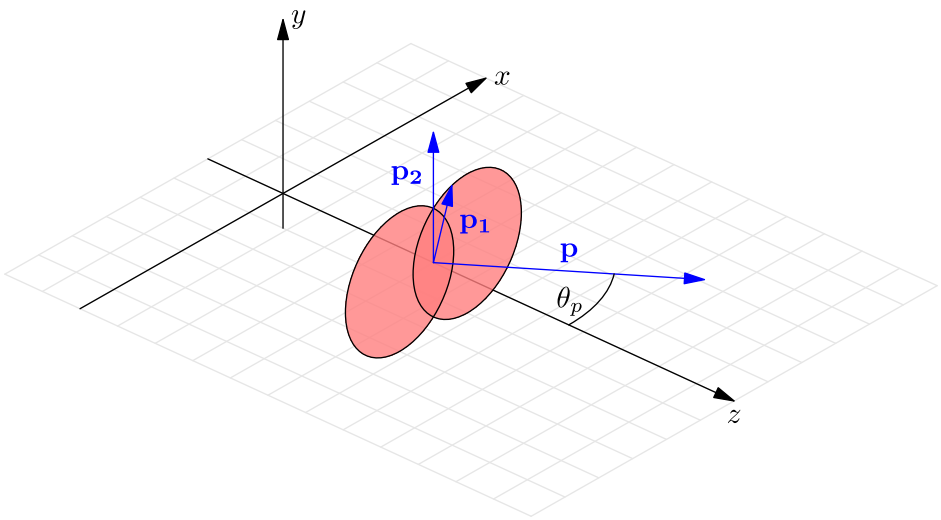

Figure 4.4: A sketch of the two nuclei in the reaction plane (gray grid). The blue arrows represent the photon wave vector $\mathbf{p}$ enclosing the polar emission angle θ_p as well as the orthogonal shifting vectors $\hat{\mathbf{p}}_1$ and $\hat{\mathbf{p}}_2$ (arrow lengths are not to scale).

of y_p. Since $y = y_p$ in Eq. (4.7), we can write easily for $x = 0$

$$-R^2 + \left(\frac{b}{2}\right)^2 \leq y_p \leq R^2 - \left(\frac{b}{2}\right)^2. \tag{4.29}$$

To complete the integration over A_N, the y_p-dependent integration boundaries for x_p are:

$$\frac{-\sqrt{R^2 - y_p^2} + \frac{b}{2} - (t - t_d + d)\sin\theta_p}{\cos\theta_p} \leq x_p \leq \frac{\sqrt{R^2 - y_p^2} - \frac{b}{2} - (t - t_d + d)\sin\theta_p}{\cos\theta_p}. \tag{4.30}$$

As the boundaries for x_p are a function of the laboratory time t and the shift y_p, the order of integration in Eq. (4.28) has to be changed if the integration is carried out successively. These integration boundaries ensure that we only include photon contributions that are within the spatial extent of the quark-gluon plasma. For $\theta_p = 0$, the shape of the plasma in terms of x_p and y_p coincides with Fig. 4.2. Changing the photon emission angle results in a skewed interaction region in x_p and y_p, illustrated in Fig. 4.5.

Due to the cosine term in the denominator, the integration boundaries for x_p diverge for $\theta_p = \frac{\pi}{2}$. The local coordinate system $\hat{\mathbf{p}}$, $\hat{\mathbf{p}}_1$ and $\hat{\mathbf{p}}_2$ rotates in a way that x_p-shift points into the beam direction z, so that the boundaries for x_p is essentially the light cone.

Inherently, the integration over the laboratory time t should cover the total interval, in which the space-like curve $\mathbf{z}(t)$ passes through the total volume of the quark-gluon plasma. If we were choose θ_p equal to zero, we would need to integrate until infinity, as our QGP is not bounded along the beam axis. At some point, the temperature of the plasma will drop below the freezeout temperature T_c and cease to exist. The integration is stopped at this specific time as well. This exact point of the plasma freezeout using the models from Chapter 2 is only accessible numerically. Still, we need some upper and lower bounds for t to use as limits for the computation. These bounds can be derived by demanding that the curve lies within the light cone ($|z| \leq t$) with the condition that $|x| \leq R$. We can eliminate x_p from Eq. (4.7):

$$x \cdot \sin\theta_p + z \cdot \cos\theta_p = t - t_d + d, \tag{4.31}$$

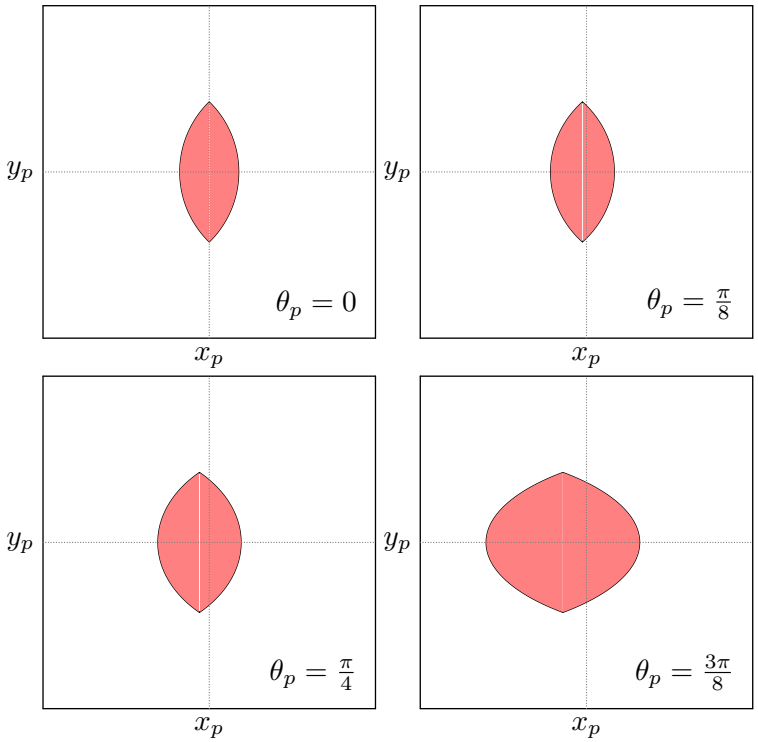

Figure 4.5: This illustration shows the distortion of the interaction region in dependence of x_p and y_p for some non-vanishing laboratory time t.

where x and z are a shorthand notation for $x(t, t_d, x_p, y_p)$ and $z(t, t_d, x_p, y_p)$. This equation relates all photons produced at position (x, z) at laboratory time t, which arrive at the time t_d at the detector placed at a distance d. By setting $z = t$, $x = R$ for the lower bound and $z = -t$, $x = -R$ for the upper bound, we get the valid interval for t:

$$\frac{t_d - d - R\sin\theta_p}{1 + \cos\theta_p} \leq t \leq \frac{t_d - d + R\sin\theta_p}{1 - \cos\theta_p}. \tag{4.32}$$

These bounds strictly only hold for $y_p = 0$. As a result of the location of the interaction plane, the extent of the QGP is maximal at $y_p = 0$. So this choice of integration bounds for t will not result in ignoring contributions from the plasma, because the limits cut off too early in either direction. We then simply drop all contributions that do not lie in the overlap region within the numerical integration. This ensures that the curve $\mathbf{z}(t)$ is limited to the volume of the QGP.

4.3. Analytic toy model for the one-dimensional plasma

Before we start with the full numerical treatment, we can try to analytically investigate at least parts of the calculation with a radically simplified model. Step number one in this approximation would be to reduce the transverse area of the QGP to a point, turning it into a wire. This approach also comes with the advantage that we can use the two dimensional Minkowski diagram without having to worry about the two other spatial dimensions in which the curve $\mathbf{z}(t)$ lives.

Imposing $\delta(x)\delta(y)$ onto the curve (4.7) yields an expression for x_p, while y_p is trivially zero:

$$\begin{aligned} x &= x_p \cos\theta_p + (t - t_d + d)\sin\theta_p = 0, \\ x_p &= -(t - t_d + d)\tan\theta_p. \end{aligned} \tag{4.33}$$

Inserting this expression for z gives

$$z = (t - t_d + d)\sec\theta_p. \tag{4.34}$$

Let us have a first look at how $\mathbf{z}(t)$ integrates in the Minkowski diagram of the Bjorken picture. Figure 4.6 shows $z(t)$ embedded in the $z - t$ plane of the Minkowski diagram. The photon emission angle θ_p is identical with the angle of the curve to the time axis in the one dimensional case. At $\theta_p = \pi/2$, the curve is parallel to the z axis, which means that all photons emitted at a certain laboratory time t arrive at the same time at the detector. Such curves in the Minkowski diagram apparently feature superluminal speeds, as they are tilted farther than the light cone. This is not in contradiction to special relativity. The curve is not a world line of a particle and does not describe the path of a single photon. Every point along this curve emits photons that arrive at laboratory time t_d at the detector. These emitted photons would be represented by world lines with an angle of 45° towards the $t = 0$ plane in a t, x, z coordinate system. A curve like $\mathbf{z}(t)$ is hence a space-like curve.

We can also observe the integration limits for t as in Eq.(4.32), where R has been set to zero. For the full numerical calculation, the contributions from earlier proper times than the formation time τ_0 will of course be omitted. In the next step, we have to find an expression for the photon rate. The complete

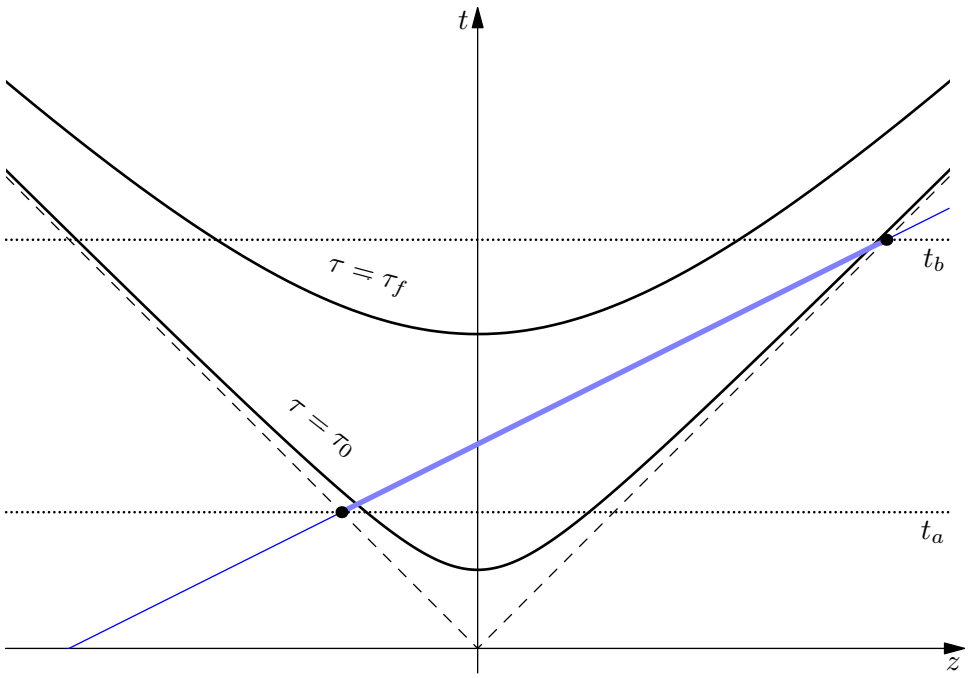

Figure 4.6: The curve $\mathbf{z}(t)$ (blue) embedded in the Minkowski diagram of the Bjorken picture at some finite $t_d - d$. Integration limits t_a and t_b at the intersection with the light cone are indicated by vertical, dotted lines.

model, as introduced in Chapter 2 is too complicated to handle in an analytic way. A feasible toy model should nevertheless encompass the three main aspects of the full concept: rapidity invariance, Doppler shift and the suppression during the anisotropy build-up. Figure 3.11 already gives a good

impression on how the time dependent photon rate combined with the full model will look like. We expect a first peak shortly after the formation at τ_0, which will subsequently get suppressed by the growing momentum space anisotropy. The anisotropy parameter will reach its maximum near τ_{iso} and then drop off, during which the photon rate will rise again. During this entire time, the plasma cools off until it reaches the freezeout temperature, at which we parametrically set the photon rate to zero.

For the toy model, this rather complicated process will be replaced by two Gaussians - the first, shorter one, will give us the photon rate shortly after the formation, while the second, longer one, will represent the rising photon rate due to the isotropization of the plasma. This way, we can mimic the suppressed photon rate during the anisotropy build up via the minimum between the two Gaussians. Based on the thermal photon production rate in an isotropic QGP which is given by [57]

$$E\frac{dR}{d^3p} = \frac{6}{9}\frac{\alpha\alpha_s}{2\pi^2}T^2 e^{-E/T}\ln\left(1+\frac{2.912}{4\pi\alpha_s}\frac{E}{T}\right), \tag{4.35}$$

we can extract the exponential term $\sim e^{-E/T}$ to give us a rough idea on how to implement the spectrum in the toy model. Incorporating the Doppler shift, the first term in our model will be

$$\exp\left[-\gamma(1-\cos\theta_p\cdot\beta)\frac{B}{T}\right], \tag{4.36}$$

where B is a model parameter that is related to the detected frequency (energy) ω_d. To account for the rapidity invariant portion of the photon rate, we employ a Gaussian as a function of proper time $\tau = t/\gamma$:

$$A\exp\left[(t/\gamma-\tau)^2\cdot C\right], \tag{4.37}$$

where A controls the amplitude of the photon rate and C is a parameter that determines the width of the Gaussian. Multiplying Eq. (4.36) and Eq. (4.37) we get our toy model

$$f_i = A_i\exp\left[-\gamma(1-\cos\theta_p\cdot\beta)\frac{B_i}{T}-(t/\gamma-\tau_i)^2\cdot C_i\right]. \tag{4.38}$$

The three parameters A_i, B_i and C_i characterize the overall scaling of each Gaussian to give some control over the model. Each of the τ_i represent proper times, at which the Gaussians have a maximum, roughly corresponding to the formation time τ_0 and the isotropization time τ_{iso}. While ξ does not actually vanish at the isotropization time in the free streaming model, it is still a timescale which we can use in this simplified case. Note that the constraint of the plasma starting to exist at τ_0 is not incorporated. The temperature T will be set to $T = 1/\tau$, which conveniently cancels the γ in the first term:

$$f_i = A_i\exp\left[-(1-\cos\theta_p\cdot\beta)B_i t-(t/\gamma-\tau_i)^2\cdot C_i\right]. \tag{4.39}$$

Plots to show the photon rates in the Minkowski diagram are seen in Fig. 4.7. One must be very cautious in the interpretation of this toy model, especially the second plot in Fig. 4.7. At $\theta_p = \pi/2$, we do not expect momentum-space anisotropies to form such a deep minimum in the photon rate, as is depicted by the large white space in the contour plot between the two maxima. This is merely an aspect of the toy model's limitations, as the photon rate suppression should show a clear dependence on the photon emission angle.

Unfortunately, even this very simple model for the photon rate can not be integrated analytically, due to terms like

$$\int dt\exp\left[\sqrt{(t+c_1)^2+c_2}\right]. \tag{4.40}$$

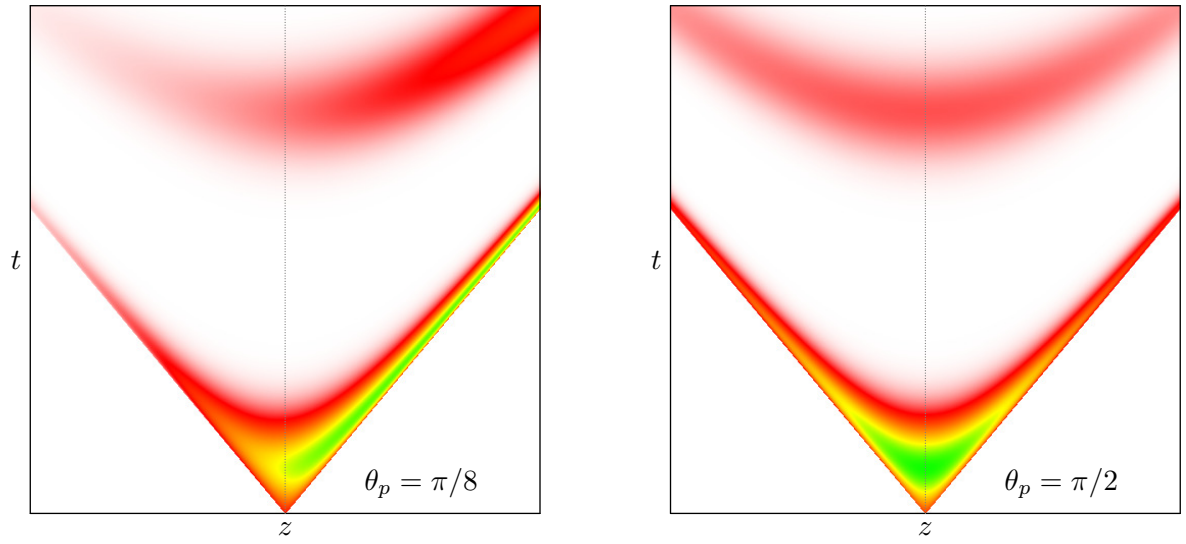

Figure 4.7: Contour plots showing the two peaks of the photon rate toy model in the Minkowski diagram. Yellow and green areas indicate higher photon rates, whereas white regions represent very low rates. One can see the effect of the Doppler shift by observing the yellow and green shaded parts of the plot. For $\theta_p = \pi/8$, the Doppler effect causes a blue-shift in the $z > 0$ half of the diagram, causing higher photon rates. At $\theta_p = \pi/2$, the Doppler shift affects both halves of the diagram in the same way, as the term proportional to β vanishes. The plasma in the toy model is formed at $t = 0$ and has non-vanishing photon rates for $\tau < \tau_0$.

To still gain some insight, we make a second approximation. If we model our two Gaussians to be infinitely short, the integral can be folded with delta functions at the proper times τ_1 and τ_2.

Equal proper time hyperbolas are defined through

$$t^2 = \tau_i^2 + z^2, \tag{4.41}$$

which we use as arguments in delta functions:

$$\delta(t^2 - \tau_i^2 - z^2). \tag{4.42}$$

Using the curve $z = (t - t_d + d)\sec\theta_p$, we get two roots for the delta function for each laboratory time t_i, where the curve intersects the hyperbolas:

$$t_i = \frac{-(t_d - d)\sec^2\theta_p \mp \sqrt{(1 - \sec^2\theta_p)\tau_i^2 + (t_d - d)^2\sec^2\theta_p}}{1 - \sec^2\theta_p}. \tag{4.43}$$

The photon rate is computed as

$$\frac{dN}{dt_d} = \int_{t_a}^{t_b} dt\ (f_1 + f_2) \tag{4.44}$$

integrated along our curve $z(t)$. If we plug in $z = (t - t_d + d)\sec\theta_p$ into the photon rate model (4.39), we can simplify the expression a bit since

$$(1 - \cos\theta_p \cdot \beta)t = \left(1 - \cos\theta_p \cdot \frac{(t - t_d + d)\sec\theta_p}{t}\right) t = t_d - d, \tag{4.45}$$

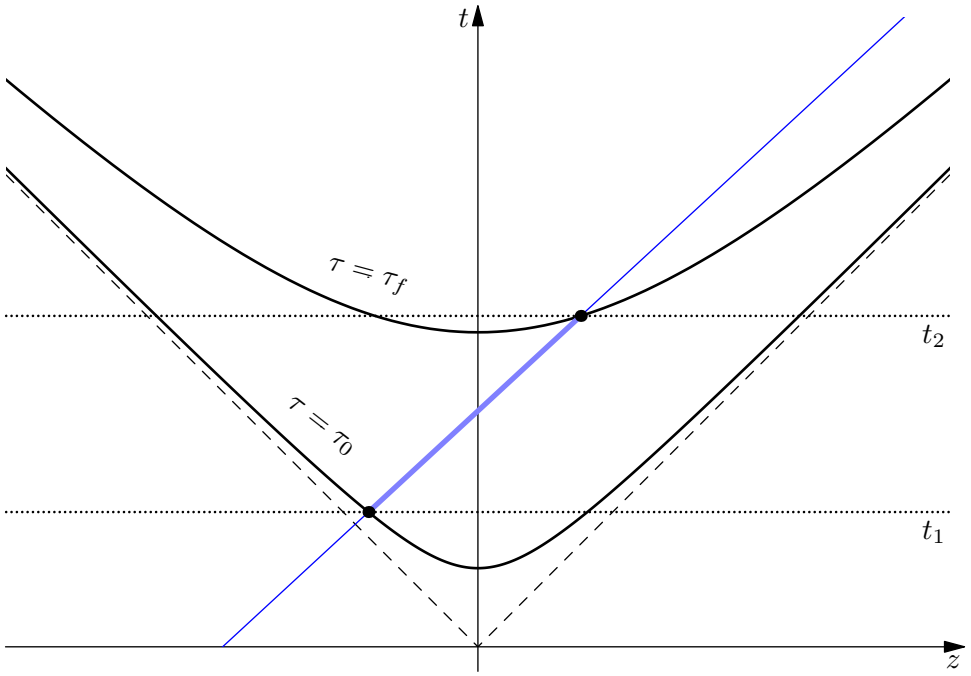

Figure 4.8: The intersections of the curve $\mathbf{z}(t)$ with the two equal proper-time hyperbolas.

so that

$$f_i = A_i \exp\left[-(t_d - d)\cdot B_i - (t/\gamma - \tau_i)^2 \cdot C_i\right]. \tag{4.46}$$

Folding the photon rate integral with the delta functions

$$\begin{aligned}\frac{dN}{dt_d} = \int_{t_a}^{t_b} dt \sum_{i=1}^{2} A_i \exp\left[-(t_d - d)\cdot B_i - (t/\gamma - \tau_i)^2 \cdot C_i\right] \\ \times\, \delta(t^2 - \tau_i^2 - z^2)\end{aligned} \tag{4.47}$$

will eliminate the term with c_i as $\tau = t/\gamma$ will be evaluated at τ_i. What remains is an exponential function in terms of the detector time t_d as well as the denominators from the evaluation of the delta functions:

$$\delta(t^2 - \tau_i^2 - z^2) = \sum_j \frac{\delta(t - t_j)}{|\frac{d}{dt}(t^2 - \tau_i^2 - z^2)|_{t=t_j}|}. \tag{4.48}$$

The derivative of the argument of the delta function at the intersection times t_i is

$$\frac{d}{dt}(t^2 - \tau_i^2 - z^2)\Big|_{t=t_j} = \mp\sqrt{\tau_i^2(1 - \sec^2\theta_p) + (t_d - d)^2 \sec^2\theta_p}, \tag{4.49}$$

where the minus-plus sign in front of the square root vanishes due to the modulus in Eq. (4.48). Since this term appears in a denominator, we can already see that the final photon rate will have poles at

$$t_d = d \pm \tau_i \sin\theta_p. \tag{4.50}$$

The final result reads

$$\frac{dN}{dt_d} = \sum_{i=1}^{2} \frac{a_i \exp[-(t_d - d)\cdot b_i]}{\sqrt{\tau_i^2(1-\sec^2\theta_p) + (t_d-d)^2\sec^2\theta_p}} \times \Theta(t_d - t_1)\Theta(t_2 - t_d)\cdot\Theta(t_d - \tau_i \sin\theta_p - d). \tag{4.51}$$

We have introduced three theta functions. The first two arise from the integration boundaries, while the last one is helpful for plotting the function, as it delivers cut-offs near the poles. A plot of the function can be seen in Fig. 4.9. To compare the full treatment of the toy model sans the delta-like

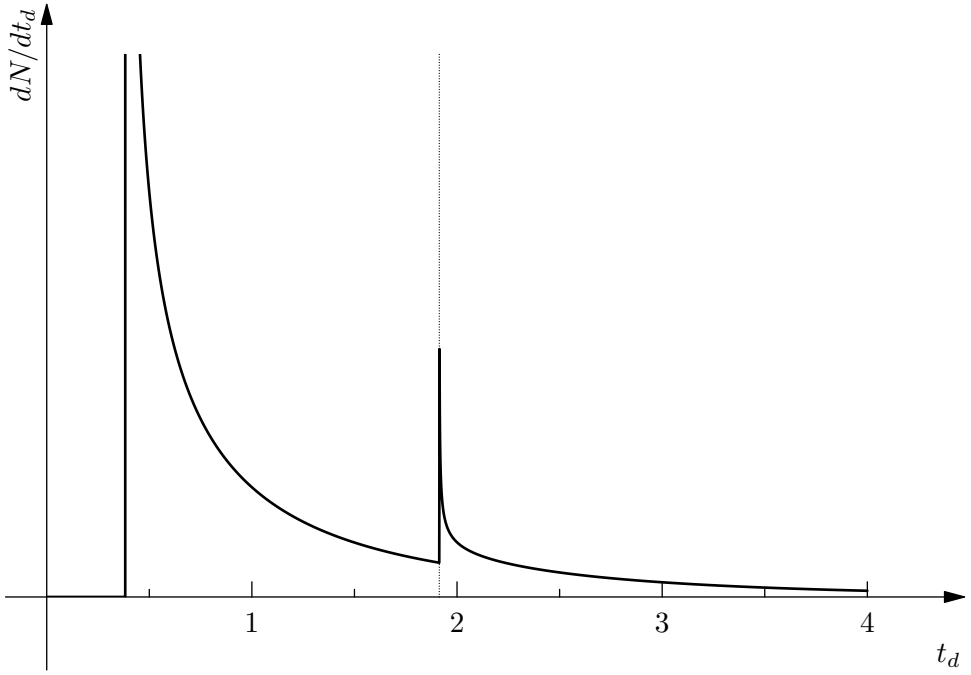

Figure 4.9: Plot of the photon rate according to our toy model. The peaks correspond to the poles of Eq. (4.51) and represent the detector time $t_d = d \pm \tau_i \sin\theta_p$ at which the integration curve touches the hyperbola at τ_i. Parameters are $A_1 = 5$, $B_1 = 0.5$, $\tau_1 = 1$, $A_2 = 3$, $B_2 = 1$, $\tau_2 = 5$, $\theta_p = \pi/8$, $d = 0$.

restriction (4.42), a numerically integrated photon rate dN/dt_d was plotted aside with the analytic result in Fig. 4.10. We also check whether the analytic treatment is applicable in any form if we employ the Martinez-Strickland (MS) model from Eqs. (2.9) and Eqs. (2.10) to a one-dimensional plasma wire. Figure 4.10 shows the three photon signals. The maxima of both analytic result and numerical integration of the toy model practically coincide. There is also a certain overlap of the numerical result for the full MS model. Although the shape of the pulse can not be reproduced buy the toy model, a qualitative statement can be made about the location of the second peak in the limit of high impact parameters.

4.3.1. Conclusions from the toy model

The models for the time evolution of the photon rate only allow for numerical solutions for the shape of the photon pulse at the detector. A first step of a simplification is to model the photon production rate by two Gaussians, employed in a rapidity-invariant manner. An additional factor takes care of the relativistic Doppler shift. Even this simplification does not allow yet to compute a photon

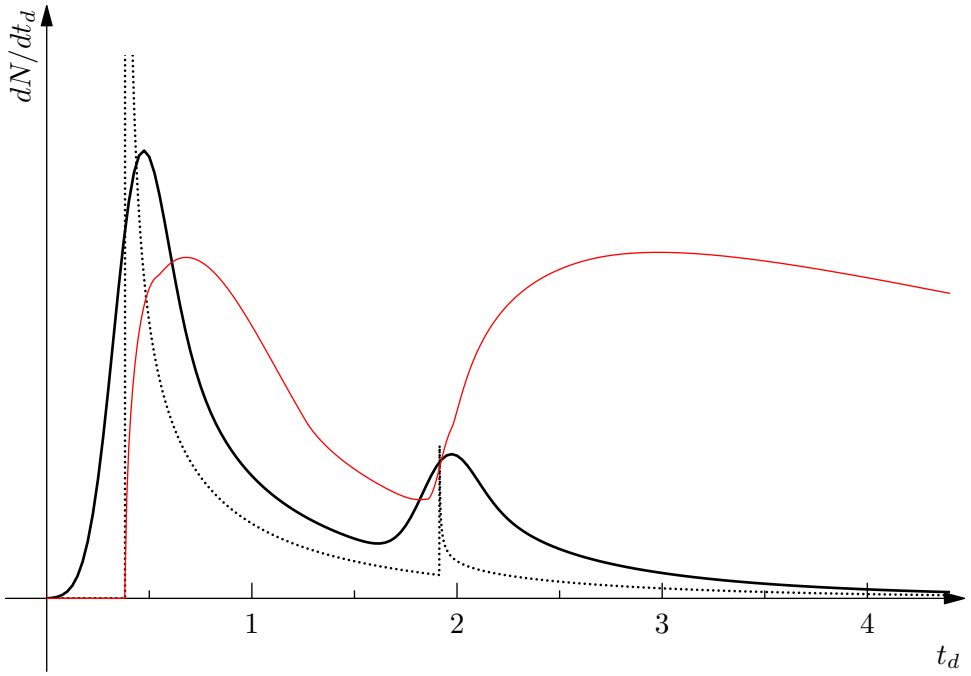

Figure 4.10: Numerical integration of the photon rate with the same parameters (solid, black) as in Fig. 4.9 (dotted) but slightly different axis scaling. The location of the maxima basically coincide. The red line represents a numerical photon rate calculation for the plasma wire employing the Martinez-Strickland model in Eqs. (2.9) and (2.10). It has been scaled to fit the plot, and following model parameters have been used: $\gamma = 20$, $\omega_d = 3\,\mathrm{GeV}$, $\tau_0 = 1\,\mathrm{fm}/c$, $\tau_{\mathrm{iso}} = 5\,\mathrm{fm}/c$, $\gamma = 2$, $\delta = 2$.

signal by purely analytic means. By restricting the photon rate in the Minkowski diagram to delta-like structures allows to perform the integration in a trivial manner and then to roughly predict the location of the two peaks, as seen in Fig. 4.10.

It is important to comprehend that the analytic expression in Eq. (4.51) is dominated by the geometrical aspect of the integration curve passing through the Minkowski diagram and intersecting the hyperbolas at certain times.

4.4. Three-dimensional model

4.4.1. Numerical integration

We use *Mathematica* for the numerical evaluation of Eq. (4.28). Again, there are a few possibilities on how to perform the computation of the integral. *Mathematica* offers various integration strategies and rules, each with their respective strengths.

One possibility is to use a multi-dimensional Monte Carlo integration. This will most likely always perform faster than a successive integration of x_p, y_p, and t using a global adaptive strategy. Monte Carlo integrations, however, may need either multiple runs or a much denser sampling to get stable results free of numerical artifacts. This, in turn, can diminish or completely eliminate the advantage of a faster performance.

The computation time is also highly dependent on some of the parameters, such as the impact parameter b or the photon emission angle θ_p and different integration strategies seem to work better

than others at different centralities. Using *Mathematica's* built-in parallel computation tools, the computation times could be sped up significantly by making use of multi-core processors.

In the following sections, the parameters below are used [49], unless specified otherwise:

- radius of the lead nucleus $R = 7.1\,\mathrm{fm}$
- initial temperature (hard momentum scale) $T_0 = 845\,\mathrm{MeV}$
- plasma freezeout temperature $T_c = 160\,\mathrm{MeV}$
- plasma formation time $\tau_0 = 0.088\,\mathrm{fm}/c$
- free streaming expansion $\delta = 2$ with $\gamma = 2$.

These parameters correspond to values expected for Pb-Pb collisions ($\sqrt{s_{\mathrm{NN}}} = 5500\,\mathrm{GeV}$) at the LHC [49]. The detector distance d is set to zero, but its position is assumed to be at some $z > 0$, therefore establishing the correct Lorentz transformations and the Doppler shift, as seen in Fig. 4.1. A finite, positive value for d would only produce a shift of the photon signal with respect to t_d.

4.4.2. Photon signal at mid-rapidity

We study the photon signal if the detector is placed at mid-rapidity, which amounts to a photon emission angle of $\theta_p = \pi/2$. Since there is a lesser dependence of the differential photon rate on ξ at mid-rapidity, there will be no significant effect of the anisotropy on the time evolved quantities and the shape of the photon pulse.

For purely illustrational purposes, the following contour plots will depict a one-dimensional scenario, as was introduced in Section 4.3. In these figures, the full model has been implemented, but the spatial extent of the plasma has been reduced to a one-dimensional wire.

Figures 4.6 and 4.8 already show how the curve $\mathbf{z}(t)$ is embedded in the Minkowski diagram for a certain value of t_d and θ_p. The diagrams can be used to literally read off what happens during the computation of the integral. For every detector time t_d, the curve is shifted in the diagram. Each of these positions represent an integration over the QGP along the curve, which is indicated in Fig. 4.6 and Fig. 4.8 by the slightly thicker line within the two hyperbolas that represent the lifetime of the plasma. This integration is the accumulation of all direct photon contributions throughout the plasma that arrive at the detector at a specific laboratory time t_d. With increasing t_d, the curve shifts more to the left (negative z) and we have to integrate over different regions of the plasma.

A contour plot in Fig. 4.11 shows the position of the curve in the Minkowski diagram. For $\theta_p = \pi/2$, the curve for the one-dimensional model lies parallel to the z axis. With increasing t_d, the curve shifts up towards positive t. Since the Doppler shift does not divide the Minkowski diagram into two parts in this case, the integration along the curve becomes very symmetric with respect to $z(t)$.

What can we expect for our detector signal dN? If we take Fig. 4.11 as a guide, we see that the curve $\mathbf{z}(t)$ starts at the very bottom of the Minkowski diagram at $t_d = 0$. At some later t_d, the curve passes the formation time τ_0 and we will begin to see a rise in the signal. Right after τ_0, the differential photon rates are the highest for a given frequency ω_d, as indicated by the green area. If we increase t_d further, the cooling of the plasma will reduce the differential photon rates. This is counteracted by the growing spatial extent of the plasma - which manifests itself in the light cone. While the differential photon rates decrease for larger t, the spatial extent increases and the integrated contributions from the whole plasma lead to a rising signal. Eventually, the plasma will cool off by such an amount that

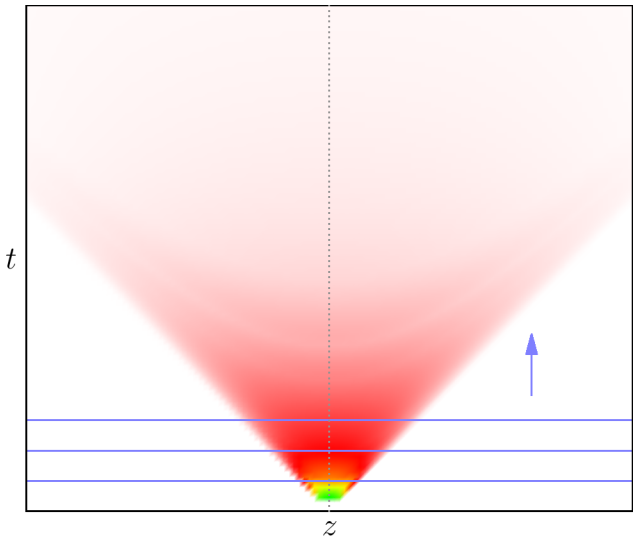

Figure 4.11: Schematic contour plot of the differential photon rate embedded in the Minkowski diagram. The vertical blue lines represent the curve $\mathbf{z}(t)$ at different, equally spaced $t_d > 0$. The upwards pointing arrow indicates the direction in which the curve shifts with increasing t_d.

the increasing spatial extent will not be enough to recover the same signal strength at the detector, leading to a decrease in the photon signal until it finally vanishes.

The explanation above and the picture presented in Fig. 4.11 have to be slightly adapted for the full three-dimensional situation. As the plasma has a finite transverse size, we will already have volume elements in the plasma that emit photons at $\tau = \tau_0$ which are away from the origin, $x \neq 0$. A photon registered at $t_d = 0$ was sent away at $(x, y, z) = (0, 0, 0)$ and arrives at laboratory time t at a detector placed at $z = d$. Hence, the photon signal at the detector will not begin at $t_d = 0$, but rather at some negative t_d. One could shift the detector time to account for this effect, but the earlier convention will be kept in order to be in accordance with Ref. [28].

First, we will take a look at how the photon signal for central collisions changes with different isotropization times. Fig. 4.12 shows the rather symmetric pulses for three different values of τ_{iso}. A remarkable phenomenon to be seen in Fig. 4.12 is the amplitude of the pulses. One would naively expect higher isotropization times to yield a lower amplitude photon signal, as the anisotropy suppresses the differential photon rate. The root of this apparent discrepancy is the time dependence of the temperature. As was shown in Fig. 2.5, different isotropization times cause a different temperature at $\tau = \tau_0$, as well as slower cooling and longer sustained initial temperature for larger τ_{iso}. For $\theta_p = \pi/2$, the suppression of the photon rate over time has a similar form as in Fig. 3.11, but the photon rate only decreases by about one order of magnitude for $\tau_{\text{iso}} \approx 10\tau_0$. Hence, the main effect driven by the isotropization time for this case is the modified temperature evolution, which results in a higher differential photon rate for a fixed photon energy ω_d.

The next quantity to investigate is the impact parameter b. It defines the transverse extent of the plasma and should have a similar influence on the pulses as in Fig. 4.12. Lower b equals a larger plasma volume, so the amplitudes of the photon pulses should be larger. Fig. 4.13 shows the pulses for three different b. The differences in the pulse length are also understood using the argument presented earlier: photons from volume elements around the near edge of the plasma arrive earlier than photon emitted from the center at the origin of our laboratory coordinate system. For a plasma with smaller

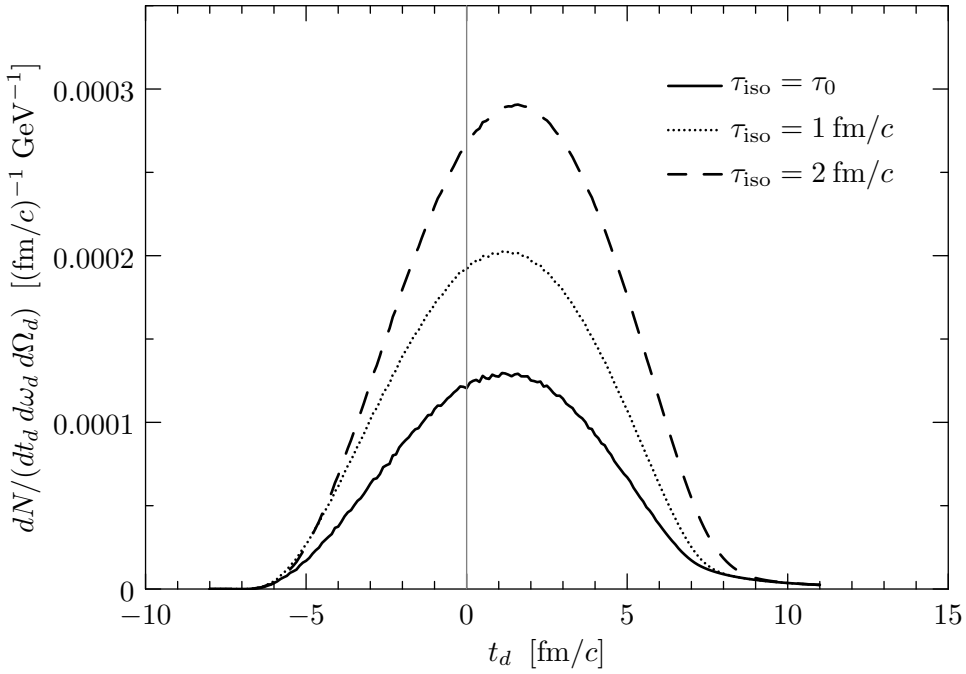

Figure 4.12: Photon pulses at midrapidity for different isotropization times. The dominating effect in these particular plot is the temperature evolution which is strongly dependent on the chosen value for the isotropization time. As seen in Fig. 2.5, larger $\tau_{\rm iso}$ result in an elongated plateau in the temperature evolution, which in turn increases the total photon yield. $\omega_d = 2\,\text{GeV}$, $\gamma = 2$, $\delta = 2$, $b = 0\,\text{fm}$, $\theta_p = \pi/2$.

transverse size, the time difference between these two photons is less and so is the shift in detector time t_d at which the photon pulse starts. It was mentioned in Subsection 4.2.3 that non-central collisions will have a lower temperature at the center, which in turn causes a faster freezeout. The time it takes for the plasma to reach the freezeout temperature is the main contributing factor to the pulse length. To demonstrate this effect, we plot two pulses with the same impact parameter $b = 10\,\text{fm}$ in Fig. 4.14 - one pulse being calculated with twice the initial temperature T_0. One can see a more pronounced tail for larger t_d towards the end of the pulse. This tail is only notably visible if the freezeout of the plasma takes longer than a photon from the far end of the plasma to catch up with the photons from the near side (with respect to the detector placement). Should the freezeout happen faster, the length of the pulse will be entirely governed by the impact parameter.

It becomes evident that the internal dynamics of the QGP determine the shape of the photon pulses. Already at $\theta_p = \pi/2$, we can see how the momentum-space anisotropies and their time evolution play a vital role.

4.4.3. Photon signal away from midrapidity

In this section, we focus on photon signals at smaller emission angles θ_p. By positioning the detector more in forward direction, the differential photon rates will exhibit a distinguished minimum induced by the anisotropy build-up, similar to Fig. 4.7.

Taking a look at a photon pulse generated with the same model parameters (Fig. 4.15), we unfortunately just see a shape similar to Fig. 4.14. Despite using a large value for the isotropization time, we do not see any hints of a two-pulse structure as expected from the toy model (Fig. 4.10).

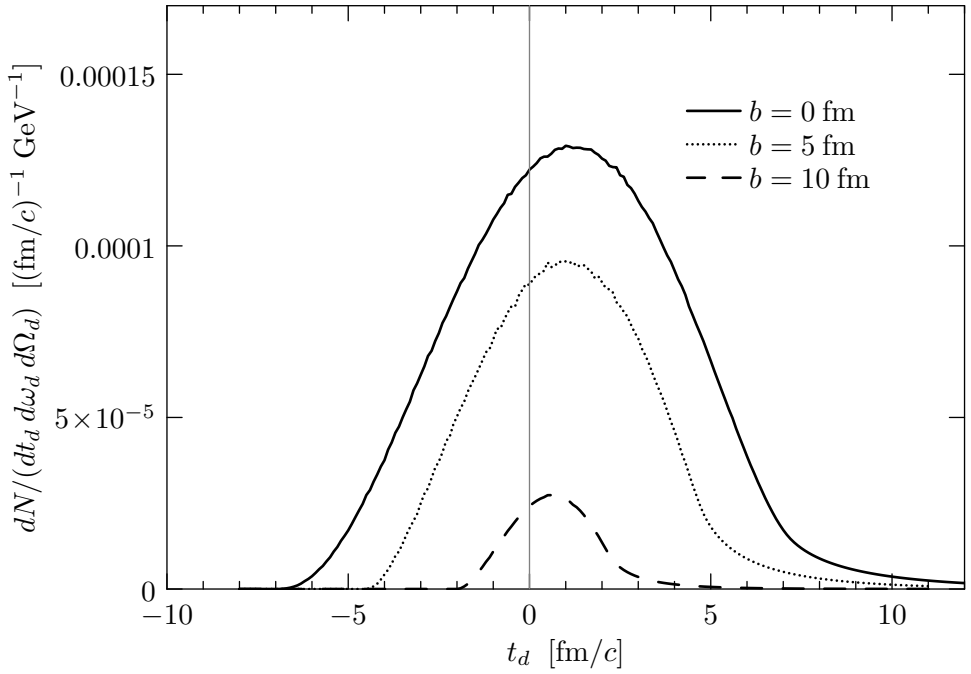

Figure 4.13: Same as Fig. 4.12 for various impact parameters b, but same isotropization time $\tau_{\rm iso} = \tau_0$. For smaller b, the plasma volume increases. This results in a larger total photon yield and hence a photon pulse with larger amplitude. The pulses are not centered at $t_d = 0$ due to an asymmetry in the time evolution of the QGP. The plasma is born sharply at a formation time τ_0, but is basically of infinite extent considering the rapidity invariance.

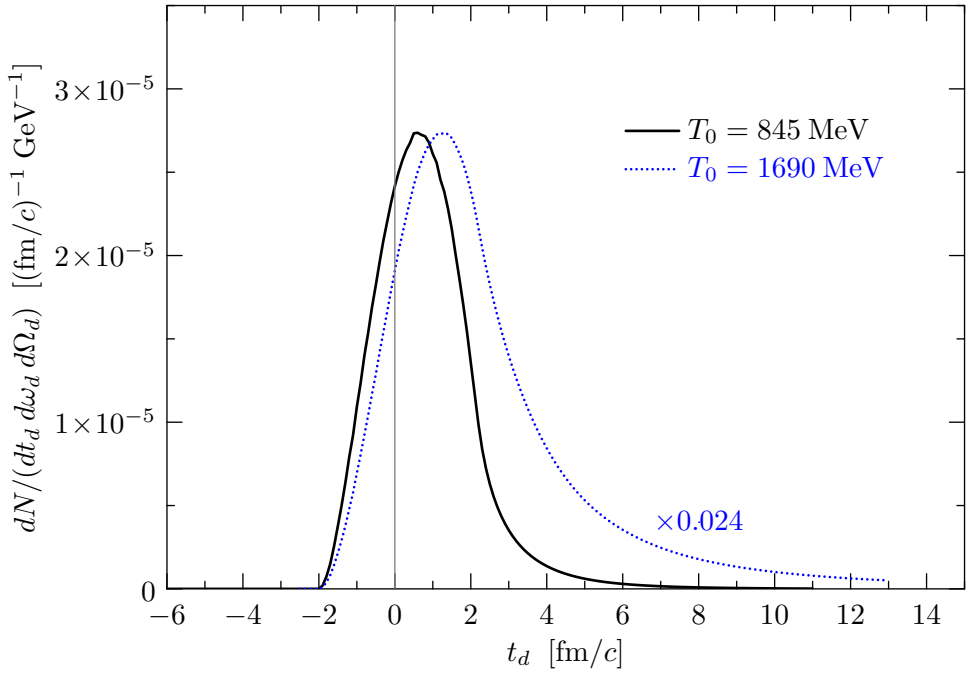

Figure 4.14: Enlarged view of Fig. 4.13 with $b = 10$ fm. The second photon pulse with $T_0 = 1690$ MeV has been normalized to the other one with by a factor of ≈ 0.024. This plot demonstrates that the tail at the end of the pulse is a characteristic that arises from the plasma lifetime. $\omega_d = 2$ GeV, $\gamma = 2$, $\delta = 2$, $b = 10$ fm, $\tau_{\rm iso} = \tau_0$.

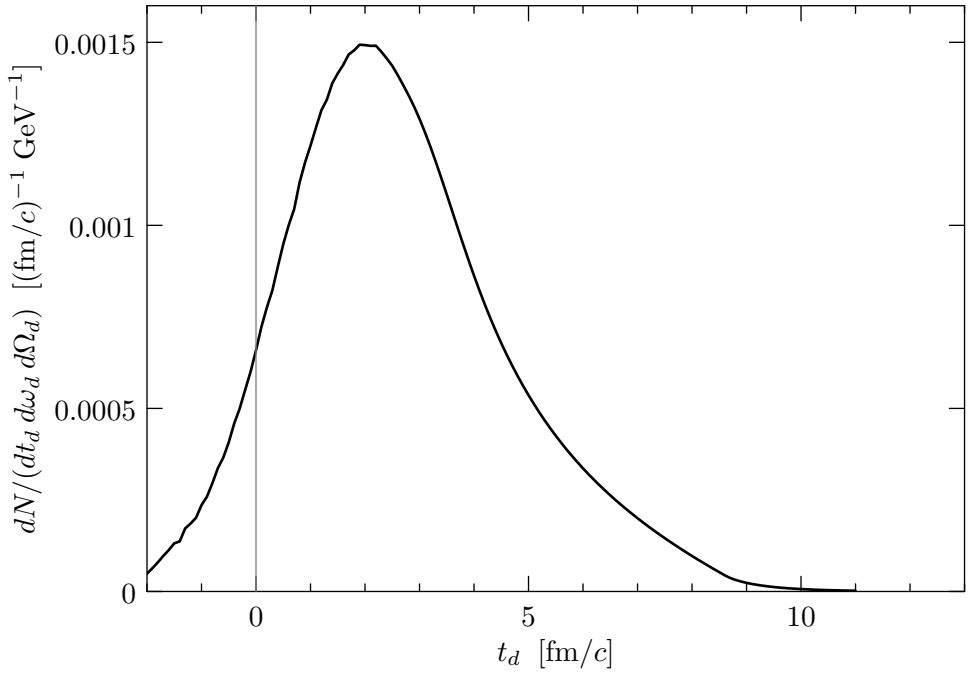

Figure 4.15: Photon pulse at $\theta_p = \pi/8$ and zero impact parameter b. The double peak features we expect via the arguments from the toy model do not appear. This is a result of the large size of the plasma which is responsible for washing out any structure in the pulse simply due to the time it takes a photon from the far end to travel through the QGP. $\omega_d = 2$ GeV and $\tau_{\text{iso}} = 2$ fm/c.

The reason we do not see any notable effect from the time-dependent photon rate suppression is the transverse size, which at $b = 0$ fm is maximal. At emission angles $\theta_p < \pi/2$, photons from the far end of the plasma travel longer distances through the QGP compared to the case at midrapidity. Reformulated in terms of our integration along the curve $\mathbf{z}(t)$, this means that we sum over many more photon emitting volume elements per detector time t_d. Such an integration over a larger region in space-time leads to a greater overlap of photons from different stages of the QGP evolution. With larger transverse sizes, this overlap eventually hides the desired effect from the anisotropy buildup.

Fig. 4.16 shows the photon production rates in the Minkowski diagram for a detector in forward position at $\theta_p = \pi/4$. The two maxima can be seen as the green and yellow spots, separated by the minimum caused by the anisotropy buildup. This figure is again a representation of the strictly one-dimensional plasma or the limit of $b \approx 2R$.

If we were to drop the constraint of having an infinitely thin plasma wire, the z-component of the curve $\mathbf{z}(t)$ is tilted differently in the Minkowski diagram (Fig. 4.17), according to Eq. (4.7).

In the plots above, the position of the curve was chosen to illustrate how a double pulse shape can occur in the first place. For a certain given photon energy ω_d and an emission angle $\theta_p < \pi/2$, the photon production rate in the Minkowski diagram shows two distinct peaks. These peaks are located near the formation time as well as shortly after isotropization of the plasma. Due to the blue-shift of photons originating from volume elements which move towards the detector, the second peak is to be found in the right half of the diagram (for $d > 0$). If the curve fits exactly into the minimum between the two peaks, as shown in Fig. 4.16, we will see a decline in the photon signal during the time t_d at which the curve passes through this suppression region. Demonstrated in Fig. 4.15, this effect can completely vanish, if the transverse extent of the plasma is too large. In the Minkowski

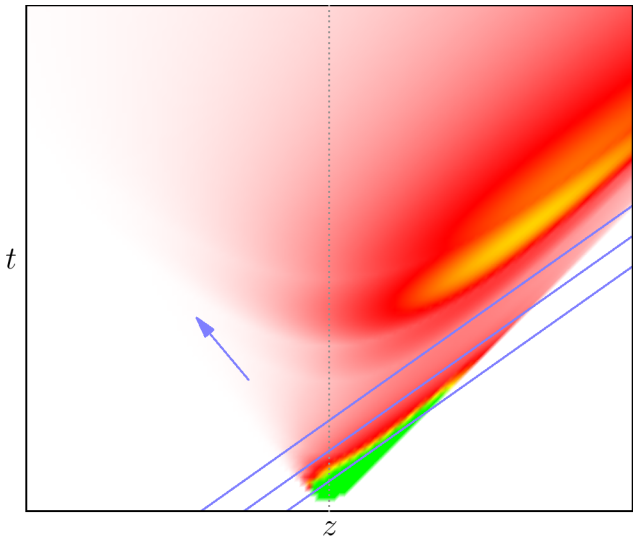

Figure 4.16: Photon production rate for $\theta_p = \pi/4$. The values have been scaled logarithmically to allow for a better separation and color coding of the peaks (yellow, green). Although the curves are separated by the same Δt_d as in Fig. 4.11, they lie closer to each other in the Minkowski diagram.

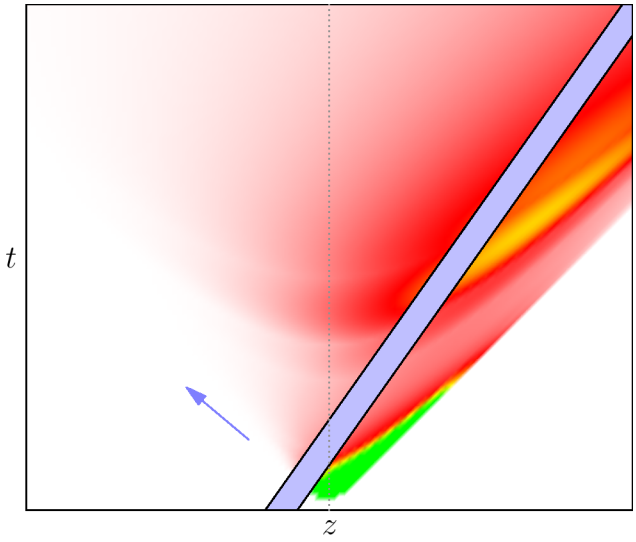

Figure 4.17: Photon production rate for $\theta_p = \pi/4$. The blue band indicates the z-component of the integration area spanned up by the curve for some finite b.

diagram, integration over the shift x_p corresponds to additional shifts of the curve, turning the line of integration essentially into a band. Should these shifts for a certain value for t_d, in which the curve lies in this minimum (Fig. 4.16), cause it to cross over to regions near the maxima, the phenomenon of suppression will be diminished or vanishes entirely. It is therefore necessary to focus on collisions with larger impact parameters in order to observe double pulses.

By reducing the transverse size of the plasma, the wanted effect from the photon rate suppression becomes finally visible, as shown in Fig. 4.18.

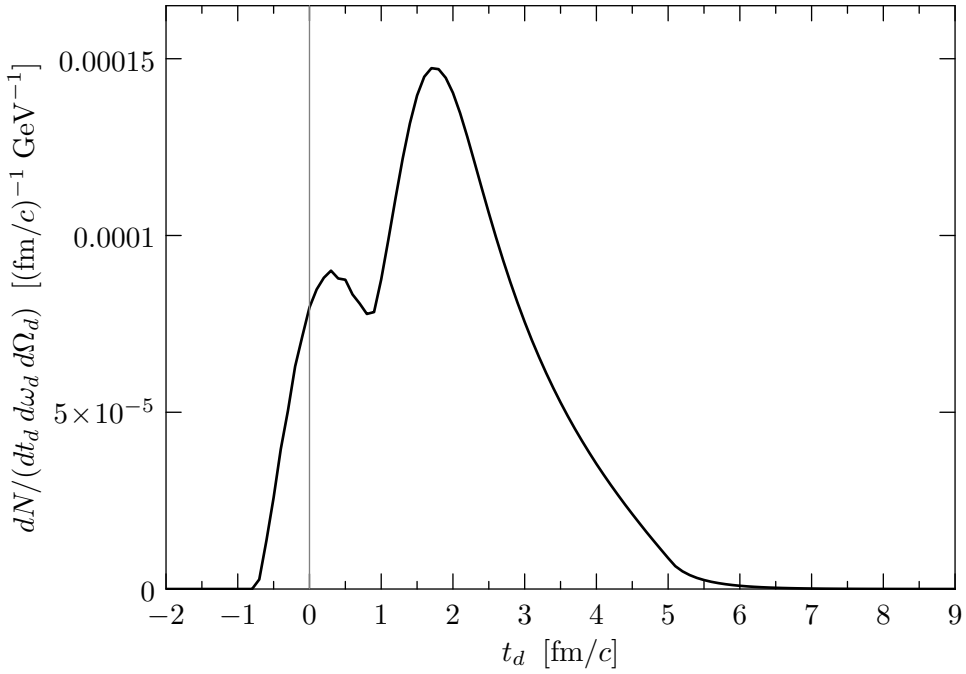

Figure 4.18: The photon pulse detected in forward direction. Due to the small transverse size of the plasma, the integration band as depicted in Fig. 4.17 is thin enough to allow for a visible minimum in the photon signal, as the curve $\mathbf{z}(t)$ passes through the minimum in the photon rate, caused by the anisotropy. $\theta_p = \pi/8$, $\omega_d = 3\,\mathrm{GeV}$, $\gamma = 2$, $\delta = 2$, $b = 10\,\mathrm{fm}$, $\tau_{\mathrm{iso}} = 2\,\mathrm{fm}/c$.

4.5. Pulse shapes

We have established the phenomenological mechanisms that give rise to a double peak structure in the photon signal. The requirements to create such a signal from an anisotropic quark-gluon plasma are summarized below:

1. a photon emission angle closer to the forward direction to get a larger effect from the photon rate suppression due to the anisotropy buildup,
2. a comparably large isotropization time τ_{iso}, which ensures that the two maxima in the differential photon rate are separated, allowing for an extended minimum in between,
3. non-central collisions to lessen the amount of overlaps due to the shift of the curve $\mathbf{z}(t)$.

These points have been demonstrated in the preceding sections in a qualitative way. Still, the question on the actual values of the parameters remain. At which isotropization times do we still see a double peak structure? How small does the emission angle have to be and at which energies does the peak doublet vanish, if at all?

The parameters used in the models $(\tau_0, \tau_{\mathrm{iso}}, T_0, T_c, \gamma, \delta, \theta_p, \omega_d, b)$ to calculate the photon signal determine the shape of the pulses. We should be able to read off several properties of the plasma by investigating the photon signal.

4.5.1. Pulses at intermediate emission angles

In this subsection, we will focus on parameters, at which the double peaks are more pronounced, such as a large impact parameter and a large isotropization time. As the limit of very large b corresponds to the one-dimensional plasma wire, we may use some of the ideas from Section 4.3. There, we have determined the detector times, at which the final signal had poles due to the delta-like nature of the photon rate as

$$t_d = d \pm \tau \sin\theta_p, \tag{4.52}$$

where τ belongs to the equal proper time hyperbola (4.42) at which the differential photon rate was non-zero. To use this result properly, we have to first remind ourselves that the photonrate does actually exhibit a minimum at $\tau = \tau_{\text{iso}}$ for $\gamma = 2$ rather than a maximum (see Figs. 2.6 and 2.7), as the anisotropy parameter is approximately maximal at this proper time. Marking this detector time in photon pulse plots at different angles actually matches this time with the minima between the two pulses very well (Fig. 4.19).

The most prominent feature in Fig. 4.19 is the varying height of the second pulse in relation to the first one. Considering the contour plots from earlier subsections, such as Fig. 4.7 or Fig. 4.16, we know that the second pulse originates from a region in the Minkowski diagram at later t. By lowering the emission angle, the Doppler shift enhances the photon production rate in the blue-shifted part of the diagram. The second peak is therefore higher in amplitude (compared to the first one), whereas the first peak, which originates from the low-t region of the diagram, is less affected by the Doppler shift.

Figure 4.20 shows the pulse shapes for the same parameters, except for an almost instantaneous isotropization $\tau_{\text{iso}} = \tau_0$.

4.5.2. Sharpness of the transition

Until now, we have been using a value of $\gamma = 2$, as was done in Ref. [28]. Already shown in Fig. 2.4 and Figs. 2.6 and 2.7, this parameter defines the sharpness of the transitions in the time evolution of the plasma.

Figure 4.21 shows the photon pulses at a large isotropization time with a much sharper transition ($\gamma = 20$).

The dashed, blue lines in Fig. 4.21 show the pulses at $\gamma = 2$, and allow for an easy comparison to the pulses at $\gamma = 20$. A larger value for γ leads to a higher maximum in the anisotropy parameter ξ (Fig. 2.7). This higher maximum seems to have just a negligible effect on the pulses, as the minima in the photon pulses are almost identical. Due to the sharper falloff of ξ, the photon rate suppression is reduced much faster and the pulse shows in a higher second peak that has shifted to smaller t_d.

4.5.3. Pulse shapes at various isotropization times

The next plots (Fig. 4.22) show the pulse shapes with varying isotropization times. While the pulses at $\tau_{\text{iso}} = 0.25\,\text{fm}/c$ bear no noticeable difference to the case at $\tau_{\text{iso}} = \tau_0$, one can notice how the second peak starts emerging at approximately $\tau_{\text{iso}} \approx 1\,\text{fm}/c$.

We were able to semi-quantitatively approximate the location of the minimum between the two peaks of a double pulse. This was possible because we know that τ_{iso} roughly corresponds to the maximum of the photon rate suppression at small γ.

Already in Fig. 4.19, one may see that the maximum of the second peak shifts forward with increasing θ_p at about the same rate as the minimum does. Such a trend suggests that the coarse approximation

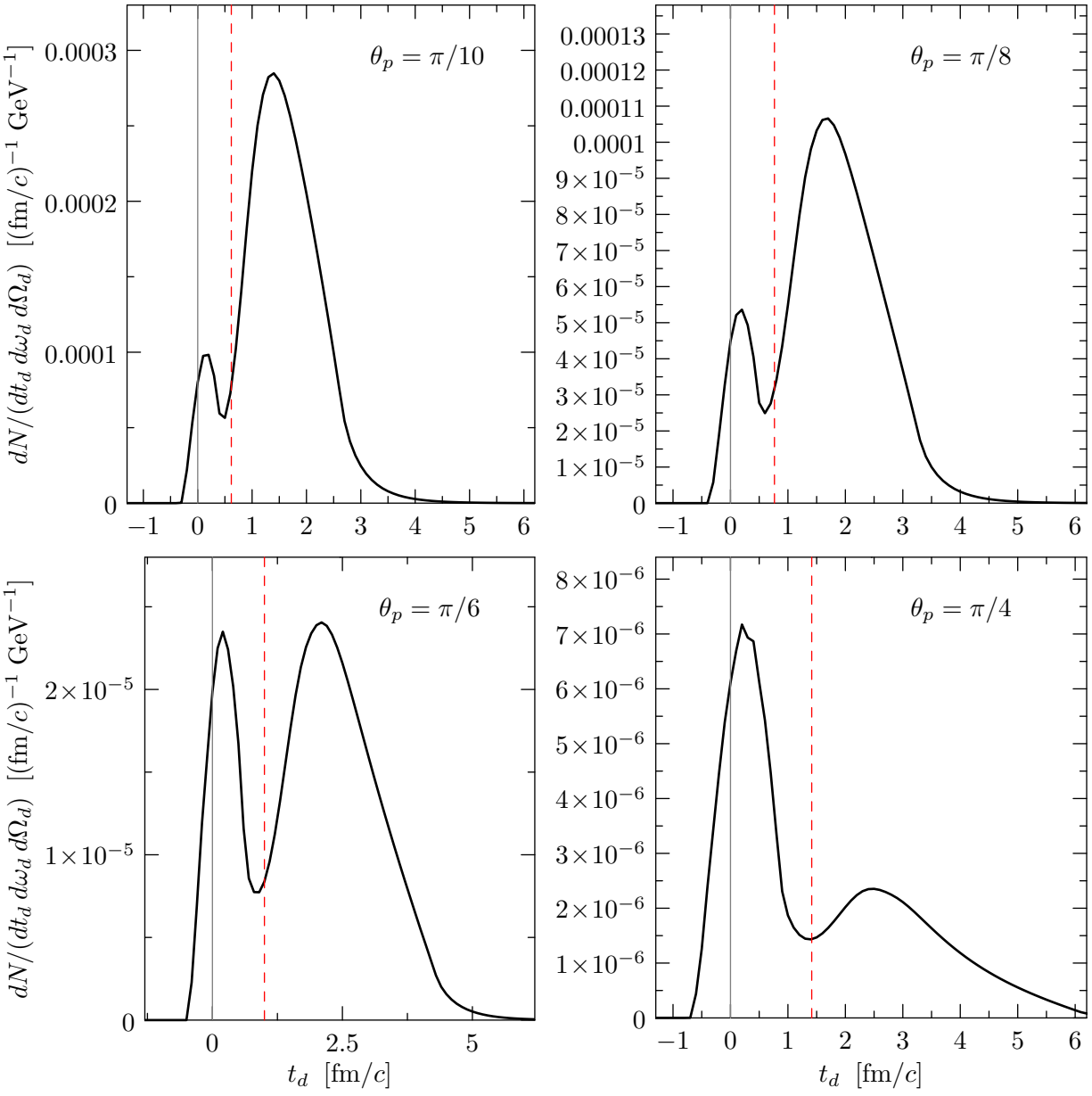

Figure 4.19: Photon pulses for various θ_p. The vertical red, dashed lines indicate detector times $t_d = \tau_{\text{iso}} \sin\theta_p$, which correspond to extended minima of the differential photon rates. This shows that in the limit of large b, we recover a scenario similar to the one-dimensional plasma wire where we can relate a distinct proper time (e.g. where the anisotropy becomes maximal) to a detector time.$\omega_d = 2\,\text{GeV}$, $\gamma = 2$, $\delta = 2$, $b = 10\,\text{fm}$, $\tau_{\text{iso}} = 2\,\text{fm}/c$.

via the one-dimensional model may be applicable if we can determine the proper time at which the photon rate suppression is lifted. We numerically calculate a value for τ which satisfies

$$\xi(\tau) = \xi_{\text{iso}}, \tag{4.53}$$

where ξ_{iso} indicates the return to isotropy. Per definition, ξ_{iso} is equal to 0 in the isotropic case, but this is only reached at asymptotically large times using the interpolating model. Therefore we need to choose a finite value for ξ_{iso}. Solving Eq. (4.53) for fixed τ_0, τ_{iso}, γ and δ would give a value for τ which is inserted into Eq. (4.50) from the analytic toy model. This would yield a detector time t_d

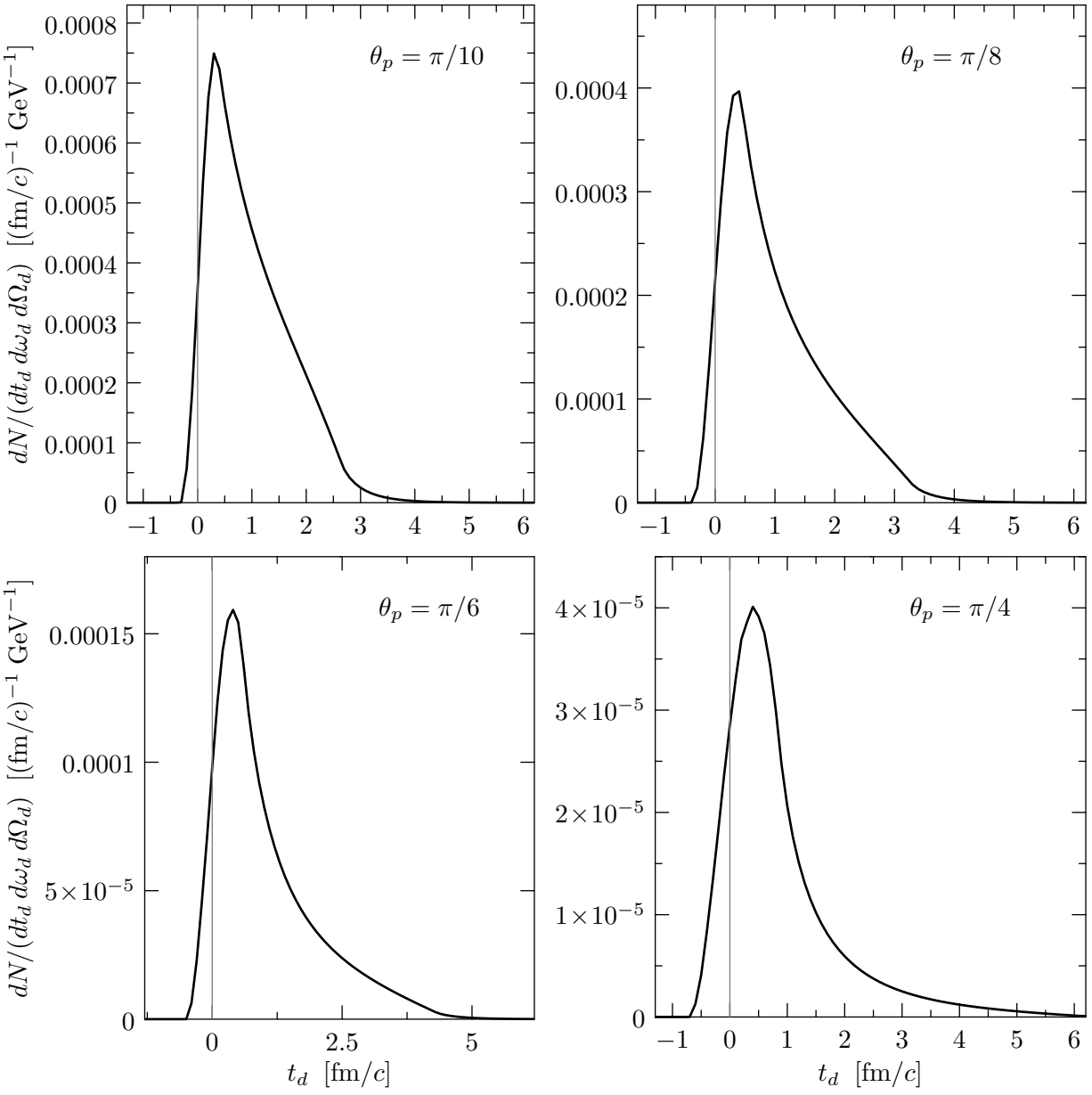

Figure 4.20: Same as Fig. 4.19, for $b = 12$fm and $\tau_{\rm iso} = \tau_0$. Due to the almost instantaneous isotropization of the plasma, there is no photon rate suppression that could manifest itself in a minimum in the photon signals.

that should reflect the isotropization of the plasma.

Unfortunately, this method does not reliably predict the location of the second maximum, since the choice of $\xi_{\rm iso}$ remains an almost arbitrary one. Due to the nature of the smeared step-function, small changes of this constant yield quite different results for $\tau > \tau_{\rm iso}$ when γ is of the order of 1. Nevertheless, the location of the second maximum can be read off (Fig. 4.22 and used in Eq. (4.50) to calculate a proper time at a known angle that can be regarded as the time at which the plasma becomes isotropic again. Indeed, for $t_d = 2\,\mathrm{fm}/c$ and $\theta_p = \pi/6$, $\tau = \tau_{\rm peak}$ equals $\approx 4\,\mathrm{fm}/c$. At this proper time, the anisotropy parameter has the value $\xi \approx 0.14$, which is sufficiently low compared to the maximum $\xi \approx 73$ at $\gamma = 2$ and hence the plasma can be regarded as approximately isotropic.

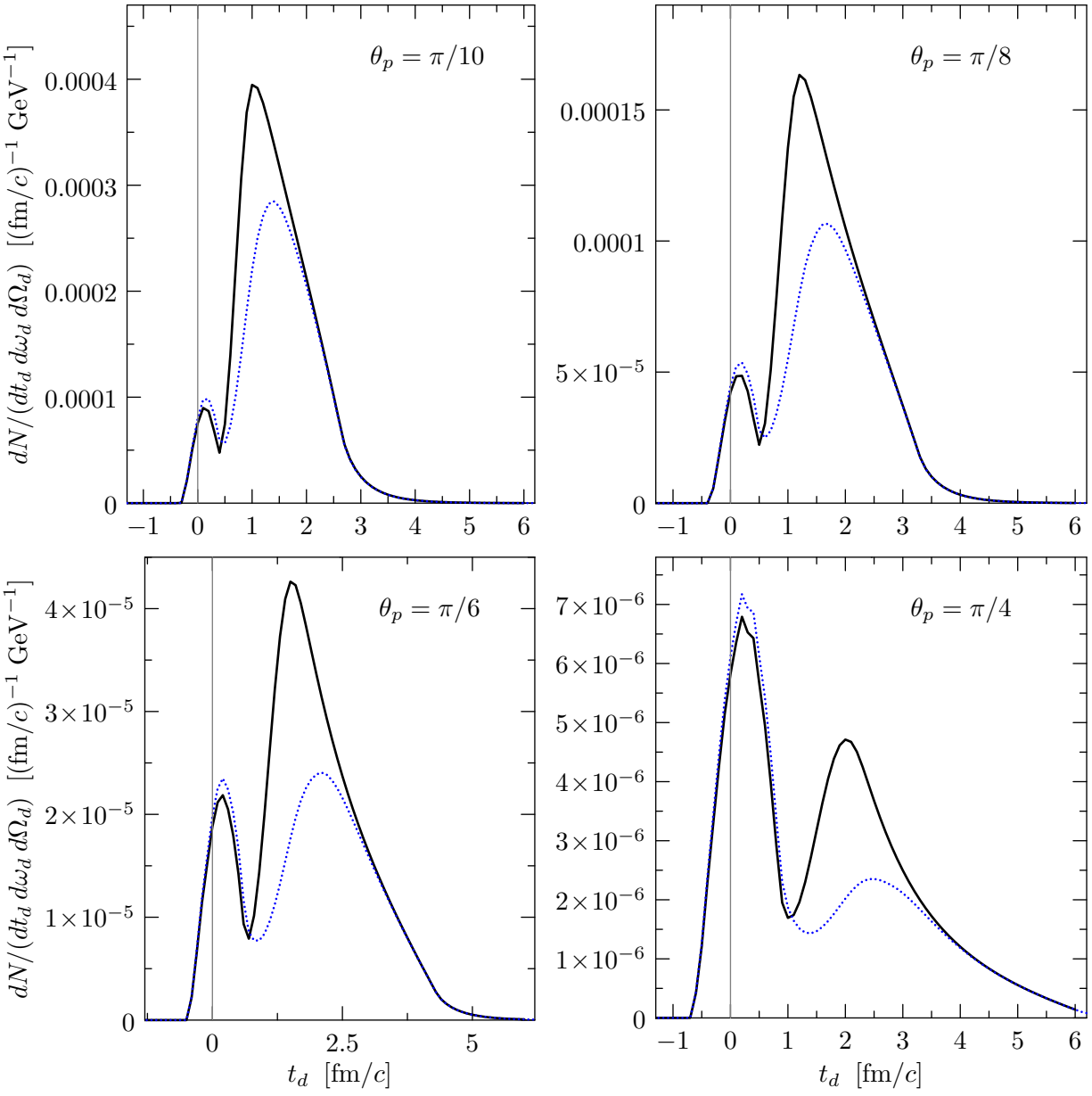

Figure 4.21: The black curves are photon pulses at $\gamma = 20$, the blue, dotted ones are the same curves as in Fig. 4.19 with $\gamma = 2$. $\omega_d = 2$ GeV, $\delta = 2$, $b = 12$ fm, $\tau_{\rm iso} = 2$ fm/c. The larger (sharper) transition parameter causes a faster isotropization of the plasma, which can be observed in the photon pulses by looking at the second peaks, which are higher in amplitude and slightly shifted to earlier detector times.

The ratio between $\tau_{\rm peak}$ and $\tau_{\rm iso}$

$$\frac{\tau_{\rm peak}}{\tau_{\rm iso}} = r_{\rm p/iso} \tag{4.54}$$

is obtained for the case $\tau_{\rm iso} = 2$ fm/c and then used to calculate new detector times t_d at different isotropization times via Eq. (4.50) with $\tau_{\rm peak} = r_{\rm p/iso} \cdot \tau_{\rm iso}$.

4.5.4. Energy dependence of photon pulses

According to Fig. 3.10 or Eq. (4.35) for the isotropic plasma, picking out a photon signal at higher energies will in general yield lower amplitudes.

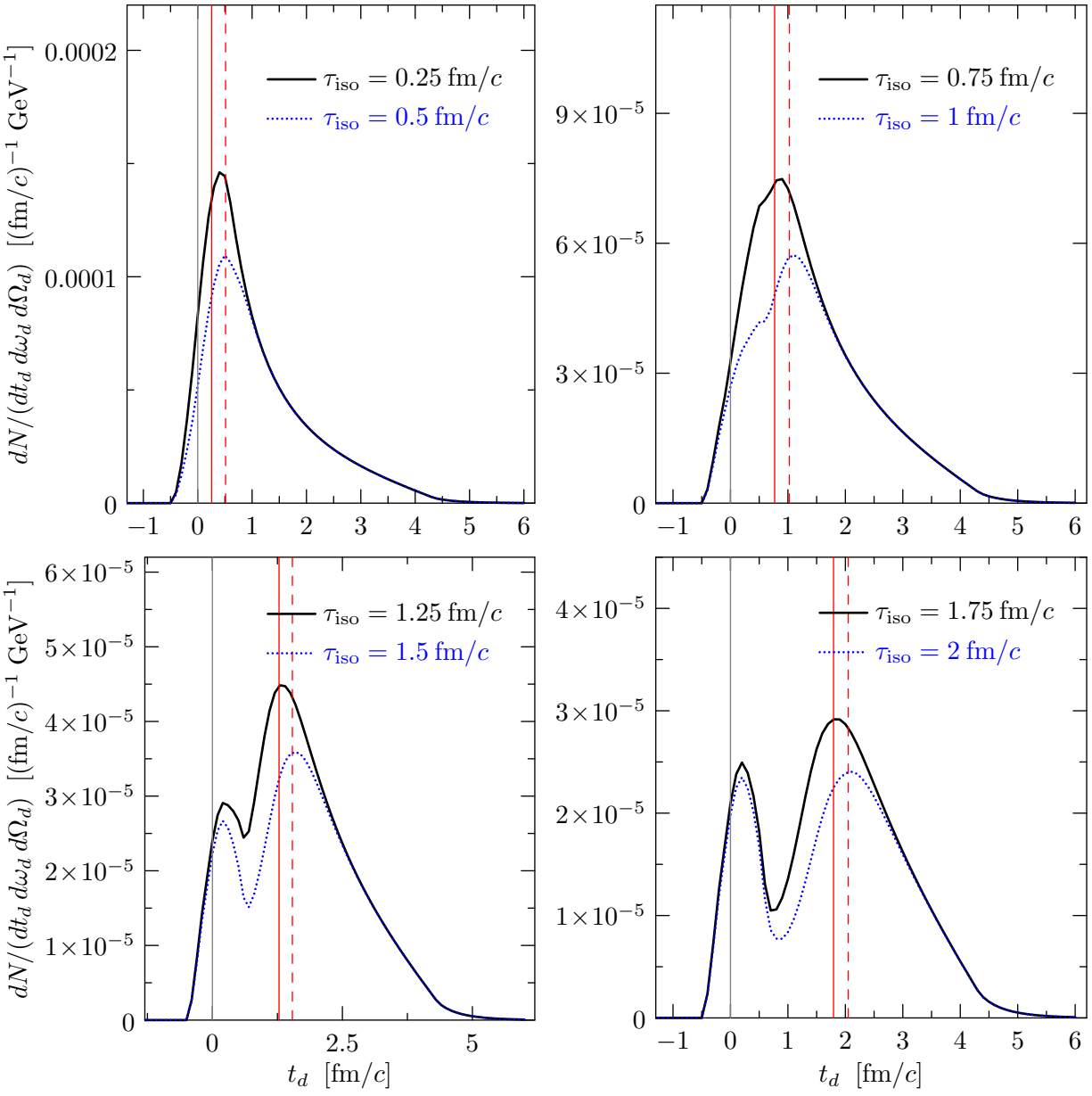

Figure 4.22: Photon pulses at various $\tau_{\rm iso}$. The vertical red, solid (dashed) lines indicate the semi-numerically approximated position of the second peak of the solid (dotted) photon pulse. $\omega_d = 2$ GeV, $\gamma = 2$, $\delta = 2$, $b = 12$ fm, $\theta_p = \pi/6$.

We see in Fig. 4.23 how the second peak of the double pulse structure becomes smaller with increasing energy, compared to the first peak. This can be explained in the following way: the photon production rate at a fixed emission angle and anisotropy parameter can be roughly written as

$$\omega_d \frac{dR}{d^3p} \sim e^{-\omega_d/T}, \tag{4.55}$$

where the temperature T has a $1/\tau$ behavior for large proper times. The first peak of the double pulse arises from the early ($\tau \approx \tau_0$) and central ($z \approx 0$) portions of the plasma. Increasing the detector energy ω_d leads to an exponential suppression according to Eq. (4.55). The second peak, however, arises from later stages ($\tau \approx \tau_{\rm iso}$) and some blue-shifted portions ($z > 0$) of the plasma (see Fig. 4.16).

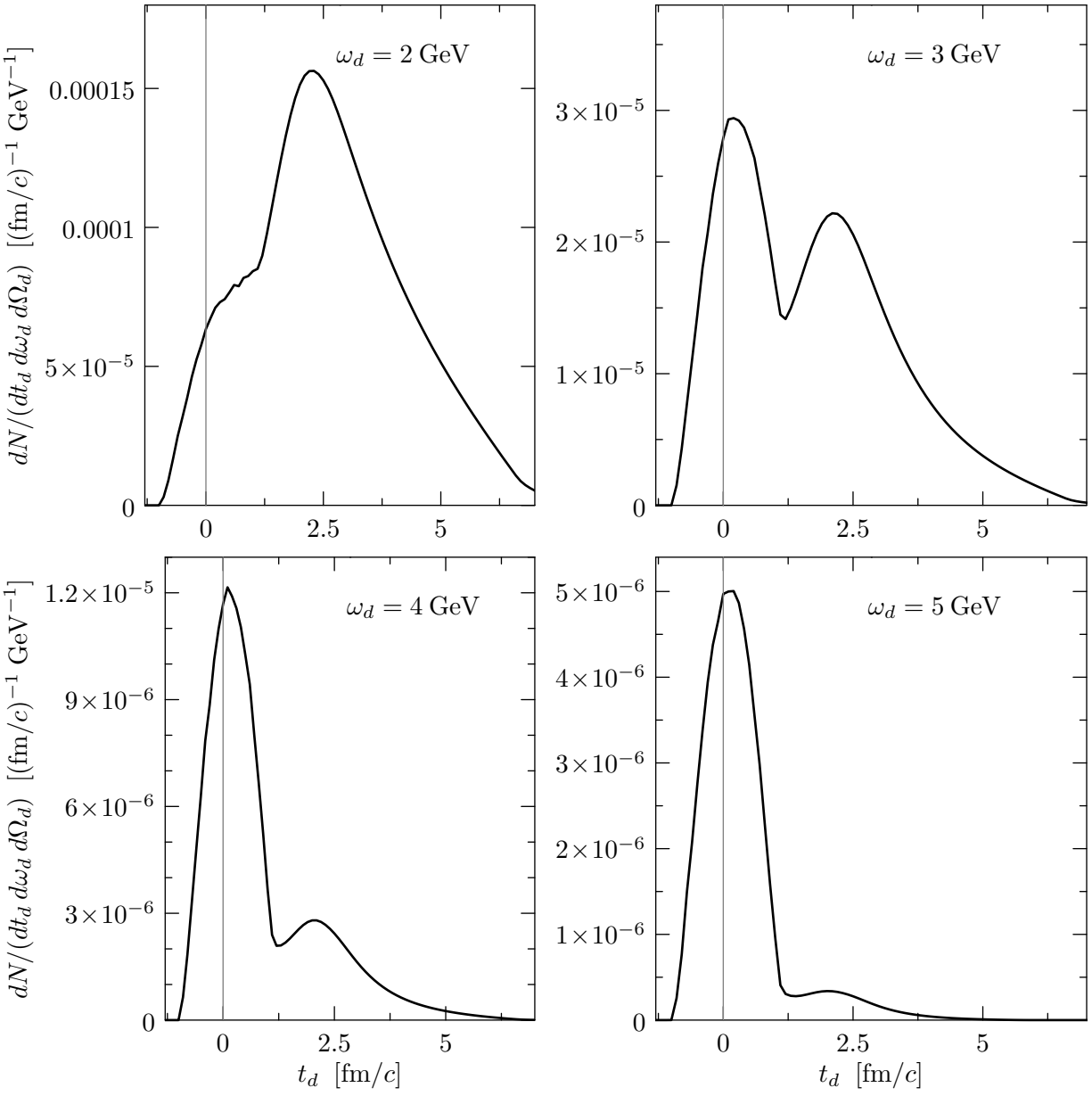

Figure 4.23: Photon pulses at different detector energies ω_d. As explained in the text, both peaks are suppressed exponentially with linearly increasing detector energy ω_d. Since the second peak arises from later stages of the plasma evolution, the suppression of this peak is even stronger as the first one, according to Eq. (4.56). $\gamma = 2$, $\delta = 2$, $b = 10$ fm, $\theta_p = \pi/6$, $\tau_{\rm iso} = 2$ fm/c.

At later times the differential photon rate is even stronger suppressed, since

$$e^{-\omega_d/T} \approx e^{-\omega_d \cdot \tau} \tag{4.56}$$

for $\tau \gg \tau_0$. Concluding, a linear increase in ω_d leads to an exponential suppression at small τ, but an even stronger exponential suppression for large τ. We check this explanation by considering the pulse heights of such a double pulse. The ratio of the second pulse height to the first pulse height should

show an exponential dependence on the detector energy ω_d. Ratios

$$\mathcal{R} = \frac{\text{height of second peak}}{\text{height of first peak}} \tag{4.57}$$

of a few pulses between $\omega_d = 2\,\text{GeV}$ and $\omega_d = 5\,\text{GeV}$ have been extracted and plotted in Fig. 4.24.

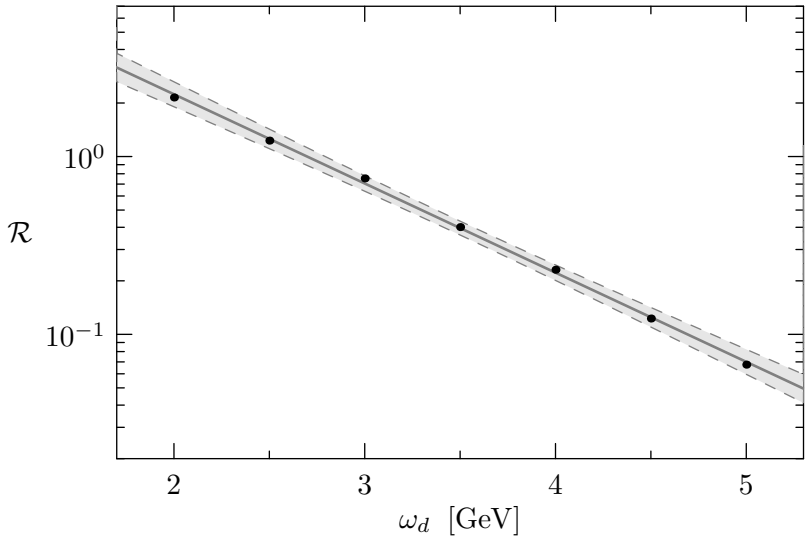

Figure 4.24: Pulse height ratios (dots) and a fit via a function $a + b\,e^{-c\,\omega_d}$ demonstrating their exponential dependence on the detector energy ω_d. The gray area represents the region between the mean prediction bands for a 99.7% confidence interval. Parameters are the same as in Fig. 4.23.

Conclusions

In this chapter, we have investigated the time dependent photon signals emitted from an anisotropic quark-gluon plasma. For a smooth transition ($\gamma = 2$), the evolution of the anisotropy parameter ξ has a maximum near τ_{iso}, which translates to a distinct minimum in the differential photon production rate. If we place an ideal photon detector far away from the plasma at an angle close to the beam axis, the suppression of the photon rate becomes manifest in the photon signal in form of a double-peak structure. To prevent this structure from being washed out due to the transverse spatial extent of the plasma, we focus mostly on peripheral collisions with large impact parameter b. The photon signals show a high sensitivity towards the model parameters, which would make them an ideal tool to explore the internal dynamics of the QGP. As of today, there exists no theoretically established method of measuring time-resolved structures in the order of yoctoseconds. A recently proposed idea for the characterization of pulses via streaking is applicable to sub-attosecond structures [80], which is still some orders of magnitude above the QGP signal length.

The next chapter will investigate, whether the mechanisms, which lead to these double pulse structures, still show up, if we consider time-integrated spectra. Such direct photon spectra have been already measured and will be measured in the near future in experimental facilities at the LHC and FAIR.

I painted the picture, and in the colors the rhythm of the music quivers. I painted the colors I saw.

– Edvard Munch

5 Spectra

5.1. Overview

Direct photon spectra in heavy-ion collisions have been successfully measured by the PHENIX experiment at RHIC [47] and the WA98 collaboration at CERN [81]. The ALICE experiment at CERN has already taken data and publications are expected in the near future. Both the PHOS detector at ALICE [82, 83] and the electromagnetic calorimeter at PHENIX are positioned at midrapidity, covering a pseudo-rapidity range of $-0.12 \leq \eta \leq +0.12$ and $-0.35 \leq \eta \leq +0.35$ respectively. The calorimeter at WA98, on the other hand, is positioned in forward direction ($2.3 \leq \eta \leq 3.0$) as well as the proposed detector in the CBM experiment at FAIR ($1.7 \leq \eta \leq 2.5$) [84]. Pseudo-rapidity η is a commonly used quantity in particle physics and is related to the polar angle θ via

$$\eta = -\ln\left[\tan\left(\frac{\theta}{2}\right)\right]. \tag{5.1}$$

The influence of momentum-space anisotropies on the QGP direct photon spectrum has been studied in Refs. [85–87]. Using an extended model including a mixed and a hydrodynamical phase, L. Bhattacharya and P. Roy matched their calculated spectra to the PHENIX data and found a good agreement for isotropization times between 0.5 fm/c and 1.5 fm/c.

Since these spectra were calculated for a detector placed at midrapidity ($\eta = 0$, $\theta = \pi/2$), the obvious question would be how these spectra behave at different detector positions.

5.2. Photon rate in proper-time and rapidity space

It was convenient to work in the standard (t, x, y, z)-coordinate system for the purpose of calculating and understanding photon pulses. In these coordinates, the curves $\mathbf{z}(t)$ are straight lines and their embedding in the Minkowski diagram is easy to visualize. A photon spectrum is the momentum or energy dependent accumulation of all photon emitting elements in the plasma. Practically, this is equivalent to integrating our photon pulses over all detector times t_d to get the total amount of photons for a certain detector energy ω_d. Calculating such photon signals for different ω_d and subsequently performing the integral $\int dt_d$ results in a direct photon spectrum. Equivalently, we can ignore the curve $\mathbf{z}(t)$ all together and sum over all photon emitting volume elements within the QGP volume, which is a faster and more efficient calculation. Conveniently, we switch to proper-time (τ) and rapidity (y)

coordinates:

$$t = \tau \cosh y, \tag{5.2a}$$
$$z = \tau \sinh y, \tag{5.2b}$$

and

$$dt\, dz = \tau d\tau\, dy. \tag{5.3}$$

Such a coordinate transformation compactifies the volume of the quark-gluon plasma (Fig. 5.1).

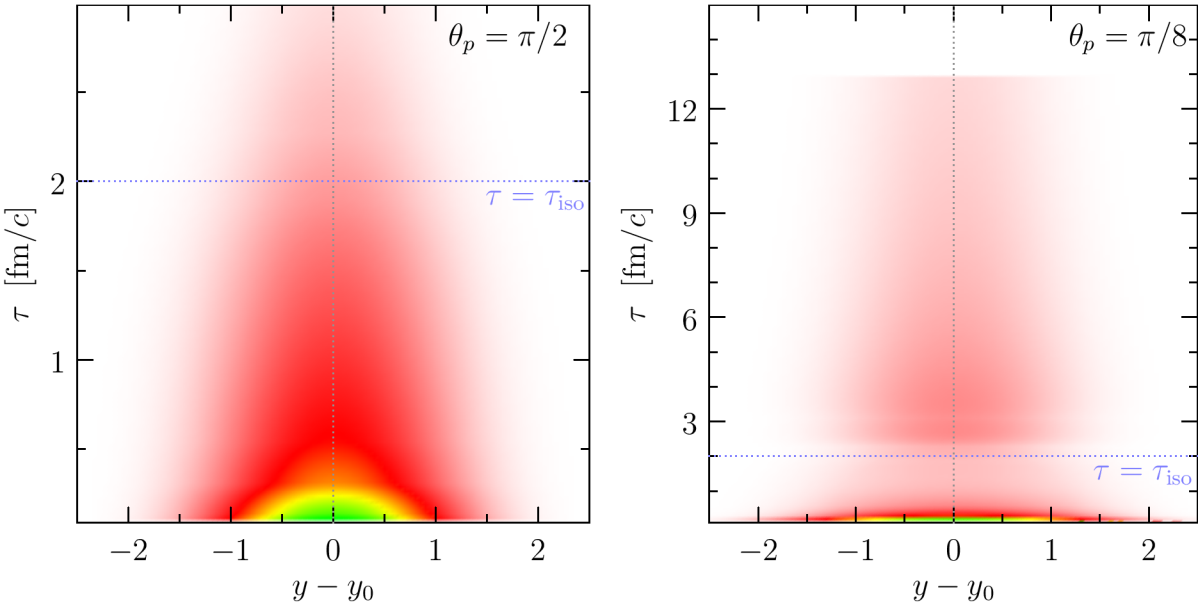

Figure 5.1: The photon production rate in the $\tau - y$ space for different angles. For better visualization, the photon rate has been scaled by a power law. In the left picture, the emission angle is set to $\theta = \pi/2$, which results in a strong maximum (yellow and green area) near the formation time and subsequent cooling. At $\theta = \pi/8$, we can clearly see the suppression of the rate near $\tau = \tau_{\mathrm{iso}}$ (horizontal, dotted line) as well as the longer lifetime and slower cooling of the plasma. The sudden and hard edge in the large τ region of the right plot is caused by the freezeout of the plasma, at which the photon rate is set to zero. The vertical, dotted line indicates the value at which the Doppler factor $\gamma(1-\beta\cos\theta_p)$ is minimal: $y_0 = \operatorname{arctanh}(\cos\theta_p)$.

Additionally to the compactification of the QGP volume, the effect from the Doppler shift does not cause the photon rate to obtain asymmetrical features as shown in Fig. 4.16. Instead, the symmetry axis of the volume shifts towards higher y and is now located at the minimum of the Doppler factor

$$\gamma(1 - \beta\cos\theta_p) = (\cosh y - \sinh y \cos\theta), \tag{5.4}$$

at

$$y_0 = \operatorname{arctanh}(\cos\theta_p)\,. \tag{5.5}$$

5.3. Calculating the spectra

The time-integrated spectra are calculated as follows:

$$\frac{dN}{d\omega_d\, d\Omega_d} = \frac{1}{8\pi} \int_{A_N} dr_x\, dr_y \int_{\tau_0}^{\tau_f} \tau d\tau \int dy\ \omega_d\, \bar{f}(\omega_d[\cosh y - \sinh y \cos\theta], \tau), \tag{5.6}$$

where $\bar{f}$ is the photon production rate in the plasma rest frame according to Eq. (4.18). The spatial coordinates x and y have been renamed to r_x and r_y respectively, to avoid confusion with the rapidity variable.

We write the photon rate per unit rapidity and photon transverse momentum p_T, where

$$p_T = \omega_d \sin\theta_p \tag{5.7}$$

and therefore

$$\frac{dN}{d^2p_T\, dy} = \frac{\pi}{\omega_d} \frac{dN}{d\Omega\, d\omega_d}. \tag{5.8}$$

Integration boundaries for x and y are given by the interaction region from Eq. (4.25). The proper time has a lower bound at the formation time τ_0 and is restricted at the freezeout time τ_f, at which $T < T_c$. Identical to the calculation of the photon pulses, τ_f is determined by the initial temperature of the plasma at $\tau = \tau_0$ and is therefore dependent on the x and y coordinates. The integration over y should cover the entire rapidity space, but is practically limited to some finite values. The photon rate drops off sufficiently to limit the integration to about $|y| < 5$. This is not in contradiction to the rapidity invariance of the Bjorken model, which we implement. The red shifted parts of the plasma (see Fig. 4.1) produce less photons and the strength of the Doppler shift grows with increasing absolute values of the rapidity.

5.3.1. Spectra at different impact parameters

In this section, we calculate spectra at various impact parameters b. Looking at the spectra for emission angle $\theta_p = \pi/2$, we observe a very similar behavior for different b at two fixed isotropization times (Fig. 5.2). The total photon yield for larger plasma volumes (small b) is trivially higher, just as the larger isotropization time increases the time-integrated photon rate due to the temperature evolution $T(\tau)$ according to Fig. 2.5.

As expected, the spectra mostly differ by a scaling factor for various b. The situation looks different for emission angles closer towards forward direction (Fig. 5.3). At $\theta_p = \pi/8$, we see a similar scaling behavior for different impact parameters. For a large isotropization time, however, the spectra exhibit a distinguished dent in the region between 2 and 4 GeV. This energy interval is the same region, where we see double pulses in the calculated time-dependent photon signal. Contrary to the situation at $\theta_p = \pi/2$, the total photon yield is smaller with increasing isotropization times - this relation is investigated in the next section.

5.3.2. Influence of the isotropization time on the spectra

The spectra for different isotropization times at midrapidity are shown in Fig. 5.4. We have two mechanisms working against each other. Large isotropization times extend the plateau in the temperature evolution which leads to higher photon rates. At the same time, a large τ_{iso} leads to a higher buildup of ξ which in turn reduces the photon rate and the time-integrated total yield. At lower emission

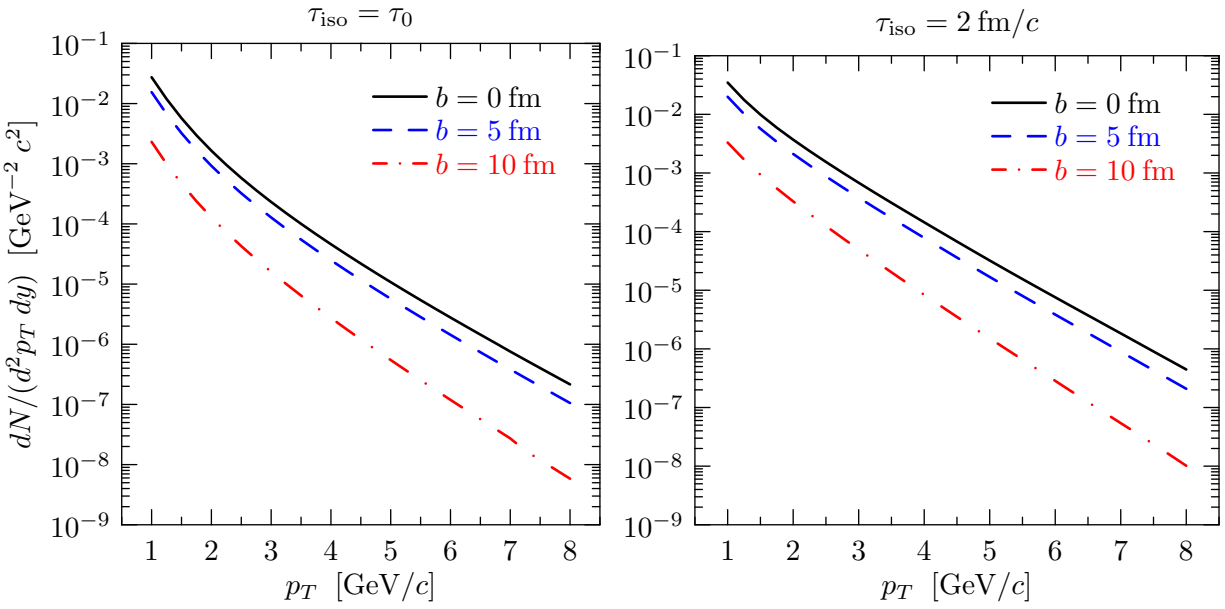

Figure 5.2: Direct photon spectrum at mid-rapidity. At larger b, the total photon yield is lower than for smaller b as smaller plasma volumes directly correspond to lower overall photon emission. $\gamma = 2$, $\delta = 2$, $\theta_p = \pi/2$.

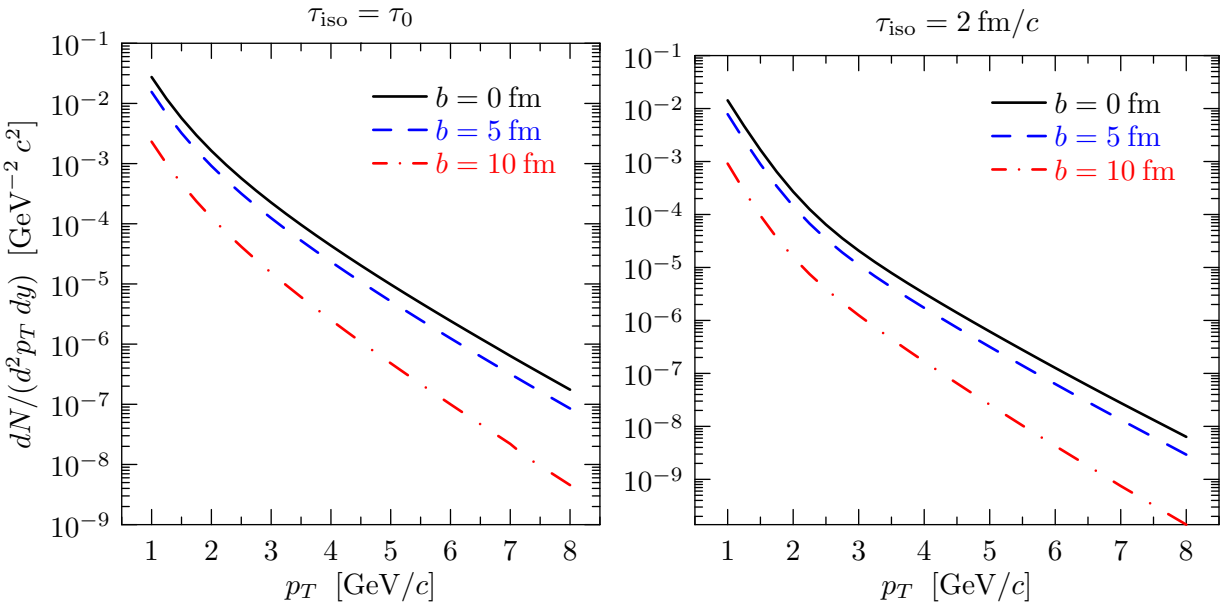

Figure 5.3: Direct photon spectrum in forward direction. The scaling behavior with respect to the impact parameter is the same as in Fig. 5.2. At larger values for $\tau_{\rm iso}$, the spectra exhibit a pronounced dent in the region up to 3 GeV, which is the result of enhanced photon rate suppression at lower emission angles. $\gamma = 2$, $\delta = 2$, $\theta_p = \pi/8$.

angles θ_p, the photon rate is also reduced.

We have seen in Fig. 5.2 how larger $\tau_{\rm iso}$ result in a higher total direct photon yield. This is a consequence of the temperature evolution with fixed final multiplicity (2.9) which features an extended plateau, depending on the isotropization time. One has to keep in mind that the anisotropy also affects the photon rate at midrapidity according to Fig. 3.9. Apparently, the elongated temperature plateau

for increasing $\tau_{\rm iso}$ surpasses the photon rate reduction due to the anisotropy buildup at an emission angle $\theta_p = \pi/2$.

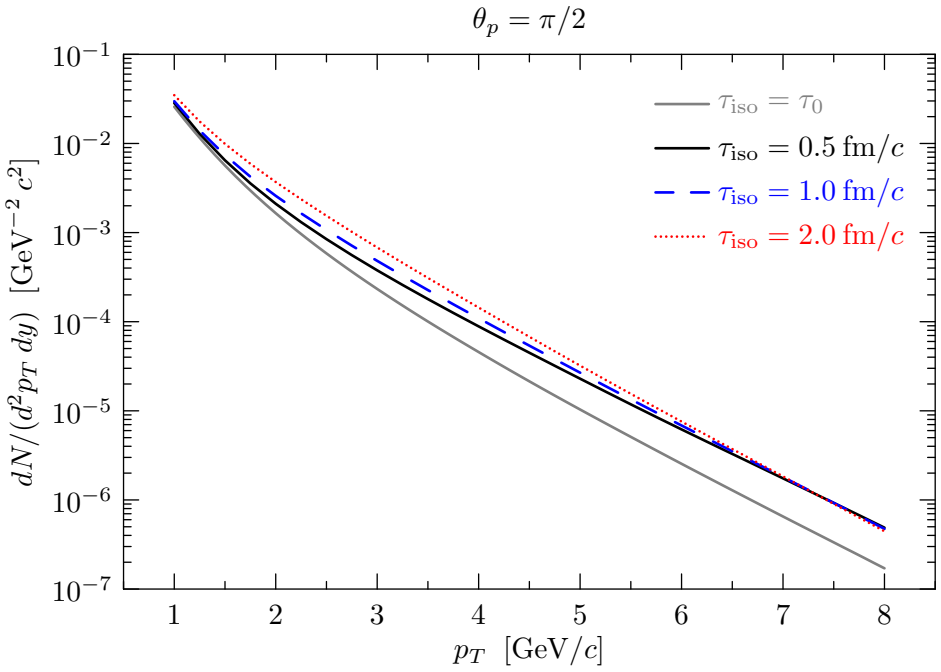

Figure 5.4: Direct photon spectrum at midrapidity ($\theta_p = \pi/2$) for different isotropization times. $\gamma = 2$, $\delta = 2$, $b = 0$.

We compare the effect of the isotropization time for a lower photon emission angle (Fig. 5.5). Since the same color coding is used as in Fig. 5.4, the reverse behavior of the spectra with respect to $\tau_{\rm iso}$ easily seen. The photon rate suppression at a lower angle of $\pi/8$ is strong enough to overcome the increase via the elongated temperature plateau. These two cases at $\theta_p = \pi/2$ and $\theta_p = \pi/8$ suggest that at some intermediate angle, change in isotropization time within some range will have no noticeable or just very little influence on the spectra.

To find the angle at which larger $\tau_{\rm iso}$ lead to lower total photon yields, we compute the ratio

$$\Upsilon(\theta_p, p_T) = \frac{dN(\theta_p, \tau_{\rm iso} = \tau_0)}{dN(\theta_p, \tau_{\rm iso} = 2\,\text{fm}/c)} \tag{5.9}$$

for a range of angles θ_p at various transverse photon momenta p_T. The ratio $\Upsilon(\theta_p, p_T)$ passes through 1 at different angles for different energies (shaded area in Fig. 5.6). At angles below this transition region, increasing $\tau_{\rm iso}$ will lead to lower total photon yields. The different angles, at which the $\Upsilon(\theta_p, p_T)$ in Fig. 5.6 become less than 1 for various energies also indicate a change in shape for the spectra at larger isotropization times.

The previous plots of spectra have shown that the isotropization time of the QGP could be derived by measuring the spectra. For a certain set of model parameters, we have also seen that the spectra for a wide range of isotropization times $\tau_0 < \tau_{\rm iso} < 2\,\text{fm}/c$ lie very close to each other. We can consider a situation where two detectors are available in a heavy-ion collision experiment [88], e.g. at $\theta_p = \pi/2$

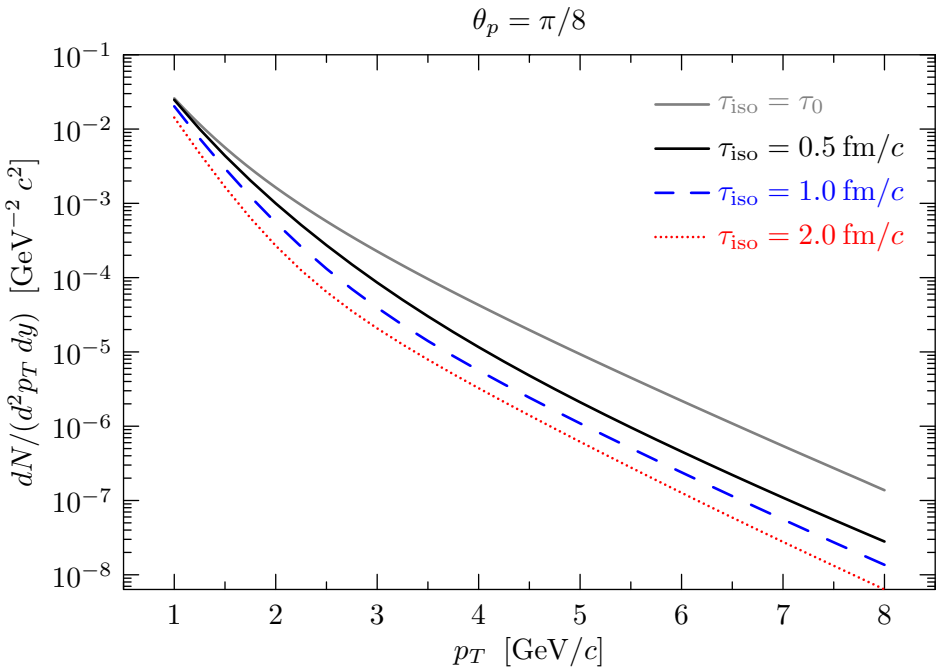

Figure 5.5: Direct photon spectrum closer to forward direction ($\theta_p = \pi/8$) for different isotropization times. $\gamma = 2$, $\delta = 2$, $b = 0$.

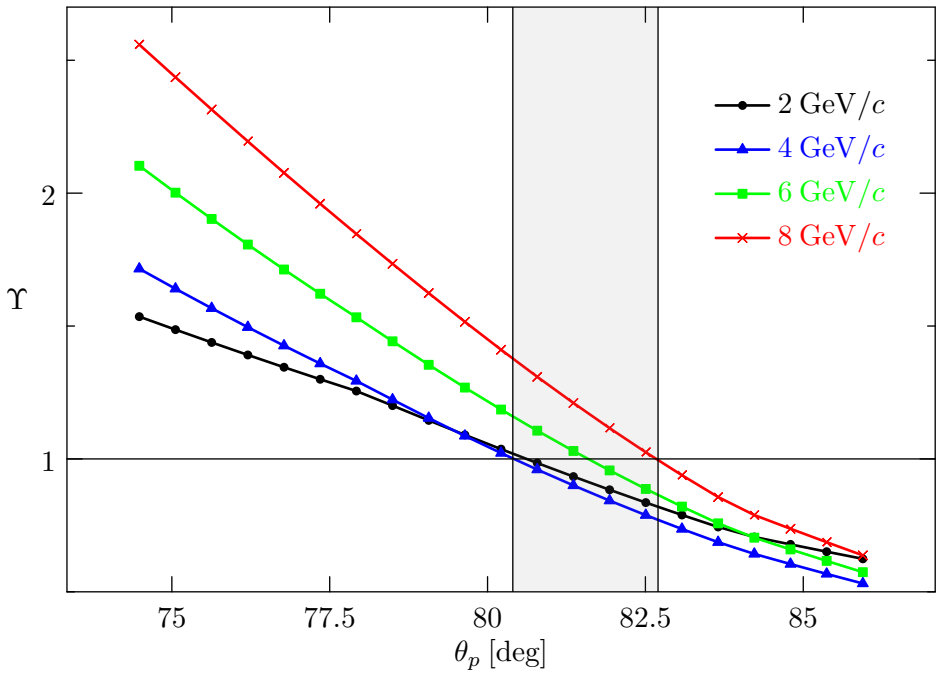

Figure 5.6: The ratio of spectra $\Upsilon(\theta_p, p_T)$ at three different photon momenta p_T. Dots, triangles, squares and crosses represent angles at which the photon yields for specific p_T have been computed. The approximate transition region is indicated by the gray area. $\gamma = 2$, $\delta = 2$, $b = 0$.

and at $\theta_p = \pi/8$. Having recorded the spectra at the two detectors, we can take the ratio

$$\kappa\,(p_T) = \frac{dN/(d^2y\,dp_T)|_{\theta_p=\pi/2}}{dN/(d^2y\,dp_T)|_{\theta_p=\pi/8}}. \tag{5.10}$$

Figure 5.7 shows how building the ratio of spectra at two different angles exploits the dent seen earlier. Such a hypothetical detector set-up would be advantageous, as the measurement at midrapidity would serve as a reference to which the spectra at some other angle could be compared to. The spectra for large isotropization times are suppressed in the high-momentum region. This is reflected by the growing ratio κ, which is almost two orders of magnitude larger for $\tau_{\text{iso}} = 2\,\text{fm}/c$ compared to $\tau_{\text{iso}} = \tau_0$ at $p_T = 8\,\text{GeV}/c$.

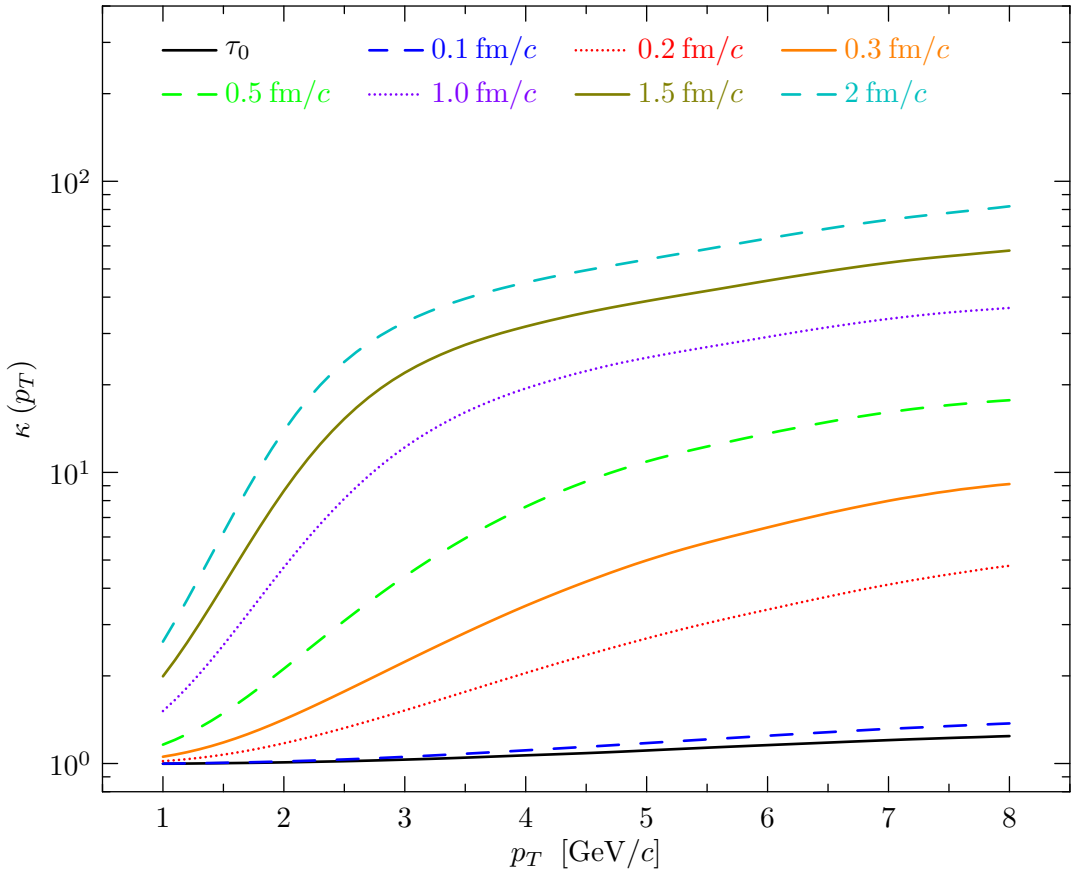

Figure 5.7: The ratio of spectra as defined in Eq. (5.10). The lowest line represents this ratio κ for an isotropization time $\tau_{\text{iso}} = \tau_0$, larger τ_{iso} lie successively higher in this plot. With increasing τ_{iso}, the ratios become larger and the dent in the spectra at $\theta_p = \pi/8$ translates to a more pronounced curvature in this plot. Notice the special sensitivity of the ratio κ to rather early isotropization times $\tau_{\text{iso}} < 0.5\,\text{fm}/c$. $\gamma = 2$, $\delta = 2$, $b = 0$.

We have shown that the isotropization time in the used models have a noticeable effect on the spectra. If one considers a ratio of two spectra at two different emission angles, this effect becomes even more pronounced. Therefore, even without time-resolving detection schemes, one can obtain indirect information about the evolution of the anisotropy parameter. A larger value of the anisotropy parameter ξ would strongly indicate that double pulses can be produced, although they can not be directly measured this way.

In the next Chapter, we investigate the possibility of using identical particle correlation functions to detect the effect of possible double pulses. These correlations have the property that the time evolution of the considered particle source directly translates to a function in momentum space.

I shot an arrow into the air
It fell to earth I knew not where;
For so swiftly it flew, the sight
Could not follow it in its flight.

– Henry Wadsworth Longfellow,
The Arrow and the Song

6

Hanbury Brown - Twiss Correlations

6.1. Overview

We have seen in the last chapter, how the time-integrated quantity, the spectrum, can give hints on a few parameters that have been used in our model so far. In this chapter, we focus on a different method that may provide better insight into the spatiotemporal evolution of the quark-gluon plasma. The so-called *Hanbury Brown - Twiss correlations* (HBT) provide a measurable quantity on the basis of Bose-Einstein quantum statistics.

After an introduction on the concept of HBT correlations and their application to high energy physics, correlation functions are calculated based on the same model that has been used to calculate the photon pulses and spectra.

Extensive introductory and review articles on this topic can be found in e.g. Refs. [89–93].

6.2. The HBT correlation function

Two-particle intensity interferometry was first devised by British physicists Robert Hanbury Brown and Richard Q. Twiss [94], who applied their method to measure the angular size of the star Sirius [95]. In 1960, Goldhaber et al. [96] used intensity interferometry to derive the size of the annihilation fireball in proton-antiproton collisions.

Following the treatment of Refs. [90, 91], we start by considering two bosonic particle emitters A and B. These emitters send out particles with the same energy at $(t_A, \mathbf{x}_A)$ and $(t_B, \mathbf{x}_B)$ respectively, where $\mathbf{x}_A$ and $\mathbf{x}_B$ denote the positions of the emitters. At some later times t_1 and t_2, the particles are detected at two detectors D_1 and D_2, placed at $\mathbf{x}_1$ and $\mathbf{x}_2$. The two emitters may be part of a larger source body, as shown in Fig. 6.1.

The dashed lines in Fig. 6.1 indicate the alternative path of the particles being detected at D_1 and D_2. Since we cannot retrace the path that a certain particle has taken, we need to include both possibilities when forming a detection amplitude. In a wave picture employing spherical waves, one can write the amplitude A_1 (A_2) measured at the detector D_1 (D_2) as

$$A_i \propto \frac{a}{L}\, e^{i[kr_{iA}-\phi_A]} + \frac{b}{L}\, e^{i[kr_{iB}-\phi_B]} \tag{6.1}$$

where L is the approximate distance $r_{iA} = |\mathbf{x}_A - \mathbf{x}_i| \approx |\mathbf{x}_B - \mathbf{x}_i| = r_{iB}$ between sources and detectors and i is the index of the detector (1,2). The magnitude of the wave vectors of the particles are denoted by $k = |\mathbf{k}_1| = |\mathbf{k}_2|$, a and b are the constant source amplitudes, ϕ_A and ϕ_B are two random phases

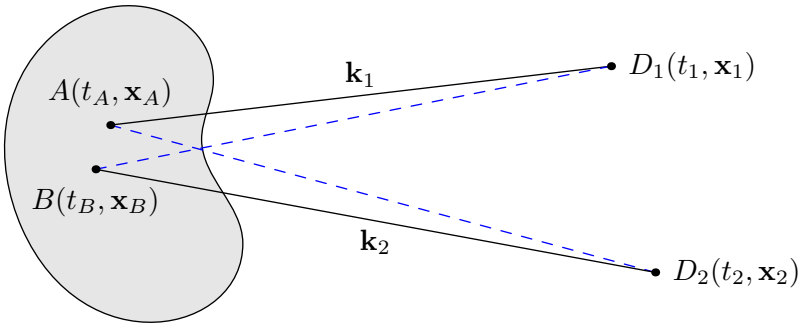

Figure 6.1: Schematic diagram of the emitters (A, B) and detectors (D_1, D_2) in the Hanbury Brown - Twiss scheme. The vectors $\mathbf{k}_1$ and $\mathbf{k}_2$ are differently oriented, but have same magnitude $|\mathbf{k}_1| = |\mathbf{k}_2| = k$. The dashed lines represent alternative paths, which particles emitted at (A,B) and detected at (D_1, D_2) can take.

related to the emission and detection times t_a (t_1) and t_b (t_2). We assume that the distance L between source and detectors is much larger than the distance between the detectors $\mathbf{d} = \mathbf{x}_1 - \mathbf{x}_2$ or the distance between the two point-like emitters $\mathbf{R} = \mathbf{x}_A - \mathbf{x}_B$. The relation $R, d \ll L$ ($R = |\mathbf{R}|$, $d = |\mathbf{d}|$) holds in both the astronomical as well as the high energy physics scenario.

The intensity I_i is the squared modulus of the amplitude and reads

$$I_i = |A_i|^2 = \frac{1}{L^2}\left(a^2 + b^2 + 2\,a\,b\,\cos[k(r_{iA} - r_{iB}) - (\phi_A - \phi_B)]\right). \tag{6.2}$$

Taking the time average of an intensity I_i is equivalent to averaging over a sufficiently large amount of random phases ϕ_A and ϕ_B. In this average, the cosine term in Eq. (6.2) vanishes:

$$\langle I_i \rangle = \frac{a^2 + b^2}{L^2}. \tag{6.3}$$

Thus, by taking the average of such a measured intensity at each detector, we cannot draw any conclusions on the spatial separation R of the two emitters. The more interesting observable here is the so-called *coincidence rate*, which is the joint probability of observing two particles at both detectors. It is formed by multiplying the intensities I_1 and I_2 before taking the average. Expanding the product $I_1 \cdot I_2$ yields, among others, six cosine terms, of which five contain the phase $\phi_A - \phi_B$. As before in the time average, the cosine terms with the phases drop out and the averaged coincidence rate is

$$\langle I_1 I_2 \rangle = \langle I_1 \rangle \langle I_2 \rangle + \frac{2\,a^2\,b^2}{L^4}\cos[k(r_{1A} - r_{1B}) - k(r_{2A} - r_{2B})], \tag{6.4}$$

and the two-particle correlation function is

$$C_2 = \frac{\langle I_1 I_2 \rangle}{\langle I_1 \rangle \langle I_2 \rangle} = 1 + 2\frac{a^2\,b^2}{[a^2 + b^2]^2}\cos[k(r_{1A} - r_{1B} - r_{2A} + r_{2B})]. \tag{6.5}$$

The form of the correlation function given in Eq. (6.5) can be further simplified. For an application in high energy physics, the size of the source is much smaller than the separation of the detectors and in this limit $R \ll d$, the cosine term reduces to (see Appendix C)

$$\cos(\mathbf{R}[\mathbf{k}_1 - \mathbf{k}_2]). \tag{6.6}$$

The momentum difference $\mathbf{k}_1 - \mathbf{k}_2$ is accessible via experimental control, and the evaluation of the correlation function would yield a value for R.

In a few words, one can summarize the relevance of HBT correlations with regards to high energy physics as following: the measurement of C_2 can give us insight on the spatial extent of the photon emitting volume.

Moving away from two point-like emitters to a continuous source with finite size, one could adapt a more suitable approach to the matter, as done by D. Neuhauser [97]. In this approach, the quark-gluon plasma[1] is modeled as a sum of N currents that are randomly oriented in space.

In this current formalism, the n-photon inclusive distribution function is defined as

$$P(k_1 \dots k_2)A_n = \langle |M_{\varepsilon_1 \mathbf{k}_1}|^2 \dots |M_{\varepsilon_n \mathbf{k}_n}|^2 \rangle, \tag{6.7}$$

where the A_n are some normalization factors and the M_i denote the amplitude to produce a photon with momentum $\mathbf{k}_i$ and polarization ε_i. The two-photon correlation function is

$$C_2(\mathbf{k}_1, \mathbf{k}_2) = \frac{P(\mathbf{k}_1, \mathbf{k}_2)}{P(\mathbf{k}_1)P(\mathbf{k}_2)}. \tag{6.8}$$

The amplitudes M_i are considered to be connected to classical currents $\mathbf{J}$:

$$M_{\varepsilon,\mathbf{k}} = \varepsilon \cdot \mathbf{J}(\mathbf{k}), \tag{6.9}$$

with $\mathbf{J}(\mathbf{k})$ being the Fourier transform of the current

$$\mathbf{J}(\mathbf{x}, t) = \sum_l^N \mathbf{j}_l(\mathbf{x} - \mathbf{x}_l, t - t_l) \tag{6.10}$$

and

$$\mathbf{J}(\mathbf{k}) = \sum_l^N \mathbf{j}_l(\mathbf{k}) e^{i\, k \cdot x_l}. \tag{6.11}$$

The above sum represents a summation over all partial currents $\mathbf{j}_l$ within the fireball. Every partial current $\mathbf{j}_l$ arises from a collision of two nucleons in the fireball. After performing the spatial averages over the random currents (see Appendix D), one gets the following result for the two-photon correlation function:

$$C(\mathbf{k}_1, \mathbf{k}_2) = 1 + \frac{1}{4}\left(1 + [\hat{\mathbf{k}}_1 \cdot \hat{\mathbf{k}}_2]^2\right)\left(|\rho(q)|^2 + |\rho(p)|^2\right), \tag{6.12}$$

with $p = k_1 + k_2$, $q = k_1 - k_2$, and ρ being the Fourier transformed space-time source density of the photon emitting region. The important point in this result is the fact that the Fourier transformation is applied to the three spatial components as well as to the temporal component of the source function. Hence, the correlation function is sensitive to the whole spatiotemporal evolution of the quark-gluon plasma until its freezeout.

As is the case with spectra, correlation function measurements of pions only yield information about the freezeout surface and are therefore not suitable to investigate the internal dynamics of the QGP. Pions, however, are easier to measure than direct photons, and can be used to study other effects, such as elliptic flow [98].

[1] Also referred to as "fireball" in e.g. Ref. [97]

6.3. Analytic double pulse model

Before we start engaging in numerical computations, the analytic result (6.12) in the chaotic current formalism from Ref. [97] allows us to compute the correlation function for a certain source distribution function ρ. This result is limited to a fully chaotic source, meaning that there are no coherence effects from e.g. some collective deceleration of the fireball. By employing a source function that shares some common features with the photon rate we used throughout, we may be able to predict the form of C_2 and its sensitivity to one or more model parameters.

The photon source density is usually modeled as a Gaussian in 3+1 dimensions

$$\rho(x) \propto \exp\left(-\frac{\mathbf{x}^2}{2R} - \frac{t^2}{2\tau^2}\right), \tag{6.13}$$

where R and τ can be interpreted as the radius and the lifetime of the fireball respectively, and τ is not to be confused with the proper time. A minimalistic extension of a Gaussian source would be to add a second, time delayed Gaussian:

$$\rho(x) \propto \exp\left(-\frac{\mathbf{x}^2}{2R^2}\right)\left[a_1 \exp\left(-\frac{(t-t_1)^2}{2\tau_1^2}\right) + a_2 \exp\left(-\frac{(t-t_2)^2}{2\tau_2^2}\right)\right]. \tag{6.14}$$

This extension mimics the second maximum in the photon production rate by employing two peaks in the time direction with maxima at $t = t_1$ and $t = t_2$, as well as lifetimes τ_1 and τ_2. The amplitudes a_1 and a_2 fulfill $a_1 + a_2 = 1$, so that this extended Gaussian reduces to the original one in Eq. (6.13) for $t_1 = t_2 = 0$. A Gaussian like this is easily transformed into momentum space:

$$\begin{aligned}\rho(k) &= \int d^4x\, e^{ikx}\, \rho(x) = \\ &= \exp\left(-\frac{1}{2}\mathbf{k}^2R^2\right)\left[a_1 \exp\left(ik_0t_1 - \frac{1}{2}k_0^2\tau_1^2\right) + \exp\left(-ik_0t_2 - \frac{1}{2}k_0^2\tau_2^2\right)\right].\end{aligned} \tag{6.15}$$

Appropriate normalization constants have been chosen. For a rough idea on how this new double Gaussian affects the HBT function, we can simplify the source by choosing $a_1 = a_2$ as well as $t_1 = -t_2 = t_D/2$ and $\tau_1 = \tau_2 = \tau$, which corresponds to two pulses with same height, separated by t_D (Fig. 6.2).

In this rather symmetric configuration, the Fourier transformed density can be written as

$$\rho(k) = \exp\left(-\frac{1}{2}[\mathbf{k}^2R^2 + k_0^2\tau^2]\right)\, \cos(k_0t_D/2). \tag{6.16}$$

Hence, the implementation of a second Gaussian pulse to the source function modifies the original density by an additional cosine factor, which depends on the photon energy and the pulse separation t_D.

To demonstrate how the correlation function changes with the pulse separation, we investigate the simplest HBT geometry. This special case is given by the choice of the two photon vectors $\mathbf{k}_1$ and $\mathbf{k}_2$, which we set parallel to each other, $\mathbf{k}_1 \parallel \mathbf{k}_2$. The remaining degree of freedom is the photon energy difference, so we choose $\mathbf{k_1} = \mathbf{k_2} + \mathbf{q}$. The source density in Eq. (6.14) exhibits a spatial spherical symmetry, so we can place the two photon vectors along any arbitrary direction.

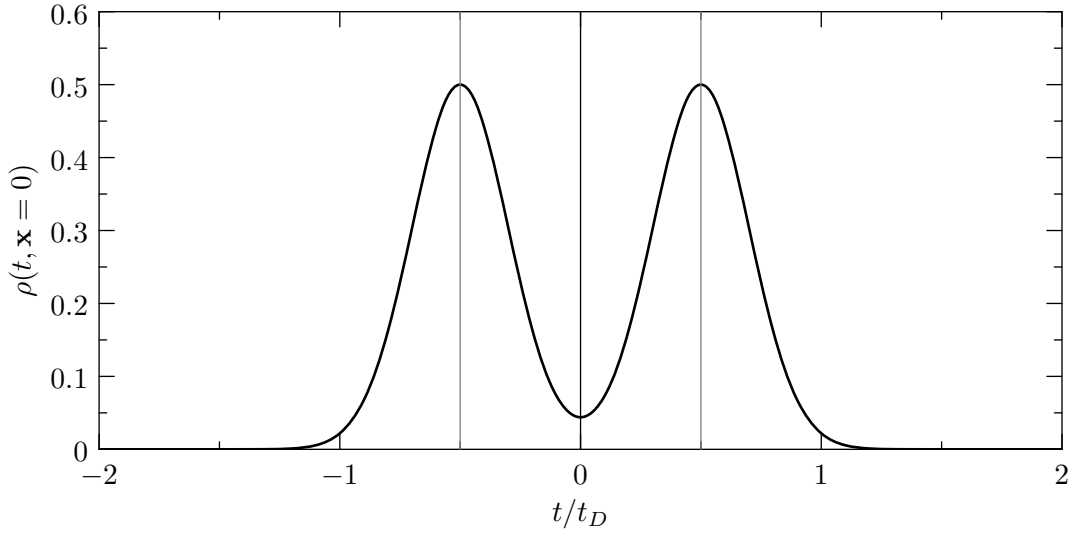

Figure 6.2: The double Gaussian with $\tau = 0.2$ at $\mathbf{x} = 0$. The peaks are separated by t_D and their maxima are located at $t = \pm t_D/2$.

If $|\mathbf{k}_2| \gg \frac{1}{2R}$ and $|\mathbf{k}_2| \gg \frac{1}{2\tau}$, the term $\rho(p) = \rho(k_1 + k_2)$ is small against $\rho(q) = \rho(k_1 - k_2)$ and can be neglected. This is a scenario we encounter for photons in the GeV range:

$$\begin{aligned} C_2(q) &= 1 + \frac{1}{2}\left| \exp\left(-\frac{1}{2}\mathbf{q}^2 R^2 - \frac{1}{2}[q^{(0)}]^2\tau^2\right)\right|^2 \cdot \cos^2(q^{(0)}\, t_D/2) = \\ &= 1 + \frac{1}{2}\exp\left(-\mathbf{q}^2 R^2 - [q^{(0)}]^2\tau^2\right) \cdot \cos^2(q^{(0)}\, t_D/2) \end{aligned} \tag{6.17}$$

Before plotting and interpreting the correlation function for some parameter set, one should consider a few points. Firstly, the source function in Eq. (6.14) is apparently not rapidity invariant and is given strictly in laboratory coordinates. Consequently, the separation time cannot be simply related to the isotropization time, which is given in the local rest frame. Secondly, the spatial extent of the plasma is defined by R, which also holds for the size in the longitudinal direction. This is in contradiction to our previous model assumption that the plasma is much larger along the beam than in the transverse directions. These are reasons, why parameters used for this analytic demonstration can not give any quantitative predictions for the full numerical treatment.

Figure 6.3 shows the correlation function for two different values of t_D. This plot already demonstrates the main characteristics of a HBT function. For photons with two polarization degrees of freedom, the correlation function is bounded between 1 and $\frac{3}{2}$ [99], and its width is mainly determined by the spatiotemporal extent of the source. Larger R and τ would result in a narrower correlation function. The dashed line in Fig. 6.3 shows C_2 for a very large pulse separation time. The squared cosine term exhibits a period of $2\pi/t_D$, which in the case of $t_D = 10\,\mathrm{fm}/c$ is about $125\,\mathrm{MeV}/c$ - the second maximum of the oscillation is clearly visible in that region in Fig. 6.3.

We conclude that in order to see a noticeable effect from the anisotropy induced photon rate suppression on the HBT correlation function, we need similar prerequisites as in the time-resolved detector signal. Larger centralities result in smaller plasma sizes and a broadening of the correlation function, which in turn make the oscillating portion visible for smaller t_D.

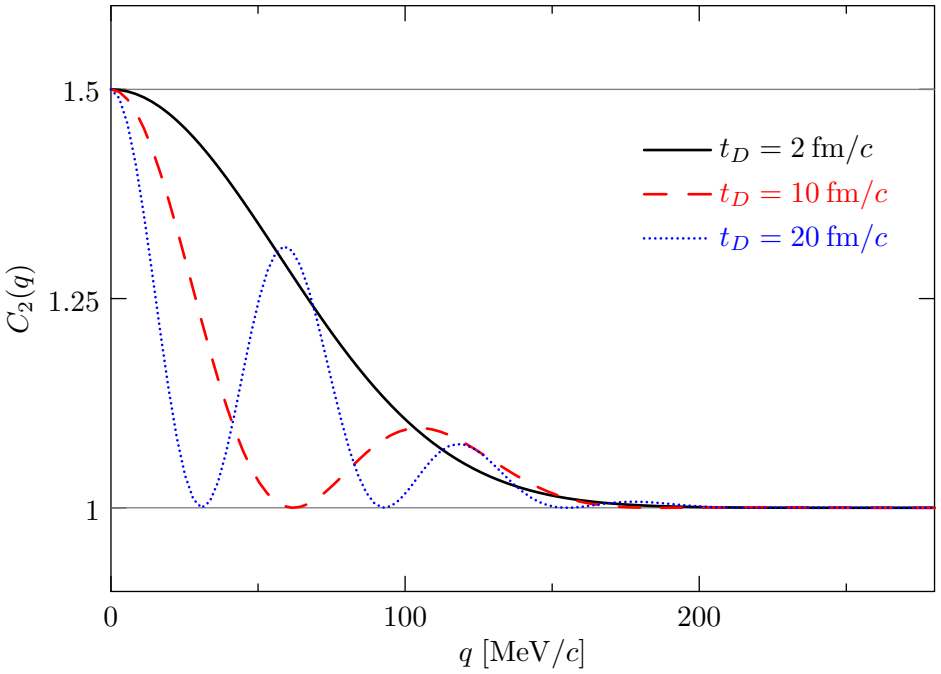

Figure 6.3: Two-photon correlation function C_2 as a function of momentum difference q. The curves show the HBT function for different separation times t_D. The spatial radius R and the overall lifetime τ of the double-Gaussian source determines the width of the HBT function in momentum space, whereas the separation time is responsible for oscillations. $R = 2$ fm, $\tau = 1$ fm/c

6.4. Calculating the correlation functions

In terms of the four-dimensional differential photon rate, the two-photon correlation function is still given by Eq. (6.8), where [100]

$$P(\mathbf{k}) = \int d^4x \frac{dR(x,\mathbf{k})}{d^4x\, d^3k} \tag{6.18}$$

and

$$P(\mathbf{k},\mathbf{k}') = \int d^4x_1\, d^4x_2 \frac{dR(x_1,\mathbf{k})}{d^4x_1\, d^3k} \frac{dR(x_2,\mathbf{k}')}{d^4x_2\, d^3k'} \left[1 + \frac{1}{2}\cos(\Delta k \cdot \Delta x)\right], \tag{6.19}$$

with

$$\Delta k = k - k', \tag{6.20a}$$
$$\Delta x = x_1 - x_2. \tag{6.20b}$$

A slightly different form of the HBT correlation function was suggested in Ref. [101], which automatically ensures that the quantum statistical bounds for a fully chaotic source are not violated:

$$P(\mathbf{k},\mathbf{k}') = \int d^4x_1\, d^4x_2 \frac{dR(x_1, \frac{\mathbf{k}+\mathbf{k}'}{2})}{d^4x_1\, d^3k} \frac{dR(x_2, \frac{\mathbf{k}+\mathbf{k}'}{2})}{d^4x_2\, d^3k'} \left[1 + \frac{1}{2}\cos(\Delta k \cdot \Delta x)\right]. \tag{6.21}$$

In the following calculations, we use the same model for the QGP as was implemented in the calculation of the double pulses as well as the spectra (see Chapter 4 and Chapter 5). As we need to integrate over the four-dimensional volume of the plasma, it is appropriate to switch to rapidity and proper

time variables, as was done to calculate spectra. In these coordinates, the position and momentum vectors are

$$x_i = \begin{pmatrix} \tau_i \cosh y_i \\ r_{x,i} \\ r_{y,i} \\ \tau_i \sinh y_i \end{pmatrix} \tag{6.22}$$

and

$$k_i = \omega_i \begin{pmatrix} 1 \\ \sin\theta_i \cos\varphi_i \\ \sin\theta_i \sin\varphi_i \\ \cos\theta_i \end{pmatrix}. \tag{6.23}$$

To avoid confusion, the usual notation for the spatial x and y coordinates has been changed to r_x and r_y respectively. The scalar product $\Delta k \cdot \Delta x$ can be expanded as

$$\Delta k \cdot \Delta x = (k_1 - k_2)_\mu (x_1 - x_2)^\mu \tag{6.24}$$

and we collect the terms according to their index (1) or (2):

$$\begin{aligned} \Delta k \cdot \Delta x = \sum_{i=1}^{2} (-1)^{i+1} \{ & \tau_i [(\omega_1 - \omega_2)\cosh y_i - (\omega_1 \cos\theta_1 - \omega_2 \cos\theta_2)\sinh y_i] \\ & - r_{x,i}[\omega_1 \cos\varphi_1 \sin\theta_1 - \omega_2 \cos\varphi_2 \sin\theta_2] \\ & - r_{y,i}[\omega_1 \sin\varphi_1 \sin\theta_1 - \omega_2 \sin\varphi_2 \sin\theta_2]\} \\ = \sum_{i=1}^{2} \Gamma_i . & \end{aligned} \tag{6.25}$$

This separation of the terms with respect to τ_i, $r_{x,i}$, $r_{y,i}$ and y_i, which are being integrated over, allows to rewrite the cosine term as

$$\cos(\Delta k \cdot \Delta x) = \cos(\Gamma_1 + \Gamma_2) = \cos\Gamma_1 \cos\Gamma_2 - \sin\Gamma_1 \sin\Gamma_2 . \tag{6.26}$$

Since the Γ_i only contain integration variables of the same index i and the photon rates in Eq. (6.21) have the same argument, the integration over d^4x_1 and d^4x_2 can be performed independently. Thus, the eight-dimensional integral has been effectively reduced to two four-dimensional integrations:

$$C_2(\mathbf{k}, \mathbf{k}') = 1 + \frac{1}{2} \frac{\left(\int d^4x \, \frac{dR(x,[k+k']/2)}{d^4x \, d^3k} \cos\Gamma \right)^2 + \left(\int d^4x \, \frac{dR(x,[k+k']/2))}{d^4x \, d^3k} \sin\Gamma \right)^2}{P(\mathbf{k}) P(\mathbf{k}')}, \tag{6.27}$$

where

$$\begin{aligned} \Gamma = \{ & \tau[(\omega_1 - \omega_2)\cosh y - (\omega_1 \cos\theta_1 - \omega_2 \cos\theta_2)\sinh y] \\ & - r_x[\omega_1 \cos\varphi_1 \sin\theta_1 - \omega_2 \cos\varphi_2 \sin\theta_2] \\ & - r_y[\omega_1 \sin\varphi_1 \sin\theta_1 - \omega_2 \sin\varphi_2 \sin\theta_2]\}, \end{aligned} \tag{6.28}$$

with the four-dimensional integration measure

$$d^4x = \tau d\tau \, dy \, dr_x \, dr_y . \tag{6.29}$$

The two integrals in Eq. (6.28) have to be evaluated for every pair of momentum vectors $\mathbf{k}$ and $\mathbf{k}'$. Due to the sine and cosine terms, the integrand shows oscillatory behavior. To compute the correlation function, the integration has been split up into two parts. The rapidity and proper time coordinates are being integrated first using *Mathematica*'s integration strategy `OscillatorySelection`, which is specifically aimed at oscillating integrands with finite boundaries. In a second step, the remaining integration over the two spatial coordinates r_x and r_y is performed.

To compute the correlation function for a pair of photon wave vectors $\mathbf{k}$ and $\mathbf{k}'$, one needs to perform a total of four integrations. Using the implementation in *Mathematica*, the computation time of C_2 for two specific photon vectors is around one to ten minutes, depending on the needed numerical accuracy.

6.4.1. Collinear configuration

We focus on a very simple configuration at first. The two photon vectors are fixed to point into the same direction ($\mathbf{k} \parallel \mathbf{k}'$) at an angle θ away from the beam axis, only differing in magnitude:

$$\mathbf{k} = \mathbf{k}' + \mathbf{q}. \tag{6.30}$$

We will start by investigating the correlation function as means to extract the spatial size of the quark-gluon plasma. For this task, we can point the photon vector pair towards midrapidity ($\theta = \pi/2$) and calculate the correlation function at different impact parameters.

Per definition, C_2 should be exactly $\frac{3}{2}$ at $q = 0$. In some the following plots, the correlation functions do not always reach $C_2(0) = \frac{3}{2}$. The main reason for this apparent inconsistency with the quantum statistical bound [99] is the oscillating integrand. If the two photon vectors have the same magnitude and are almost parallel, the argument in the cosine and sine terms in Eq. (6.27) can be considered small and the integrand does not oscillate heavily - compared to a situation where the two photon vectors are separated by some larger finite angle or a larger momentum difference. In such a situation, the integration kernel that is tailored to oscillating integrands is not very effective and may treat numerical artifacts arising from the linear interpolation of the photon rate data(see Fig. 3.12) as some oscillation period. Other integration strategies, however, require very long computation times at large separation angles or large momentum differences. For practical reasons, we choose to use the oscillatory integration strategy throughout the calculations, since we are mostly interested in qualitative figures. A more elaborate technique to tackle this problem would be to analyze the integrand for a given photon pair and to check which integration strategy is more advantageous. In addition to the calculations which produced the plots in this chapter, we calculated the HBT function $C_2(0)$ for those curves, which did not reach $C_2 = \frac{3}{2}$ with a different integration strategy and found all of them in agreement with the quantum statistical bound.

Figure 6.4 shows how smaller QGP sizes widen the correlation function. The curves for larger isotropization times in this configuration only differ very slightly, which means that the HBT function is not sensitive towards the lifetime of the QGP if the photon vectors point towards midrapidity.

Moving away from midrapidity, we point our photon vector pair into forward direction, $\theta = \pi/4$, and then vary the isotropization time. Doing so reveals an interesting feature for a large value of τ_{iso} (Fig. 6.5). First, we see that longer isotropization times have an effect on the HBT function, if the photon vectors point away from midrapidity - larger τ_{iso} reduce the width of C_2. For $\tau_{\text{iso}} = 2\,\text{fm}/c$, the correlation function exhibits a plateau-like shape between 1 and 2 GeV/c. Increasing τ_{iso} to unrealistically high values reveals an even more remarkable new shape (Fig. 6.6), the plateau turned into a second, distinct peak, similar to Fig. 6.3. The dashed, blue line represents the correlation

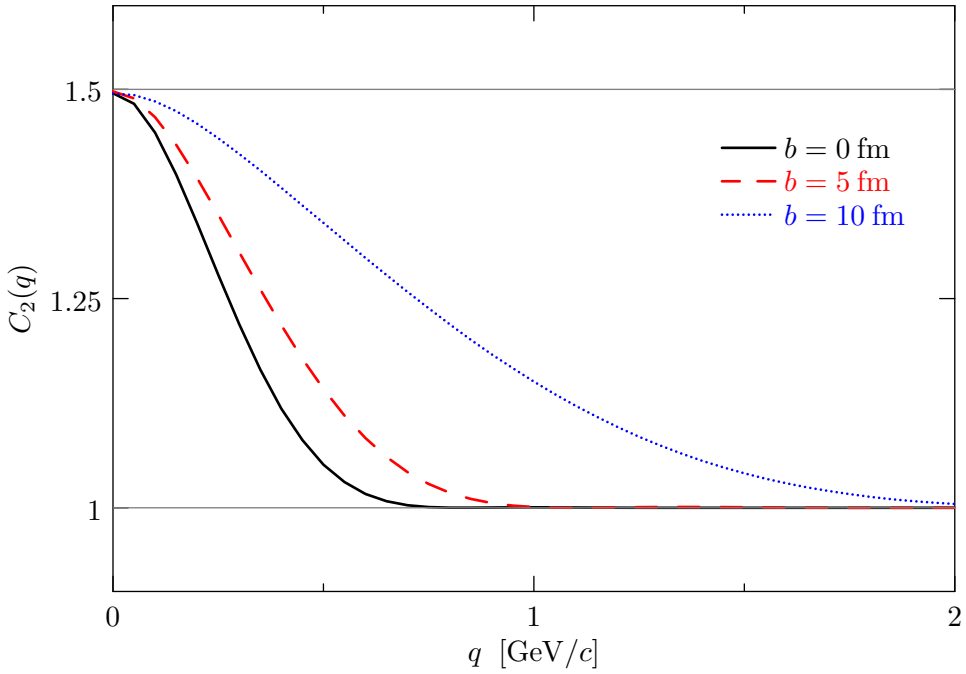

Figure 6.4: Two-photon correlation function at different impact parameters b. Large plasma sizes and therefore small b result in a quenched HBT function. Small plasma sizes are therefore necessary to observe any kind of modulation to the trivial shape of the correlation function. $\tau_{\text{iso}} = \tau_0$, $|\mathbf{k}'| = 2\,\text{GeV}/c$, $\theta = \pi/2$.

function with the same parameters except for a much shorter transition width.

Turning back to reasonable scenarios, such as $\tau_{\text{iso}} \leq 2\,\text{fm}/c$ and $\gamma = 2$, we can scan through different angles θ and try to determine when the plateau starts to emerge (Fig. 6.7).

Figure 6.7 reveals two aspects. First, the photon rate suppression does not have the same maximal effect on the HBT function at lowest angles, as was the case in the time-dependent photon signal. The second peak or plateau starts emerging noticeably at $\theta = \pi/8$ and moves towards lower momentum differences q as well as growing in amplitude with increasing angle. Secondly, the width of the correlation function decreases as the angle grows.

The measurement of direct photon correlations is a particularly difficult task for almost the same reasons as measuring direct photon spectra. There have only been very few HBT measurements from QGP photons in heavy-ion colliders [102–105]. In this section, we have restricted ourselves to the simplest possible geometry to perform the computation of the HBT function, as was done in e.g. Ref. [100]. As of now, it is not possible to measure collinear photon correlations in a calorimeter [106]. While there is the conceptual possibility to use the conversion of photons to e^-e^+-pairs in the calorimeter to measure the collinear HBT function, this would require a good knowledge on the angle dependence of C_2. The minimal angle for a photon pair to be registered as individual particles is determined by the physical resolution of the detector.

In experiments, the full detector surface is utilized to gather data, which is then processed to extract the correlation function. To reconstruct a scenario for a given detector geometry, the integration would have to be extended to all possible combinations of photon pairs, including some energy cuts as well as restrictions on the angle between the photon momentum vectors [93]. Such an integration over six more degrees of freedom $d^3k\,d^3k'$ is not feasible on an ordinary desktop computer anymore and would

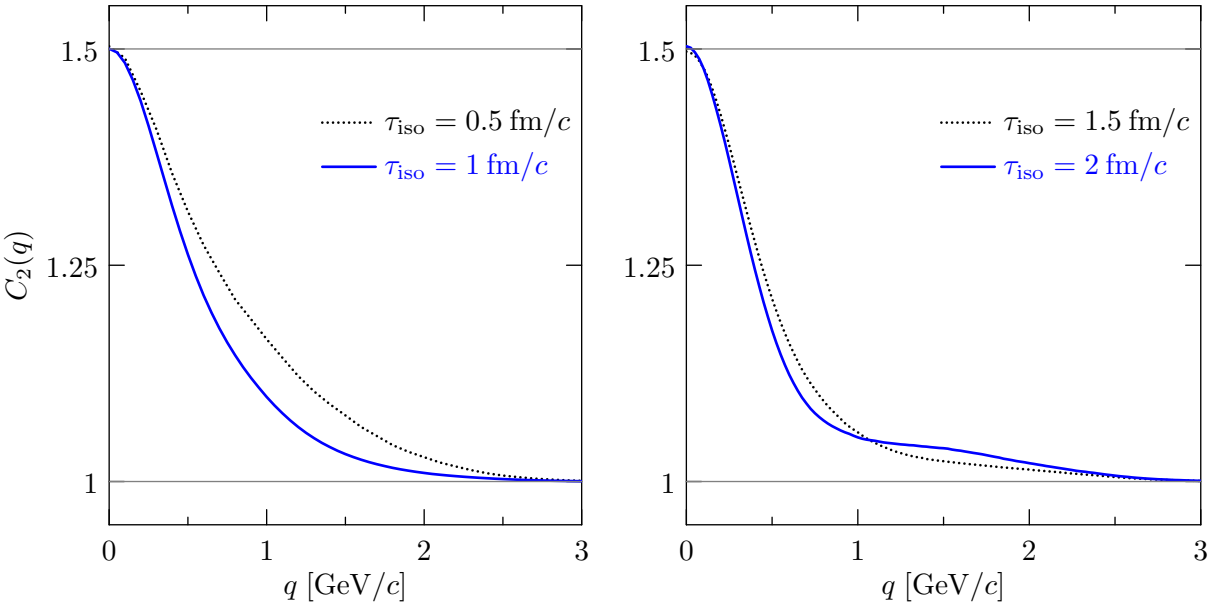

Figure 6.5: Two-photon correlation function at different isotropization times. Strong oscillations, as indicated by Fig. 6.3 are not seen. Nevertheless, we see the expected behavior of the width of the HBT function with respect to $\tau_{\rm iso}$. Larger isotropization times lengthen the lifetime of the plasma, expanding its four-volume. This results in a less wide correlation function, similar to Fig. 6.4. $|\mathbf{k}'| = 2\,\mathrm{GeV}/c$, $\theta = \pi/4$, $b = 10\,\mathrm{fm}$.

require massive parallel computing to finish in an affordable time.

We make a quick estimation on how much computation time a discretized version of the problem can take. Using the ansatz from Ref. [93], the projection of the correlation function onto transverse and longitudinal components of the momentum difference q can be written as

$$C_2^{\rm proj}(q_T, q_L) = \frac{\int d^3k_1 d^3k_2\, P(k_1,k_2) A(q_T, q_L; k_1, k_2)}{\int d^3k_1 d^3k_2\, P(k_1) P(k_2) A(q_T, q_L; k_1, k_2)}, \tag{6.31}$$

where $A(q_T, q_L; k_1, k_2)$ is a window function that includes the energy cuts as well as angle difference cuts inspired by the experimental procedures. We turn the integrals in Eq. (6.31) into sums and therefore discretize the detector into a spatial grid. Considering such a grid with m horizontal and n vertical segments, the number of possible combinations to point the two photon vectors towards two distinct detector segments is given by

$$\binom{m \cdot n}{2}. \tag{6.32}$$

We then assume the length of the vectors to be discretized into q segments, which leads to q^2 possible combinations for both vectors:

$$N_{\rm pos} = \binom{m \cdot n}{2} q^2 = (m \cdot n - 1) \cdot (m \cdot n) \cdot \frac{q^2}{2}. \tag{6.33}$$

For a spatial grid of $m = n = 32 \rightarrow m \cdot n = 1024$ detector segments and $q = 8$ different photon momenta, we already have roughly 33.5 million possible photon pair combinations. The current implementation used to calculate the HBT function for the collinear case takes about 10 s to compute

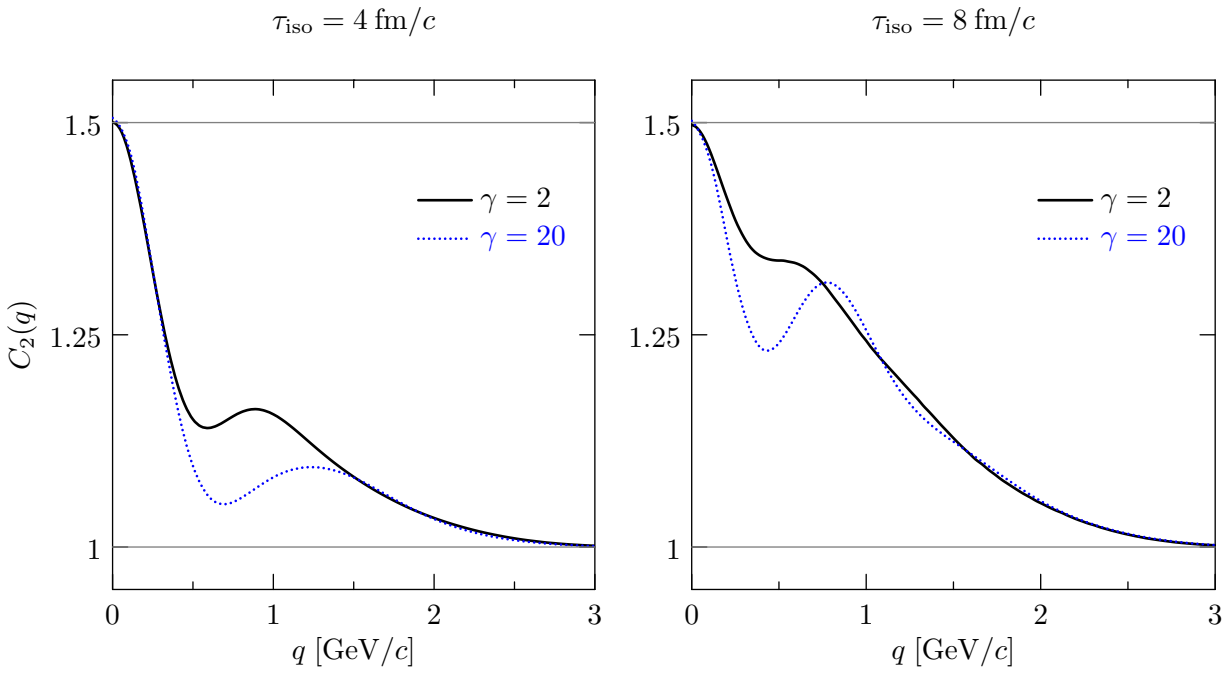

Figure 6.6: C_2 at rather extreme values of τ_{iso} and two different values for the transition width γ. The second peaks of the HBT functions show that the concept of a double-Gaussian introduced and shown Fig. 6.2 partially holds for a photon rate with larger transition parameters. $|\mathbf{k}'| = 2\ \mathrm{GeV}/c$, $\theta = \pi/4$, $b = 10\ \mathrm{fm}$.

the single-inclusive distribution $P(k_1)$. The two-particle distribution function $P(k_1, k_2)$ already needs at least a minute of computation time. According to Eq. (6.31), we need to sum over all photon pair combinations twice, each combination taking $2 \times 10\ \mathrm{s}$ and $60\ \mathrm{s}$ respectively. For our small grid, this would already take around 750,000 CPU hours, just to compute C_2^{proj} for a single pair (q_T, q_L)! While this is a worst-case estimate in terms of the amount of vector pair positions, the computation time of Eq. (6.28) can significantly increase past the $60\ \mathrm{s}$ mark for large momentum differences or large relative angles.

6.4.2. Correlations for non-collinear configurations

In this section we consider another photon pair configuration that only features one degree of freedom. The configuration with relative photon vector angles does not suffer from the drawback that identical particles have to be registered at the same detector segment, which is of practical difficulty. One photon momentum vector is fixed in the reaction plane, whereas the other is varied at a different angles. The magnitude of both vectors is kept fixed, turning the relative angle between the vectors into the only degree of freedom. Figure 6.8 illustrates the position of the vectors.

In Section 3.4 we have computed differential photon rates for angles $0 \leq \theta_p \leq \pi/2$. Within the reaction plane (x-z-plane), we consider the photon rate to be symmetric for polar angles larger than $\pi/2$, so that

$$0 \leq \theta_p < \frac{\pi}{2} \Longrightarrow \theta_p, \tag{6.34a}$$

$$\frac{\pi}{2} \leq \theta_p \leq \pi \Longrightarrow \pi - \theta_p. \tag{6.34b}$$

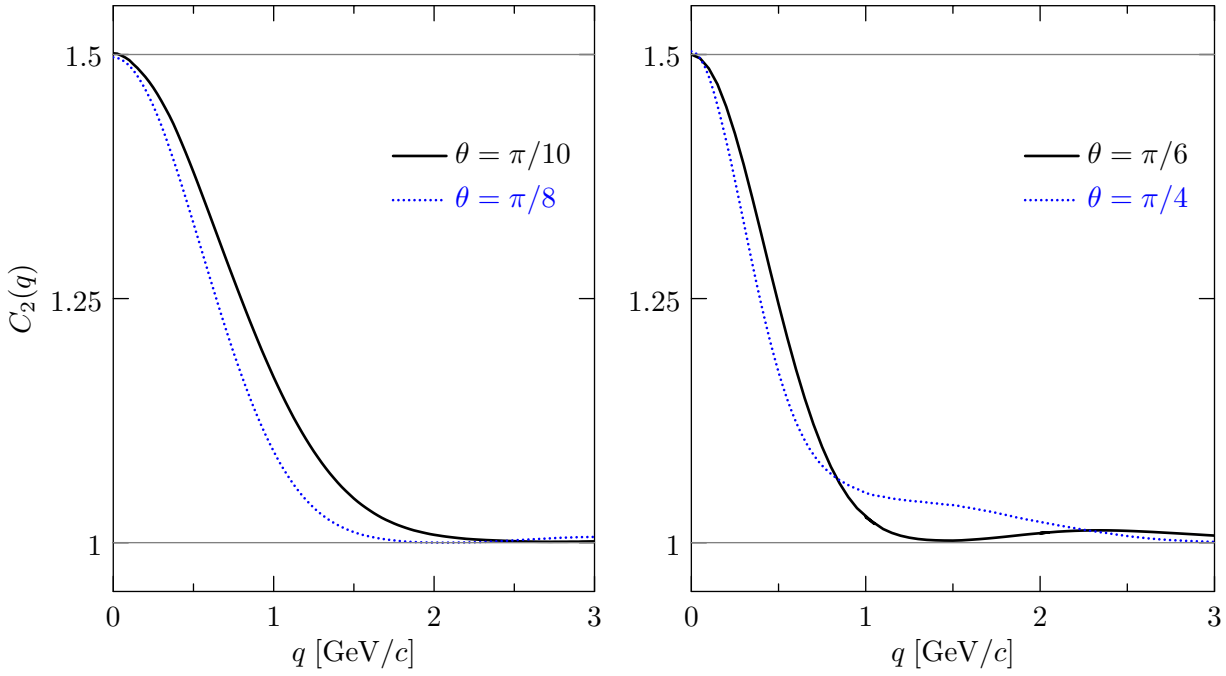

Figure 6.7: HBT function for different angles θ. The plateau emerges at $\theta_p = \pi/6$ and exhibits a minimum which looks similar to the oscillating features in Fig. 6.3. For a larger angle $\theta_p = \pi/4$, the second peak closes in to the main Gaussian structure of the HBT function and creates a plateau. $\gamma = 2$, $\tau_{\text{iso}} = 2\,\text{fm}/c$, $|\mathbf{k}'| = 2\,\text{GeV}/c$, $b = 10\,\text{fm}$.

HBT correlations for photon pair configurations as depicted in Fig. 6.8 are shown in Fig. 6.9. The polar angle θ_1 is fixed at 10° for the first momentum vector, the second vector is varied with respect to the relative angle θ_{rel} between the two vectors. This specific angle has been chosen to match the proposed CBM detector's rapidity coverage of $1.7 \leq \eta \leq 2.5$ [84]. Both vectors have the same magnitude $|\mathbf{k}_1| = |\mathbf{k}_2|$ ($4 - 7\,\text{GeV}$ in Fig. 6.9). If one considers the HBT functions for two different plasma isotropization times, one notices a plateau structure for $\tau_{\text{iso}} = 2\,\text{fm}/c$, similar to the collinear configuration shown in Fig. 6.5.

The correlation functions in Fig. 6.9 were calculated with a plasma transition parameter $\gamma = 0.5$. At higher values for this parameter, thus a sharper transition, the plateau is reduced. This is in contrast to Fig. 6.6, where sharper transitions lead to a more distinct shape of the correlation function. Considering the correlation functions in Fig. 6.9, we see that the HBT function drops to 1 at relative angles larger than $\approx 25°$. As an outlook for further computations on a discretized grid (see end of Section 6.4.1), this reduces the amount of pair configurations which one has to consider, since photon pair vectors separated by a certain maximal angle do not show any correlation.

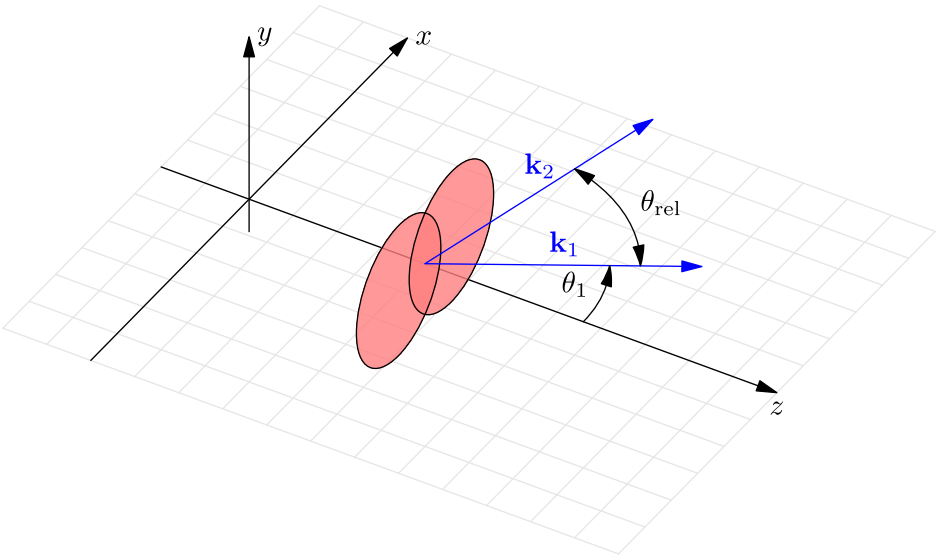

Figure 6.8: Illustration of a non-collinear photon pair configuration in the reaction plane (gray grid). The relative angle θ_{rel} is the only quantity which is varied, while the magnitude of the vectors $\mathbf{k}_1$ and $\mathbf{k}_2$ is held fixed.

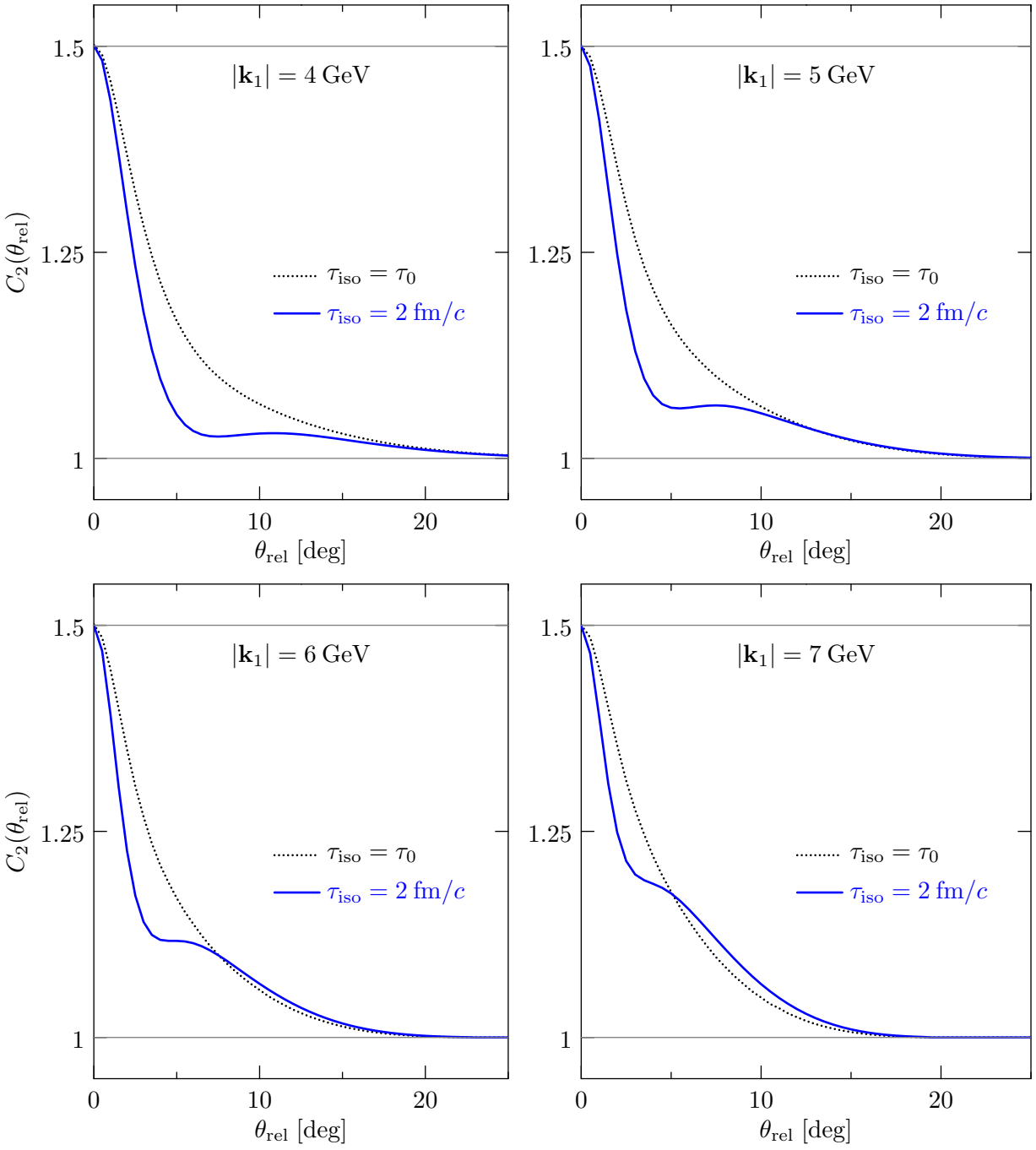

Figure 6.9: HBT correlations as a function of the relative angle of the photon momentum pair $\theta_{\rm rel}$ as seen in Fig. 6.8. A plateau structure similar to Fig. 6.5 arises for large isotropization times. Additionally, the shapes of the HBT functions show a dependence on the magnitude of the photon momentum vectors - the plateau structures move towards smaller relative angles at increasing $|\mathbf{k}_1|$. $\theta_1 = 10°$, $\gamma = 0.5$, $b = 10$ fm.

7

Summary and conclusions

The aim of this thesis is to study the effects of photon double pulses in spectra or intensity correlations. To start, we describe the mechanism to create these double pulses from an anisotropic quark-gluon plasma both in a phenomenological as well as in a quantitative way. It was shown that these time-dependent signals are highly sensitive to the model parameters that characterize the QGP in the calculations. A toy model for a one-dimensional plasma was constructed and used to infer properties of the pulse shapes in an analytic way, such as the location of the second peak of a double pulse structure.

Direct photons are regarded as a promising tool to probe the internal QGP dynamics, as they are produced throughout the total lifetime of the plasma. As of now, there is no established theoretical or practicable method of measuring time-resolved signals on the order of yoctoseconds. The lack of employable methods to measure or characterize photon signals on these short timescales forces us to reformulate the question. We can not directly measure the photon pulses themselves, but there may well be a way of detecting an indirect signal, one that is sensitive to the same mechanisms which give rise to double pulses.

Time-integrated spectra are the first choice for an investigation, as such measurements have already been performed at various experimental facilities. It is expected that experiments at the LHC and at FAIR will record direct photon spectra in the near to foreseeable future. The proposed detector geometry at FAIR is especially relevant, as the calorimeter is placed in forward direction. This range is of special interest, as double pulses only arise at lower emission angles due to the enhanced suppression of the photon rate caused by the anisotropy buildup. We have calculated spectra for various plasma isotropization times and found that ratios of two spectra, measured at two different angles, for example at midrapidity and in forward direction, provide a quantity which is even more sensitive to τ_{iso} than the single-inclusive spectra themselves.

A different approach that we studied are Hanbury Brown-Twiss correlations. By exploiting the quantum statistical properties of a particle emitting source, the complete spatio temporal evolution of the plasma can be encoded in such a correlation function. These two-particle correlations can be functions of momentum space or separation angle of the photon pair. This way, the QGP dynamics at a timescale of yoctoseconds can be made partially accessible. We calculated photon pair configurations with one degree of freedom, such as the aforementioned momentum difference or separation angle.

Outlook

A number of open questions remain regarding both the photon pulses as well as an indirect signal via spectra or photon pair correlations.

Extend HBT calculations. Calculations of the HBT correlation functions were carried out for scenarios, where only one degree of freedom was considered. In order to compare the results with experimental data, the calculation has to be extended to realistic detector geometries, covering more degrees of freedom for the photon pair positions. This is a numerical challenge, as the amount of possible vector pair configurations increases the computation time significantly. Strategies have to be established to deal with the oscillating integrand and speed up the numerical integration while maintaining a sufficient level of precision.

Transverse QGP expansion. In the current calculations, the transverse expansion of the quark-gluon plasma was neglected, as it is small compared to the longitudinal expansion, particularly during the interesting initial stage of the collision. Since most of the interesting effects occur at large impact parameters, the transverse expansion may not be negligible anymore. Incorporating the possibility of a transverse expansion would require a new treatment of calculating the photon production rate in an anisotropic QGP.

Viscosities. Experimental findings suggest to treat the quark-gluon plasma as a strongly coupled, near-perfect fluid. The related effect of elliptic flow is stronger at peripheral collisions, where the double peak structure appears in the photon signals. Reference [48] investigated how the inclusion of viscosities in the hydrodynamical description of the QGP affects the direct photon spectra at an emission angle of $\pi/2$. An improved model of QGP dynamics would modify the calculated shape of the photon pulses and may have an influence on the HBT correlations as well.

Mixed phase contributions. In our calculations, only photons created in the pure QGP phase are considered. After the temperature of the plasma drops below the freezeout temperature, the photon production rate is set to zero at this specific point in space. Introducing a mixed phase, where the photon production rate is a certain fraction of that in the pure QGP phase, would prolong the lifetime of the photon emitting volume and also have an influence on the photon pulse shapes.

Coherence. The calculations start at a formation time τ_0, some finite time after the collision impact. An open question is how the initial collision at $t = 0$ has an effect on potential spatial coherence for the photons created in the QGP. What contributions can we expect from bremsstrahlung photons that arise during the collective deceleration after the initial impact?

Dileptons. Dileptons in the QGP context are lepton pairs that are created from real or virtual photons. As such, they should show similar dependence on the anisotropy and its evolution throughout the QGP lifetime. Thermal dilepton spectra will be investigated at the LHC [107].

A Feynman rules for quantum chromodynamics

These are the Feynman rules for QCD in momentum space [64] used for the calculations in Chapter 3. The rules are derived from the QCD Lagrangian which is given by

$$\mathcal{L}_{\mathrm{QCD}} = \sum_{f=1}^{n_f} \overline{\psi}_f (i \not{D}_\mu - m_f) \psi_f - \frac{1}{4} G^a_{\mu\nu} G^{\mu\nu}_a. \tag{A.1}$$

Quarks with masses m_f are represented by spinors ψ with flavor index f. The covariant derivative $D_\mu = \partial_\mu - igA_\mu$ with Lorentz index μ contains the gauge fields $A_\mu = A^a_\mu T_a$ with the gauge group generators T_a, where a is the index of the adjoint color space. The Yang-Mills term includes the gauge boson field strength $G^a_{\mu\nu} = \partial_\mu A^a_\nu - \partial_\nu A^a_\mu + g f_{abc} A^b_\mu A^c_\nu$ with the quark-gluon coupling g and structure constants f_{abc}.

For the vertices including photons, the rules are derived from the QED Lagrangian:

$$\mathcal{L}_{\mathrm{QED}} = \overline{\psi}(i \not{D}_\mu - m)\psi - \frac{1}{4} F_{\mu\nu} F^{\mu\nu}. \tag{A.2}$$

In the Abelian case of QED, the spinor ψ represents a fermion with mass m. The covariant derivative is given by $D_\mu = \partial_\mu + ieA_\mu$, where the coupling constant is the electric charge e. The field strength tensor reduces to a simpler form compared to QCD, as the gauge fields A_μ do not commute: $F_{\mu\nu} = \partial_\mu A_\nu - \partial_\nu A_\mu$.

Fermionic lines

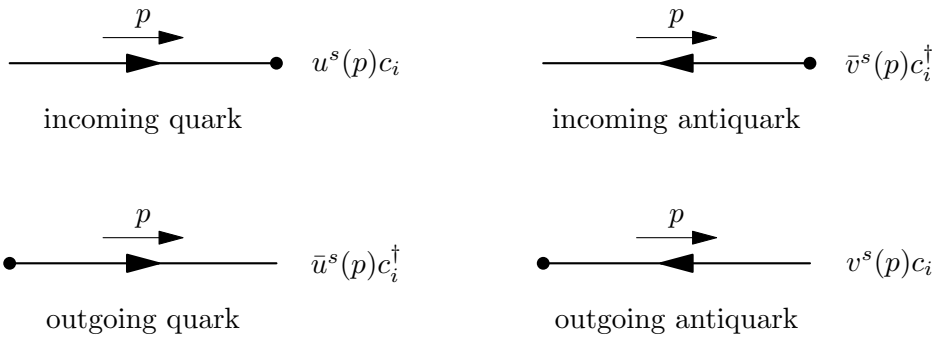

External fermion lines. Quarks with momentum p and spin s are represented by spinors u and their Dirac adjoint $\bar{u}$. Their structure in the fundamental color space is incorporated by color operators c and $c^\dagger$ [108] with color index i. Incoming lines have a color annihilation operator (c), while outgoing quark lines feature color creation operators ($c^\dagger$). For antiquarks, the incoming lines have a Dirac adjoint spinor $\bar{v}$, whereas outgoing lines have spinors v. The color operators are exchanged as well.

Quark and antiquark propagators for (anti)quarks with mass m and momentum p. Notice the sign

difference for the antiquark propagator that occurs due to the momentum arrow pointing in the opposite direction of the fermion line.

Bosonic lines

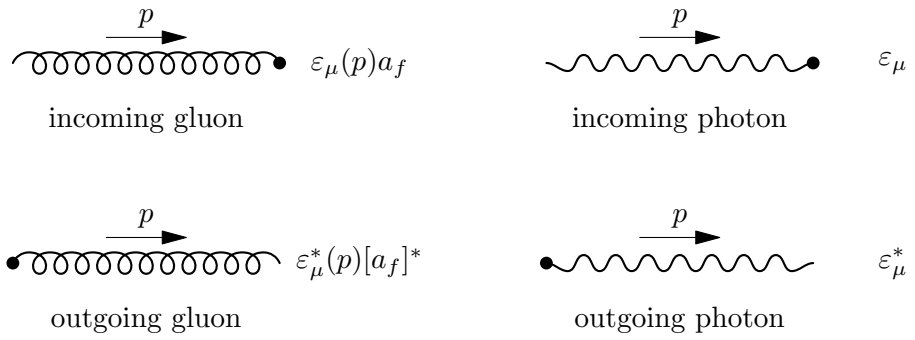

External gauge boson lines. Incoming gluons with momentum p are represented by polarization vectors ε which have a Lorentz index μ. They are objects in the adjoint color space, which is implemented by color operators a that have a adjoint color index f. Outgoing gluons are constructed via the complex conjugate polarization vectors ε^*_μ. Photons are represented by polarization vectors as well, but they do not feature adjoint color indices.

Vertices

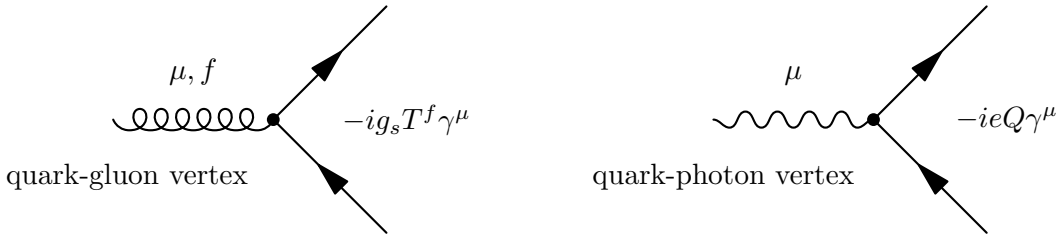

QED and QCD vertices including fermions. The Feynman rules for the quark-gluon vertex contains the gauge group matrices T with adjoint color index f as well as the strong coupling constant g_s. The QED vertex is analogous, where the coupling is replaced by eQ and Q represents the quark charge in units of the elementary electric charge e. Other vertices including ghosts or the remaining gluon vertices were not used in the calculations and are omitted here.

B Conjugate of the Compton scattering matrix element

The matrix element

$$\begin{aligned}(i\mathcal{M}_{qg\to q\gamma})^\dagger = {} & c_i^\dagger u_{\delta'}^{s\dagger}(p_1)\left(+ieQ\,[\gamma^{\mu'}_{\gamma'\delta'}]^\dagger\right)\varepsilon_{\mu'}(p)\frac{-i(\not{q}_2+m)^\dagger_{\beta'\gamma'}}{q_2^2-m^2}a_f^\dagger\varepsilon^*_{\nu'}(p_3)\\ & \times\left(+ig_s[\gamma^{\nu'}_{\alpha'\beta'}]^\dagger[T^f]^\dagger\right)c_j\bar{u}^{s'\dagger}_{\alpha'}\\ & + u_{\delta'}^{s\dagger}\left(+ig_s[T^f]^\dagger[\gamma^{\nu'}_{\gamma'\delta'}]^\dagger\right)a_f^\dagger\varepsilon^*_{\nu'}(p_3)\frac{-i(\not{q}_1+m)^\dagger_{\beta'\gamma'}}{q_1^2-m^2}\varepsilon_{\mu'}(p)\\ & \times\left(+ieQ\,[\gamma^{\mu'}_{\alpha'\beta'}]^\dagger\right)c_j\bar{u}^{s'\dagger}_{\alpha'},\end{aligned} \tag{B.1}$$

can be simplified by using the properties of the Dirac matrices and the adjoint spinors. Since

$$\bar{u}_\beta = u_\alpha^\dagger\gamma^0_{\alpha\beta}, \tag{B.2}$$

the Hermitian conjugate is

$$(\bar{u}_\beta)^\dagger = (\gamma^0_{\alpha\beta})^\dagger u_\beta = \gamma^0_{\alpha\beta}u_\beta. \tag{B.3}$$

Here we have used the hermiticity of γ^0. In (B.1), we encounter terms like

$$(\gamma^{\mu'}_{\alpha'\beta'})^\dagger\bar{u}^\dagger_{\beta'}. \tag{B.4}$$

Since $(\gamma^\mu)^\dagger = \gamma^0\gamma^\mu\gamma^0$, we can write using (B.3):

$$(\gamma^{\mu'}_{\alpha'\beta'})^\dagger\bar{u}^\dagger_{\beta'} = (\gamma^{\mu'}_{\alpha'\beta'})^\dagger\gamma^0_{\beta'\gamma'}u_{\gamma'} = \gamma^0_{\alpha'\delta'}\gamma^{\mu'}_{\delta'\varepsilon'}\gamma^0_{\varepsilon'\beta'}\gamma^0_{\beta'\gamma'}u_{\gamma'} = \gamma^0_{\alpha'\delta'}\gamma^{\mu'}_{\delta'\gamma'}u_{\gamma'}. \tag{B.5}$$

The relation in (B.5) allows us to pull the two γ^0 matrices away from each $(\bar{u})^\dagger$ and through all Dirac matrices, until we can attach them onto the conjugate spinors $u^\dagger$ to form Dirac adjoint spinors $\bar{u}$ again. Using the hermiticity of the gauge group generators T^f, (B.1) can be rewritten as

$$\begin{aligned}(i\mathcal{M}_{qg\to q\gamma})^\dagger = {} & c_i^\dagger\bar{u}_{\delta'}^{s\dagger}(p_1)\left(+ieQ\,\gamma^{\mu'}_{\delta'\gamma'}\right)\varepsilon_{\mu'}(p)\frac{-i(\not{q}_2+m)_{\gamma'\beta'}}{q_2^2-m^2}a_f^\dagger\varepsilon^*_{\nu'}(p_3)\\ & \times\left(+ig_s\gamma^{\nu'}_{\beta'\alpha'}T^f\right)c_j u^{s'\dagger}_{\alpha'}\\ & + \bar{u}_{\delta'}^{s\dagger}\left(+ig_sT^f\gamma^{\nu'}_{\delta'\gamma'}\right)a_f^\dagger\varepsilon^*_{\nu'}(p_3)\frac{-i(\not{q}_1+m)_{\gamma'\beta'}}{q_1^2-m^2}\varepsilon_{\mu'}(p)\\ & \times\left(+ieQ\,\gamma^{\mu'}_{\beta'\alpha'}\right)c_j u^{s'\dagger}_{\alpha'}.\end{aligned} \tag{B.6}$$

The two sums in (3.1) and (B.6) can now be multiplied in order to obtain the squared modulus of the scattering amplitude.

C HBT function in the high-energy physics limit

Starting from Equation (6.5), we focus on the cosine term:

$$\cos[k(r_{1A} - r_{1B} - r_{2A} + r_{2B})]. \tag{C.1}$$

In the high-energy physics scenario, the source is much smaller compared to the separation of the detectors. Therefore the distance $d = |\mathbf{d}|$ is much larger than $R = |\mathbf{R}|$. In this approximation, the vectors $\mathbf{r}_{1A}$ and $\mathbf{r}_{1B}$ are assumed to be parallel, as are vectors $\mathbf{r}_{2A}$ and $\mathbf{r}_{2B}$. The detailed HBT scheme is illustrated in Fig. C.1.

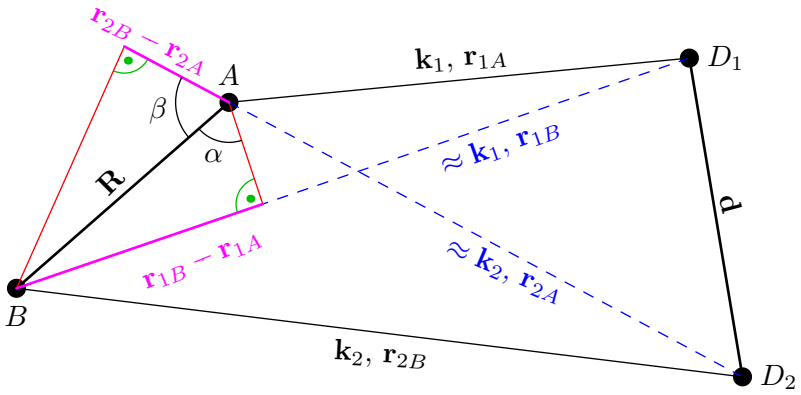

Figure C.1: Detailed HBT scheme (similar to Fig. 6.1). The lengths of the vectors are drawn out of proportion for better legibility of the angles and labels.

We split up the argument of the cosine term in Eq. (C.1) into

$$k(r_{1A} - r_{1B}) - k(r_{2A} - r_{2B}). \tag{C.2}$$

The distances in Eq. (C.2) appear in Fig. C.1 as magenta-colored segments. Considering the corresponding right triangles, we can write

$$R \sin\alpha = r_{1B} - r_{1A}, \tag{C.3a}$$
$$R \cos\beta = r_{2B} - r_{2A}, \tag{C.3b}$$

which can be inserted into Eq. (C.2). With

$$\mathbf{k}_1 \cdot \mathbf{R} = k\, R\, \sin\alpha, \tag{C.4a}$$
$$(-\mathbf{k}_2) \cdot (-\mathbf{R}) = k\, R\, \cos\beta, \tag{C.4b}$$

we can rewrite Eq. (C.1) as

$$\cos(\mathbf{R} \cdot [\mathbf{k}_1 - \mathbf{k}_2]). \tag{C.5}$$

One has to be careful with the signs of the vectors $\mathbf{R}$, $\mathbf{k}_1$ and $\mathbf{k}_2$. $\mathbf{R}$ is defined as $\mathbf{x}_A - \mathbf{x}_B$, so the triangle involving the angle β has to be spanned by $\mathbf{R}$ and $\mathbf{k}_2$ with negative signs.

D The correlation function in the current formalism

This derivation follows Ref. [97] and Ref. [109]. We start by considering the total current in the fireball $\mathbf{J}$ as a sum over all partial currents

$$\mathbf{J}(\mathbf{x}, t) = \sum_{l}^{N} \mathbf{j}_l(\mathbf{x} - \mathbf{x}_l, t - t_l). \tag{D.1}$$

In this picture, the space-time coordinates $(\mathbf{x}_l, t_l)$ specify the l-th collision of two nucleons which each produce an electromagnetic current. Hence the Fourier transform is

$$\mathbf{J}(\mathbf{k}) = \sum_{l}^{N} \mathbf{j}_l(\mathbf{k})\ e^{ik\,\cdot\,x_l}, \tag{D.2}$$

where

$$k = (|\mathbf{k}|, \mathbf{k}). \tag{D.3}$$

Here, k and x_l are four-vectors. To keep the model simple, a few restrictions have to be made. Usually, one would expect an additional coherent current from the collective deceleration of the two nuclei. This contribution is dropped and only incoherent currents are considered, so that

$$\langle \mathbf{j}_l(\mathbf{k}) \rangle = 0. \tag{D.4}$$

Coherent effects on the correlation function can also be neglected, since the photon energies of interest are high enough. The model is now reduced to the most simple case, in which the incoherent currents all have the same magnitude. As Neuhauser already pointed out, this is not a realistic case. The collisions in the center of the fireball will probably differ from the more peripheral collisions in the outer regions. Also, due to the mostly isotropic nature of the nuclear force, one expects two different currents from two separate collisions to have no directional correlation whatsoever:

$$\langle \mathbf{j}_\mathbf{l} \cdot \mathbf{j}_{l'} \rangle = 0 \qquad\qquad \forall\ l \neq l'. \tag{D.5}$$

Using the aforementioned approximations, the current in momentum space is

$$\mathbf{J}(k) = j(k) \sum_{l}^{N} \hat{\mathbf{v}}_l \exp(ik \cdot x_l). \tag{D.6}$$

Because of the two assumptions, the directional dependence is now only manifest in the random unit vector $\hat{\mathbf{v}}_l$. All the necessary assumptions are now made to calculate the one- and two-photon inclusive distribution function

$$P(\mathbf{k}) = \langle |M_{\varepsilon,\mathbf{k}}|^2 \rangle = \langle |\varepsilon \cdot \mathbf{J}(k)|^2 \rangle. \tag{D.7}$$

Since the polarization of the photons is not known, we need to take an average and sum over all polarizations. After inserting the parametrization of the classical current, the one-photon distribution

function reads

$$P(\mathbf{k}) = \sum_{\lambda=1}^{2} \langle |\varepsilon_\lambda \cdot \mathbf{J}(k)|^2 \rangle = \sum_{\lambda=1}^{2} \langle |\varepsilon_\lambda \cdot j(k) \sum_{l=1}^{N} \hat{\mathbf{v}}_l \exp(ik \cdot x_l)|^2 \rangle. \tag{D.8}$$

In the next step, the modulus is expanded ($|z|^2 = z \cdot \bar{z}$):

$$P(\mathbf{k}) = \sum_{\lambda=1}^{2} \left\langle \left(\varepsilon_\lambda \, j(k) \sum_{l=1}^{N} \hat{\mathbf{v}}_l e^{ik \cdot x_l} \right) \left(\varepsilon_\lambda \, j^*(k) \sum_{l'=1}^{N} \hat{\mathbf{v}}_{l'} e^{-ik \cdot x_{l'}} \right) \right\rangle \tag{D.9a}$$

$$= \sum_{\lambda=1}^{2} \left\langle \sum_{l,l'}^{N} (\varepsilon_\lambda \cdot \hat{\mathbf{v}}_l)(\varepsilon_\lambda \cdot \hat{\mathbf{v}}_{l'}) j(k) j^*(k) e^{ik(x_l - x_{l'})} \right\rangle \tag{D.9b}$$

$$= \sum_{\lambda=1}^{2} |j(k)|^2 \sum_{l,l'} \left\langle (\varepsilon_\lambda \cdot \hat{\mathbf{v}}_l)(\varepsilon_\lambda \cdot \hat{\mathbf{v}}_{l'}) e^{ik(x_l - x_{l'})} \right\rangle. \tag{D.9c}$$

The current can be pulled out of the average, since it has no spatial dependence. To evaluate the time-average (which is equal to a spatial average here), one must take a closer look at the product of polarizations and the random unit vectors. Assuming that during the time span, over one averages, the random unit vector points in all directions, we need to average this product over all spatial directions of $\hat{\mathbf{v}}_l$:

$$\langle (\varepsilon \cdot \hat{\mathbf{v}}_l)(\varepsilon' \cdot \hat{\mathbf{v}}_{l'}) \rangle = \frac{1}{4\pi} \int d\Omega \, (\varepsilon \cdot \hat{\mathbf{v}}_l(\vartheta, \varphi)) \, (\varepsilon' \cdot \hat{\mathbf{v}}_l(\vartheta, \varphi)) \, \delta_{ll'} \tag{D.10}$$

To see why only the average with the condition $l = l'$ survives ($\delta_{ll'}$), one needs to visualize the averaging. The two polarization vectors ε and ε' are held fixed in space, whereas the random vectors are integrated over all directions. If $\hat{\mathbf{v}}_l$ and $\hat{\mathbf{v}}_{l'}$ are two different vectors, then the averaging affects each polarization vector individually:

$$\langle (\varepsilon \cdot \hat{\mathbf{v}}_l)(\varepsilon' \cdot \hat{\mathbf{v}}_{l'}) \rangle = \langle \varepsilon \cdot \hat{\mathbf{v}}_l \rangle \langle \varepsilon' \cdot \hat{\mathbf{v}}_{l'} \rangle \tag{D.11}$$

Of course the averaging of such a dot product with only one vector held in place is zero and the term vanishes completely. Thus the condition $\delta_{ll'}$ is imposed. What is left to do is to parametrize the vectors in spherical coordinates (remember $|\hat{\mathbf{v}}_l| = |\hat{\mathbf{v}}_{l'}| = 1$) and integrate over the total solid angle:

$$\langle (\varepsilon \cdot \hat{\mathbf{v}}_l)(\varepsilon' \cdot \hat{\mathbf{v}}_{l'}) \rangle = \frac{1}{4\pi} \int_0^\pi \int_0^{2\pi} d\vartheta d\varphi \, \sin\vartheta \, (\varepsilon_r \sin\vartheta \cos\varphi + \varepsilon_\vartheta \sin\vartheta \sin\varphi + \varepsilon_\varphi \cos\vartheta)$$
$$\times \left(\varepsilon'_r \sin\vartheta \cos\varphi + \varepsilon'_\vartheta \sin\vartheta \sin\varphi + \varepsilon'_\varphi \cos\vartheta \right) \delta_{ll'} \tag{D.12a}$$

$$= \frac{1}{3} (\varepsilon \cdot \varepsilon') \delta_{ll'}. \tag{D.12b}$$

With this result, $P(\mathbf{k})$ reduces to a simple form:

$$P(\mathbf{k}) = \sum_{\lambda=1}^{2} |j(k)|^2 \sum_{l,l'}^{N} \frac{1}{3} (\varepsilon \cdot \varepsilon) \delta_{ll'} \langle e^{ik(x_l - x_{l'})} \rangle = \sum_{\lambda=1}^{2} |j(k)|^2 \sum_{l}^{N} \frac{1}{3} (\varepsilon \cdot \varepsilon'). \tag{D.13}$$

Now the polarization sum can be calculated using $\sum \varepsilon^i \varepsilon^j = \delta^{ij} - n^i n^j$, and in this case $i = j$:

$$P(\mathbf{k}) = \sum_{l=1}^{N} |j(k)|^2 \frac{1}{3} \left(\delta^{ii} - n^i n^i\right) = \frac{2}{3} N |j(k)|^2. \tag{D.14}$$

The calculation of $P(\mathbf{k}_1, \mathbf{k}_2)$ is analogous to the calculation of the one-photon distribution function. This time, two different polarization vectors and the associated two different momenta appear:

$$P(\mathbf{k}_1, \mathbf{k}_2) = \langle |\varepsilon_{k_1} \cdot \mathbf{J}(k_1)|^2 |\varepsilon_{k_2} \cdot \mathbf{J}(k_2)|^2 \rangle \tag{D.15a}$$

$$= \sum_{\varepsilon_{k_1}, \varepsilon_{k_2}} \langle |\varepsilon_{k_1} j(k_1) \sum_{l}^{N} \hat{\mathbf{v}}_l e^{i k_l x_l}|^2 \, |\varepsilon_{k_2} j(k_2) \sum_{m}^{N} \hat{\mathbf{v}}_m e^{i k_m x_m}|^2 \rangle \tag{D.15b}$$

$$= \sum_{\varepsilon_{k_1}, \varepsilon_{k_2}} \langle \left(\sum_{l} \varepsilon_{\mathbf{k_1}} j(k_1) \hat{\mathbf{v}}_l e^{i k_1 x_l} \right) \left(\sum_{l'} \varepsilon_{k_1} j^*(k_1) \hat{\mathbf{v}}_{l'} e^{-i k_1 x_{l'}} \right)$$

$$\times \left(\sum_{m} \varepsilon_{k_2} j(k_2) \hat{\mathbf{v}}_m e^{i k_2 x_m} \right) \left(\sum_{m'} \varepsilon_{k_2} j^*(k_2) \hat{\mathbf{v}}_{m'} e^{-i k_2 x_{m'}} \right) \rangle. \tag{D.15c}$$

The terms can now again be rearranged in the same manner as before. The currents are again pulled out of the average, leaving only products of random unit vectors and polarization vectors.

$$P(\mathbf{k}_1, \mathbf{k}_2) = \sum_{\varepsilon_{k_{1,2}}} \sum_{l,l'}^{N} \sum_{m,m'}^{N} |j(k_1)|^2 |j(k_2)|^2 \langle e^{i k_1 (x_l - x_{l'})} e^{i k_2 (x_m - x_{m'})}$$

$$\times (\varepsilon_{k_1} \cdot \hat{\mathbf{v}}_l)(\varepsilon_{k_1} \cdot \hat{\mathbf{v}}_{l'})(\varepsilon_{k_2} \cdot \hat{\mathbf{v}}_m)(\varepsilon_{k_2} \cdot \hat{\mathbf{v}}_{m'}) \rangle. \tag{D.16}$$

The situation now is slightly different than in the calculation before. There are now several conditions, under which the average of the last 4 terms is nonzero. Since always two unit vectors have to be the same for a non-vanishing average, one needs to investigate the 3 possible cases $\delta_{mm'}\delta_{ll'}$, $\delta_{lm}\delta_{l'm'}$ and $\delta_{lm'}\delta_{l'm}$ and can use the relations derived for $P(\mathbf{k})$.

$$\delta_{ll'}\delta_{mm'}: \quad \langle (\varepsilon_{k_1} \cdot \hat{\mathbf{v}}_l)(\varepsilon_{k_1} \cdot \hat{\mathbf{v}}_l)(\varepsilon_{k_2} \cdot \hat{\mathbf{v}}_m)(\varepsilon_{k_2} \cdot \hat{\mathbf{v}}_m) \rangle = \frac{4}{9}, \tag{D.17a}$$

$$\delta_{lm}\delta_{l'm'}: \quad \langle (\varepsilon_{k_1} \cdot \hat{\mathbf{v}}_l)(\varepsilon_{k_2} \cdot \hat{\mathbf{v}}_l)(\varepsilon_{k_1} \cdot \hat{\mathbf{v}}_{l'})(\varepsilon_{k_2} \cdot \hat{\mathbf{v}}_{l'}) \rangle = \frac{1}{9} (\varepsilon_{k_1} \cdot \varepsilon_{k_2})^2, \tag{D.17b}$$

$$\delta_{lm'}\delta_{l'm}: \quad \ldots = \frac{1}{9} (\varepsilon_{k_1} \cdot \varepsilon_{k_2})^2. \tag{D.17c}$$

The calculation was done in the same way as before, by parametrizing the unit vectors in spherical coordinates and performing the integration over the full solid angle ($\frac{1}{4\pi} \int d\Omega$). Now by carefully putting the terms together and paying attention to how the Kronecker-deltas act on the exponential functions,

one gets

$$P(\mathbf{k}_1,\mathbf{k}_2) = \sum_{\varepsilon_{k_{1,2}}} \sum_{l,l'}^{N} \sum_{m,m'}^{N} |j(k_1)|^2 |j(k_2)|^2 \frac{1}{9} \left(4\delta_{ll'}\delta_{mm'} + (\varepsilon_{k_1}\cdot\varepsilon_{k_2})^2[\delta_{lm}\delta_{l'm'} + \delta_{lm'}\delta_{l'm}]\right)$$
$$\times \left\langle e^{ik_1(x_l - x_{l'})} e^{ik_2(x_m - x_{m'})} \right\rangle \tag{D.18a}$$
$$= \sum_{\varepsilon_{k_{1,2}}} \sum_{l,l'}^{N} \sum_{m,m'}^{N} |j(k_1)|^2 |j(k_2)|^2 \tag{D.18b}$$
$$\times \frac{1}{9} \left(4 + (\varepsilon_{k_1}\cdot\varepsilon_{k_2})^2[\langle e^{ix_m(k_1+k_2)} e^{-ix_{m'}(k_1+k_2)}\rangle + \langle e^{ix_{m'}(k_1-k_2)} e^{ix_m(k_1-k_2)}\rangle]\right).$$

Using the definition of the ensemble average

$$\langle e^{ikx}\rangle = \int e^{ikx}\rho(x)d^4x = \rho(k), \tag{D.19}$$

the final result is

$$P(\mathbf{k}_1,\mathbf{k}_2) = \sum_{\varepsilon_{k_{1,2}}} |j(k_1)|^2 |j(k_2)|^2 \frac{N^2}{9} \left(4 + (\varepsilon_{k_1}\cdot\varepsilon_{k_2})^2[|\rho(q)|^2 + |\rho(p)|^2]\right) \tag{D.20a}$$
$$= \left(\frac{2}{3}N|j(k_1)|^2\right)\left(\frac{2}{3}N|j(k_2)|^2\right)$$
$$\times \left(1 + \frac{1}{4}(1 + (\hat{\mathbf{k}}_2\cdot\hat{\mathbf{k}}_2)^2)[|\rho(q)|^2 + |\rho(p)|^2]\right) \tag{D.20b}$$
$$= P(\mathbf{k}_1)P(\mathbf{k}_2)\left\{1 + \frac{1}{4}\left(1 + (\hat{\mathbf{k}}_1\cdot\hat{\mathbf{k}}_2)^2\right)[|\rho(q)|^2 + |\rho(p)|^2]\right\}. \tag{D.20c}$$

Here, the abbreviations $q = k_1 - k_2$ and $p = k_1 + k_2$, were used and the summation over polarizations was performed using

$$\sum_{\varepsilon}(\varepsilon\cdot\varepsilon')^2 = 1 + (\hat{\mathbf{k}}\cdot\hat{\mathbf{k}}')^2. \tag{D.21}$$

The single-photon distribution functions cancel in the full two-photon correlation function and the final result is

$$C_2(\mathbf{k}_1,\mathbf{k}_2) = \frac{P(\mathbf{k}_1,\mathbf{k}_2)}{P(\mathbf{k}_1)P(\mathbf{k}_2)} = 1 + \frac{1}{4}\left(1 + (\hat{\mathbf{k}}_1\cdot\hat{\mathbf{k}}_2)^2\right)\left[|\rho(q)|^2 + |\rho(p)|^2\right]. \tag{D.22}$$

The density $\rho(k)$ is the Fourier transformed source density of the photon emission region.

Bibliography

[1] C.-N. Yang and R. L. Mills, "Conservation of Isotopic Spin and Isotopic Gauge Invariance," *Phys.Rev.* **96** (1954) 191–195.

[2] D. Gross and F. Wilczek, "Ultraviolet Behavior of Nonabelian Gauge Theories," *Phys.Rev.Lett.* **30** (1973) 1343–1346.

[3] H. D. Politzer, "Asymptotic freedom: An approach to strong interactions," *Physics Reports* **14** no. 4, (1974) 129 – 180.

[4] D. Gross, "Asymptotic freedom and QCD: A historical perspective," *Nucl.Phys.Proc.Suppl.* **135** (2004) 193–211.

[5] M. Gell-Mann and F. Low, "Quantum electrodynamics at small distances," *Phys.Rev.* **95** (1954) 1300–1312.

[6] C. G. Callan, Jr., "Broken scale invariance in scalar field theory," *Phys.Rev.* **D2** (1970) 1541–1547.

[7] K. Symanzik, "Small distance behaviour in field theory and power counting," *Communications in Mathematical Physics* **18** (1970) 227–246. 10.1007/BF01649434.

[8] E. D. Bloom, D. H. Coward, H. DeStaebler, J. Drees, G. Miller, L. W. Mo, R. E. Taylor, M. Breidenbach, J. I. Friedman, G. C. Hartmann, and H. W. Kendall, "High-energy inelastic $e-p$ scattering at 6° and 10°," *Phys. Rev. Lett.* **23** (Oct, 1969) 930–934.

[9] S. Bethke, "Experimental tests of asymptotic freedom," *Prog.Part.Nucl.Phys.* **58** (2007) 351–386, `arXiv:hep-ex/0606035 [hep-ex]`.

[10] A. Bazavov, T. Bhattacharya, M. Cheng, N. Christ, C. DeTar, *et al.*, "Equation of state and QCD transition at finite temperature," *Phys.Rev.* **D80** (2009) 014504, `arXiv:0903.4379 [hep-lat]`.

[11] S. Borsanyi, G. Endrodi, Z. Fodor, C. Hoelbling, S. Katz, *et al.*, "Transition temperature and the equation of state from lattice QCD, Wuppertal-Budapest results," *J.Phys.Conf.Ser.* **316** (2011) 012020.

[12] S. Hands, "The Phase diagram of QCD," *Contemp.Phys.* **42** (2001) 209–225, `arXiv:physics/0105022 [physics.ed-ph]`.

[13] M. G. Alford, A. Schmitt, K. Rajagopal, and T. Schafer, "Color superconductivity in dense quark matter," *Rev.Mod.Phys.* **80** (2008) 1455–1515, `arXiv:0709.4635 [hep-ph]`.

[14] A. Schmitt, "Dense matter in compact stars: A pedagogical introduction," *Lect.Notes Phys.* **811** (2010) 1–111, `arXiv:1001.3294 [astro-ph.SR]`.

[15] A. Schmitt, S. Stetina, and M. Tachibana, "Ginzburg-Landau phase diagram for dense matter with axial anomaly, strange quark mass, and meson condensation," *Phys.Rev.* **D83** (2011) 045008, `arXiv:1010.4243 [hep-ph]`.

[16] J. Allday, *Quarks, Leptons and the Big Bang.* Taylor & Francis, 2nd ed., 12, 2001.

[17] T. Hashimoto, O. Miyamura, K. Hirose, and T. Kanki, "Mass shift of charmonium near deconfining temperature and possible detection in lepton-pair production," *Phys. Rev. Lett.* **57** (Oct, 1986) 2123–2126.

[18] T. Matsui and H. Satz, "J/ψ Suppression by Quark-Gluon Plasma Formation," *Phys.Lett.* **B178** (1986) 416.

[19] **ALICE** Collaboration, H. Pereira Da Costa, "J/ψ production in pp and Pb-Pb with ALICE at the LHC," `arXiv:1110.1035 [nucl-ex]`.

[20] M. Gyulassy and M. Plumer, "Jet quenching in dense matter," *Phys.Lett.* **B243** (1990) 432–438.

[21] X.-N. Wang, "Discovery of jet quenching and beyond," *Nucl.Phys.* **A750** (2005) 98–120, `arXiv:nucl-th/0405017 [nucl-th]`.

[22] H. Song, S. A. Bass, and U. Heinz, "Elliptic flow in 200 A GeV Au+Au collisions and 2.76 A TeV Pb+Pb collisions: insights from viscous hydrodynamics + hadron cascade hybrid model," *Phys.Rev.* **C83** (2011) 054912, `arXiv:1103.2380 [nucl-th]`.

[23] **NA50 Collaboration** Collaboration, R. Arnaldi *et al.*, "The Onset of the anomalous J/ψ suppression in Pb Pb collisions at the CERN SPS," `arXiv:hep-ex/0106079 [hep-ex]`.

[24] A. Chaudhuri, "J/ψ production in Au+Au collisions at RHIC and the nuclear absorption," `arXiv:nucl-th/0307029 [nucl-th]`.

[25] **STAR** Collaboration, J. Adams *et al.*, "Azimuthal anisotropy at RHIC: The First and fourth harmonics," *Phys.Rev.Lett.* **92** (2004) 062301, `arXiv:nucl-ex/0310029 [nucl-ex]`.

[26] T. Sakaguchi for the PHENIX Collaboration, "Electromagnetic emission from hot medium measured by the PHENIX experiment at RHIC," `arXiv:1110.2440 [nucl-ex]`.

[27] **STAR** Collaboration, B. Abelev *et al.*, "Systematic Measurements of Identified Particle Spectra in pp, d^+ Au and Au+Au Collisions from STAR," *Phys.Rev.* **C79** (2009) 034909, `arXiv:0808.2041 [nucl-ex]`.

[28] A. Ipp, C. H. Keitel, and J. Evers, "Yoctosecond photon pulses from quark-gluon plasmas," *Phys. Rev. Lett.* **103** (2009) 152301, `arXiv:0904.4503 [hep-ph]`.

[29] M. Martinez and M. Strickland, "Dilepton production as a measure of QGP thermalization time," *J.Phys.G* **G35** (2008) 104162, `arXiv:0804.2618 [hep-ph]`.

[30] A. Dumitru, Y. Guo, and M. Strickland, "The Heavy-quark potential in an anisotropic (viscous) plasma," *Phys.Lett.* **B662** (2008) 37–42, `arXiv:0711.4722 [hep-ph]`.

[31] B. Schenke, A. Dumitru, Y. Nara, and M. Strickland, "QGP collective effects and jet transport," *J.Phys.G* **G35** (2008) 104109, `arXiv:0804.4557 [hep-ph]`.

[32] M. Martinez and M. Strickland, "Suppression of forward dilepton production from an anisotropic quark-gluon plasma," *Eur.Phys.J.* **C61** (2009) 905–913, `arXiv:0808.3969 [hep-ph]`.

[33] Y. Mehtar-Tani, "The Transport coefficient g-hat in an anisotropic plasma," `arXiv:0909.2794 [hep-ph]`.

[34] A. Dumitru, "Quarkonium in a non-ideal hot QCD Plasma," *Prog.Theor.Phys.Suppl.* **187** (2011) 87–95, arXiv:1010.5218 [hep-ph].

[35] A. Rebhan, M. Strickland, and M. Attems, "Instabilities of an anisotropically expanding non-Abelian plasma: 1D+3V discretized hard-loop simulations," *Phys.Rev.* **D78** (2008) 045023, arXiv:0802.1714 [hep-ph].

[36] A. Rebhan, "Nonabelian plasma instabilities in Bjorken expansion," *Nucl.Phys.* **A820** (2009) 123C–126C, arXiv:0810.2805 [hep-ph].

[37] A. Rebhan and D. Steineder, "Collective modes and instabilities in anisotropically expanding ultarelativistic plasmas," *Phys.Rev.* **D81** (2010) 085044, arXiv:0912.5383 [hep-ph].

[38] M. Attems, A. Rebhan, and M. Strickland, "Plasma instabilities in heavy ion collisions," *AIP Conf.Proc.* **1343** (2011) 614–614.

[39] A. Ipp, A. Rebhan, and M. Strickland, "Non-Abelian plasma instabilities: SU(3) vs. SU(2)," *Phys.Rev.* **D84** (2011) 056003, arXiv:1012.0298 [hep-ph].

[40] E. S. Weibel, "Spontaneously Growing Transverse Waves in a Plasma Due to an Anisotropic Velocity Distribution," *Phys.Rev.Lett.* **2** (1959) 83–84.

[41] S. Mrówczyński, "Stream instabilities of the quark-gluon plasma," *Physics Letters B* **214** no. 4, (1988) 587–590.

[42] P. B. Arnold, J. Lenaghan, and G. D. Moore, "QCD plasma instabilities and bottom up thermalization," *JHEP* **0308** (2003) 002, arXiv:hep-ph/0307325 [hep-ph]. Erratum added online, Sep/29/2004.

[43] M. Luzum and P. Romatschke, "Conformal Relativistic Viscous Hydrodynamics: Applications to RHIC results at $\sqrt{s_{\rm NN}} = 200$-GeV," *Phys.Rev.* **C78** (2008) 034915, arXiv:0804.4015 [nucl-th].

[44] J. D. Bjorken, "Highly Relativistic Nucleus-Nucleus Collisions: The Central Rapidity Region," *Phys. Rev.* **D27** (1983) 140–151.

[45] **ALICE** Collaboration, R. Tieulent, "Heavy flavour and quarkonium at forward and central rapidity in p-p collisions with ALICE at LHC," *Acta Phys.Polon.* **B42** (2011) 1655–1662, arXiv:1107.4509 [hep-ex].

[46] R. Chatterjee and D. K. Srivastava, "Elliptic flow of thermal photons and formation time of quark gluon plasma at RHIC," *Phys.Rev.* **C79** (2009) 021901, arXiv:0809.0548 [nucl-th]. Dedicated to the memory of Klaus Geiger on the 10th anneversary of his passing away.

[47] **PHENIX** Collaboration, S. Adler *et al.*, "Centrality dependence of direct photon production in $\sqrt{s_{\rm NN}} = 200$-GeV Au + Au collisions," *Phys.Rev.Lett.* **94** (2005) 232301, arXiv:nucl-ex/0503003 [nucl-ex].

[48] A. Chaudhuri and B. Sinha, "Direct photon production from viscous QGP," *Phys.Rev.* **C83** (2011) 034905, arXiv:1101.3823 [nucl-th].

[49] S. Turbide, C. Gale, S. Jeon, and G. D. Moore, "Energy loss of leading hadrons and direct photon production in evolving quark-gluon plasma," *Phys.Rev.* **C72** (2005) 014906, arXiv:hep-ph/0502248 [hep-ph].

[50] S. Turbide, R. Rapp, and C. Gale, "Hadronic production of thermal photons," *Phys.Rev.* **C69** (2004) 014903, arXiv:hep-ph/0308085 [hep-ph].

[51] M. Martinez and M. Strickland, "Pre-equilibrium dilepton production from an anisotropic quark-gluon plasma," *Phys. Rev.* **C78** (2008) 034917, arXiv:0805.4552 [hep-ph].

[52] P. Romatschke and M. Strickland, "Collective Modes of an Anisotropic Quark-Gluon Plasma," *Phys. Rev.* **D68** (2003) 036004, arXiv:hep-ph/0304092.

[53] M. Martinez and M. Strickland, "Measuring QGP thermalization time with dileptons," *Phys. Rev. Lett.* **100** (2008) 102301, arXiv:0709.3576 [hep-ph].

[54] B. Kampfer and O. P. Pavlenko, "Probing early parton kinetics by photons, dileptons and charm," *Nucl. Phys.* **A566** (1994) 351c–354c.

[55] M. Martinez and M. Strickland, "Non-boost-invariant anisotropic dynamics," *Nucl. Phys.* **A856** (2011) 68–87, arXiv:1011.3056 [nucl-th].

[56] R. Baier, A. H. Mueller, D. Schiff, and D. T. Son, "'Bottom-up' thermalization in heavy ion collisions," *Phys. Lett.* **B502** (2001) 51–58, arXiv:hep-ph/0009237.

[57] J. I. Kapusta, P. Lichard, and D. Seibert, "High-energy photons from quark - gluon plasma versus hot hadronic gas," *Phys.Rev.* **D44** (1991) 2774–2788.

[58] E. Braaten and R. D. Pisarski, "Soft Amplitudes in Hot Gauge Theories: A General Analysis," *Nucl. Phys.* **B337** (1990) 569.

[59] Z.-T. Liang and X.-N. Wang, "Globally polarized quark gluon plasma in non-central A + A collisions," *Phys. Rev. Lett.* **94** (2005) 102301, arXiv:nucl-th/0410079. [Erratum-ibid.Lett.96:039901,2006].

[60] A. Ipp, A. Di Piazza, J. Evers, and C. H. Keitel, "Photon polarization as a probe for quark-gluon plasma dynamics," *Phys. Lett.* **B666** (2008) 315–319, arXiv:0710.5700 [hep-ph].

[61] B. Schenke and M. Strickland, "Photon production from an anisotropic quark-gluon plasma," *Phys. Rev.* **D76** (2007) 025023, arXiv:hep-ph/0611332.

[62] A. Ipp, "Polarized photons from anisotropic quark-gluon plasma." Unpublished.

[63] D. Boyanovsky and H. J. de Vega, "Photon production from a thermalized quark gluon plasma: Quantum kinetics and nonperturbative aspects," *Nucl. Phys.* **A747** (2005) 564–608, arXiv:hep-ph/0311156.

[64] M. E. Peskin and D. V. Schroeder, *An Introduction To Quantum Field Theory*. Westview Press, 10, 1995.

[65] A. Zee, *Quantum Field Theory in a Nutshell*. Princeton University Press, 2 ed., 2, 2010.

[66] A. L. Bondarev, "A new method for calculation of traces of dirac γ-matrices in minkowski space," *Nucl.Phys. B* **733** (2006) 48–58, hep-ph/0504223.

[67] R. Mertig and F. Orellana, "FeynCalc Mathematica package." http://www.feyncalc.org.

[68] J. I. Kapusta and C. Gale, *Finite-Temperature Field Theory: Principles and Applications (Cambridge Monographs on Mathematical Physics)*. Cambridge University Press, 2 ed., 8, 2006.

[69] M. E. Carrington, H. Defu, and M. H. Thoma, "Equilibrium and non-equilibrium hard thermal loop resummation in the real time formalism," *Eur. Phys. J.* **C7** (1999) 347–354, arXiv:hep-ph/9708363.

[70] L. V. Keldysh, "Diagram technique for nonequilibrium processes," *Zh. Eksp. Teor. Fiz.* **47** (1964) 1515–1527. [Sov.Phys.JETP 20:1018,1965].

[71] J. Rammer, *Quantum Field Theory of Non-equilibrium States*. Cambridge University Press, reissue ed., 3, 2011.

[72] S. Mrowczynski and M. H. Thoma, "Hard loop approach to anisotropic systems," *Phys. Rev.* **D62** (2000) 036011, arXiv:hep-ph/0001164.

[73] R. Baier, M. Dirks, K. Redlich, and D. Schiff, "Thermal photon production rate from non-equilibrium quantum field theory," *Phys. Rev.* **D56** (1997) 2548–2554, arXiv:hep-ph/9704262.

[74] N. P. Landsman and C. G. van Weert, "Real and Imaginary Time Field Theory at Finite Temperature and Density," *Phys. Rept.* **145** (1987) 141.

[75] K.-c. Chou, Z.-b. Su, B.-l. Hao, and L. Yu, "Equilibrium and Nonequilibrium Formalisms Made Unified," *Phys. Rept.* **118** (1985) 1.

[76] B. Schenke and M. Strickland, "Fermionic collective modes of an anisotropic quark-gluon plasma," *Phys. Rev.* **D74** (2006) 065004, arXiv:hep-ph/0606160.

[77] A. Ipp, "One-dimensional model of time-dependent photon emission." Unpublished.

[78] R. J. Fries, B. Muller, and D. K. Srivastava, "High-energy photons from passage of jets through quark gluon plasma," *Phys.Rev.Lett.* **90** (2003) 132301, arXiv:nucl-th/0208001 [nucl-th].

[79] R. J. Glauber, *Lectures in Theoretical Physics*. New York: Interscience, 1959.

[80] A. Ipp, J. Evers, C. H. Keitel, and K. Z. Hatsagortsyan, "Streaking at high energies with electrons and positrons," *Phys.Lett.* **B702** (2011) 383–387, arXiv:1008.0355 [physics.ins-det].

[81] **WA98 Collaboration** Collaboration, M. Aggarwal *et al.*, "Direct photon production in 158-A-GeV Pb-208 + Pb-208 collisions," *Phys.Rev.C* (2000) , arXiv:nucl-ex/0006007 [nucl-ex].

[82] **ALICE** Collaboration, D. Zhou, "PHOS, the ALICE-PHOton Spectrometer," *J.Phys.G* **G34** (2007) S719–S723.

[83] **ALICE/PHOS** Collaboration, H. Torii, "The ALICE PHOS calorimeter," *J.Phys.Conf.Ser.* **160** (2009) 012045.

[84] B. Friman, C. Höhne, J. Knoll, S. Leupold, J. Randrup, R. Rapp, and P. Senger, eds., *The CBM Physics Book: Compressed Baryonic Matter in Laboratory Experiments (Lecture Notes in Physics)*. Springer, 1st edition. ed., 3, 2011.

[85] L. Bhattacharya and P. Roy, "Measuring isotropization time of Quark-Gluon-Plasma from direct photon at RHIC," *Phys.Rev.* **C79** (2009) 054910, arXiv:0812.1478 [hep-ph].

[86] L. Bhattacharya and P. Roy, "Rapidity distribution of photons from an anisotropic Quark-Gluon-Plasma," *Phys.Rev.* **C81** (2010) 054904, arXiv:0907.3607 [hep-ph].

[87] L. Bhattacharya, "Estimation of isotropization time ($\tau_{\rm iso}$) of QGP from direct photons," *Nucl.Phys.* **A855** (2011) 351–354, arXiv:1101.5857 [hep-ph].

[88] S. Gräfe. Private communication.

[89] T. Csörgö and B. Lörstad, "Bose-Einstein correlations for three-dimensionally expanding, cylindrically symmetric, finite systems," *Phys.Rev.* **C54** (1996) 1390–1403, arXiv:hep-ph/9509213 [hep-ph]. Revised version.

[90] U. W. Heinz, "Hanbury Brown-Twiss interferometry in high-energy nuclear and particle physics," arXiv:hep-ph/9806512 [hep-ph].

[91] G. Baym, "The Physics of Hanbury Brown-Twiss intensity interferometry: From stars to nuclear collisions," *Acta Phys.Polon.* **B29** (1998) 1839–1884, arXiv:nucl-th/9804026 [nucl-th].

[92] U. W. Heinz and B. V. Jacak, "Two particle correlations in relativistic heavy ion collisions," *Ann.Rev.Nucl.Part.Sci.* **49** (1999) 529–579, arXiv:nucl-th/9902020 [nucl-th].

[93] S. S. Padula, "HBT interferometry: Historical perspective," *Braz.J.Phys.* **35** (2005) 70–99, arXiv:nucl-th/0412103 [nucl-th].

[94] R. Hanbury Brown and R. Twiss, "A New type of interferometer for use in radio astronomy," *Phil.Mag.* **45** (1954) 663–682.

[95] R. Hanbury Brown and R. Twiss, "A Test of a new type of stellar interferometer on Sirius," *Nature* **178** (1956) 1046–1048.

[96] G. Goldhaber, S. Goldhaber, W.-Y. Lee, and A. Pais, "Influence of Bose-Einstein statistics on the anti-proton proton annihilation process," *Phys.Rev.* **120** (1960) 300–312.

[97] D. Neuhauser, "Photon interferometry for heavy ion collisions," *Physics Letters B* **182** no. 3-4, (1986) 289 – 292.

[98] W.-N. Zhang, Y.-Y. Ren, and C.-Y. Wong, "Analysis of pion elliptic flows and HBT interferometry in a granular quark-gluon plasma droplet model," *Phys.Rev.* **C74** (2006) 024908, arXiv:hep-ph/0606113 [hep-ph].

[99] M. Plumer, L. Razumov, and R. Weiner, "Bounds for Bose-Einstein correlation functions," *Phys.Rev.* **D49** (1994) 4434–4437, arXiv:hep-ph/9311230 [hep-ph].

[100] D. K. Srivastava and J. I. Kapusta, "History of quark - gluon plasma evolution from photon interferometry," *Phys.Rev.* **C48** (1993) 1335–1345.

[101] A. Timmermann, M. Plumer, L. Razumov, and R. Weiner, "Photon interferometry of quark - gluon dynamics revisited," *Phys.Rev.* **C50** (1994) 3060–3063, arXiv:hep-ph/9405232 [hep-ph].

[102] D. Peressounko, "Hanbury Brown-Twiss interferometry of direct photons in heavy ion collisions," *Phys.Rev.* **C67** (2003) 014905.

[103] **WA98** Collaboration, M. Aggarwal *et al.*, "Interferometry of direct photons in central Pb-208+Pb-208 collisions at 158-A-GeV," *Phys.Rev.Lett.* **93** (2004) 022301, arXiv:nucl-ex/0310022 [nucl-ex].

[104] D. Peressounko, "Direct photon interferometry," *AIP Conf.Proc.* **828** (2006) 581–586, arXiv:hep-ph/0512110 [hep-ph].

[105] D. Das, G. Lin, S. Chattopadhyay, A. Chikanian, E. Finch, *et al.*, "Preliminary results on direct photon-photon HBT measurements in $\sqrt{s_{\rm NN}} = 62.4$-GeV and 200-GeV Au + Au collisions at RHIC," *Nukleonika* **51** (2006) 55–58, arXiv:nucl-ex/0511055 [nucl-ex].

[106] Y. Kharlov and D. Peressounko. Private communication.

[107] H. van Hees and R. Rapp, "Thermal Dileptons at LHC," arXiv:0706.4443 [hep-ph].

[108] C. Y. Lum and C. H. Oh, "Quantum chromodynamics." Unpublished.

[109] P. Somkuti, "Projektarbeit Theoretische Elementarteilchenphysik." Unpublished.